Investigation of capacitive discharge heating of metallic glasses

Thesis by

Georg Kaltenboeck

In Partial Fulfillment of the Requirements

for the Degree of

Doctor of Philosophy

California Institute of Technology

Pasadena, California

2016

(Defended December 11, 2015)

To Milla, Bernhard, Yvonne, Anna, Ryan, and Savanna.

Acknowledgments

I would like the thank Professor Bill Johnson for giving me the opportunity to work in his research group. Without his support, this work would not have been possible. His discussions always provided me with a invaluable insights, which I would never have been able to uncover on my own. His unwavering support for those working in his group made being there a delight.

I am also grateful to Dr. Marios Demetriou for helping throughout my graduate and undergraduate years. He continually motivated me during my time in grad school, and helped me focus my efforts on fruitful areas of research.

I would like to to thank all of the members of the research group. Glenn Garrett, Joseph Schramm, and Scott Roberts taught me a great deal in lab and provided me with very entertaining conversations. Mike Floyd, Andrew Hoff, Henry Kozachkov, and Joanna Kolodziejska sparked many fruitful discussions during my time at Caltech. I would also like to to thank Professor Konrad Samwer, Professor Sven Bossuyt, and Professor Brent Fultz for their valuable insights and discussions. I am also indebted to Mike Vondrus and John van Deusen for teaching me how to use the tools needed to make all of the pieces of equipment used in this research.

I would also like to thank Glassimetal Technologies for letting me borrow their IR camera, as well as providing me with several samples to test. This research was funded in part by II-VI Foundation, AFOSR, and Glassimetal Technologies. I would also like to thank all of the members of my committee for their time and consideration.

Abstract

In recent years, the discovery of bulk metallic glasses with exceptional properties has generated much interest. One of their most intriguing features is their capacity for viscous flow above the glass transition temperature. This characteristic allows metallic glasses to be formed like plastics at modest temperatures. However, crystallization of supercooled metallic liquids in the best bulk metallic glass-formers is much more rapid than in most polymers and silicate glass-forming liquids. The short times to crystallization impairs experimentation on and processing of supercooled glass-forming metallic liquids. A technique to rapidly and uniformly heat metallic glasses at rates of 10^5 to 10^6 kelvin per second is presented. A capacitive discharge is used to ohmically heat metallic glasses to temperatures in the super cooled liquid region in millisecond time-scales. By heating samples rapidly, the most time-consuming step in experiments on supercooled metallic liquids is reduced orders of magnitude in length. This allows for experimentation on and processing of metallic liquids in temperature ranges that were previously inaccessible because of crystallization.

A variety of forming techniques, including injection molding and forging, were coupled with capacitive discharge heating to produce near net-shaped metallic glass parts. In addition, a new forming technique, which combines a magnetic field with the heating current to produce a forming force, was developed. Viscosities were measured in previously inaccessible temperature ranges using parallel plate rheometry combined with capacitive discharge heating. Lastly, a rapid pulse calorimeter was developed with this technique to investigate the thermophysical behavior of metallic glasses at these rapid heating rates.

Published Content and Contributions

W L Johnson, Georg Kaltenboeck, Marios Demetriou, Joseph P Schramm, X Liu, Konrad Samwer, C P Kim, and Douglas C Hofmann. Beating Crystallization in Glass-Forming Metals by Millisecond Heating and Processing. *Science*, 332(6031):828–833, May 2011, doi: 10.1126/science.1201362
G.K. participated in the conception of the project, collected calorimetric and rheological data, designed and put into practice an injection molding apparatus, prepared data, and participated in writing the manuscript.

Georg Kaltenboeck, Thomas Harris, Kerry Sun, Thomas Tran, Gregory Chang, Joseph P Schramm, Marios Demetriou, and W L Johnson. Accessing thermoplastic processing windows in metallic glasses using rapid capacitive discharge. *Sci Rep*, 4, October 2014, doi: 10.1038/srep06441
G.K. participated in the conception of the project, collected TTT data, designed and put into practice a forging apparatus, prepared data, and participated in writing the manuscript.

Georg Kaltenboeck, Marios D. Demetriou, Scott Roberts, and Johnson. Shaping metallic glasses by electromagnetic pulsing. *Nature Communications*, 7:10576, 2016, doi:10.1038/ncomms10576
G.K. participated in the conception of the project, designed and put into practice a magnetic forming method, prepared data, and participated in writing the manuscript.

Contents

List of Figures

Chapter 1

Beating crystallization in glass-forming metals by millisecond heating and processing

1.1 Abstract

The development of metal alloys that form glasses at modest cooling rates has stimulated broad scientific and technological interest. However, intervening crystallization of the liquid in even the most robust bulk metallic glass-formers is orders of magnitude faster than in many common polymers and silicate glass-forming liquids. Crystallization limits experimental studies of the undercooled liquid and hampers efforts to plastically process metallic glasses. We have developed a method to rapidly and uniformly heat a metallic glass at rates of 10^6 kelvin per second to temperatures spanning the undercooled liquid region. Liquid properties are subsequently measured on millisecond time scales at previously inaccessible temperatures under near-adiabatic conditions. Rapid thermoplastic forming of the undercooled liquid into complex net shapes is implemented under rheological conditions typically used in molding of plastics. By operating in the millisecond regime, we are able to beat the intervening crystallization and successfully process even marginal glass-forming alloys with very limited stability against crystallization that are not processable by conventional heating.

1.2 Introduction

A glass is formed when a liquid is undercooled below the melting point, T_M, of the competing crystalline solid(s) and then freezes at a glass transition temperature, T_g, without crystallizing. Undercooled liquids and glasses are metastable phases, implying that given sufficient time, both will transform to more stable crystalline solids. The glass-forming ability of a liquid is a measure of its metastability; that is, its resistance to crystallization in the undercooled temperature region between T_g and T_M. Robust glass-forming silicate, polymer, and molecular melts exhibit superior metastability, with crystallization time scales that range from minutes to hours, or longer, over the entire undercooled liquid region. Metallic glass formation was first reported by Klement et al. [4] in a eutectic Au-Si alloy that was rapidly quenched through the undercooled liquid region at a cooling rate of 10^6 K/s. At the time, this result was considered surprising because crystallization in undercooled metals and atomic liquids was presumed to be so rapid as to preclude glass formation altogether. Metal alloys with enhanced liquid metastability that form glass at substantially lower cooling rates (1 to 10^3 K/s), so-called bulk metallic glasses, were first developed in the early 1980s [5]. Their development [5, 6], and the use of techniques to suppress the nucleation of crystals such as containerless processing [7, 8], fluxing [5], and preparation of high-purity alloys [9] led to improved metastability of metallic glass-forming melts. Nevertheless, the crystallization rates of these glass-forming metallic liquids remain orders of magnitude higher than those of common glass-forming polymers, silicates, or molecular liquids. Consequently, experimental studies in undercooled metallic liquids are broadly limited by the intervening crystallization of the melt [10, 11]. Measurements of thermodynamic functions, viscosity, atomic diffusion, and crystallization kinetics are generally restricted to temperatures just below T_M or just above T_g and are precluded at intermediate undercooling. For instance, viscosity data on metallic glass-forming melts are generally nonexistent for viscosities in the range from 10^1 to 10^6 Pa·s, because time scales for traditional rheometry exceed crystallization time scales. On the technology side, the application of net-shape thermoplastic forming processes such as injection molding [12, 13], blow molding [14], and microreplication [15, 16, 17] to fabricate high-performance, net-shape metal-glass hardware was met with limited success [18].

For polymer plastics, these technologies have been transformative due in large part to using relatively low process viscosities of 1 to 10^4 Pa·s [19]. Implementation of these methods for metallic glasses has been restricted, however, because of high melt viscosities ($> 10^6$ Pa·s) in the accessible temperature range near the glass transition.

To appreciate the difficulty of avoiding crystallization while processing a liquid at intermediate undercooling, consider the time scale required to relax spatial temperature variations within a sample by heat conduction. For a metallic glass of typical thermal diffusivity of $\sim 10^{-2}\text{cm}^2/\text{s}$ and sample dimensions of several millimeters, this time scale is typically 1 to 10 s. Several multiples of this time are required to establish a uniform temperature. Heating methods that supply heat through the sample boundary do not permit uniform heating in shorter times. To heat more rapidly requires that power be dissipated homogeneously and volumetrically throughout the sample so that temperature variations are never created. Ohmic dissipation by a uniform current density is one way to achieve this. In this work, we exploited the large and nearly temperature-independent electrical resistivity of metallic glasses [20, 21] and used an intense millisecond current pulse to achieve uniform ohmic heating from the glass to the undercooled liquid at rates of $\sim 10^6$ K/s. We used high-frame-rate video, thermal imaging, and high-speed infrared pyrometry to conduct millisecond time-scale viscosity and dynamic enthalpy measurements in the undercooled liquid at temperatures where intervening crystallization precludes conventional rheometry and calorimetry, which are limited to much lower heating and cooling rates. We further demonstrated rapid millisecond injection molding of metallic glass rods into net-shape metallic glass parts under liquid viscosity, pressure, and strain rate conditions widely established as optimum in plastic-forming technology.

When a metallic glass is continuously heated, the glass transition at T_g and onset of crystallization at T_x are heating rate dependent, and the rate-dependent temperature interval, $\Delta T = T_x - T_g$, defines an available process window for the undercooled liquid. Larger values of ΔT indicate higher metastability of the liquid with respect to crystallization. Figure 1.1 illustrates the dependence of T_x and T_g on heating rate for the highly processable bulk metallic glass Vitreloy 1 ($\text{Zr}_{41.2}\text{Ti}_{13.8}\text{Cu}_{12.5}\text{Ni}_{10}\text{Be}_{22.3}$). This alloy is a superior metallic glass-former, with a critical casting

thickness of 3 to 4 cm. At a conventional heating rate of 20 K/min, one has $T_g \approx 620$ K, $T_x \approx 705$ K, and $\Delta T \approx 85$ K [22]. Above a critical heating rate of $\sim$ 200 K/s, crystallization is avoided entirely during heating [23]. This heating rate is roughly two orders of magnitude greater than the critical cooling rate of $\sim$2 K/s [24] that is required to avoid crystallization during quenching of the liquid from high temperature to form the glass. Such heating and cooling rate asymmetry is observed for other systems [such as $Pd_{43}Ni_{10}Cu_{27}P_{20}$ [25]] and is believed to be a general feature of the crystallization kinetics of a metallic glass. For comparison, a marginal glass-forming alloy (a metallic glass with critical casting thickness limited to few millimeters) will exhibit a crystallization curve as in Fig. 1.1 that is shifted to the left by about two orders of magnitude and thereby have a critical heating rate of $\sim 10^4$ K/s. As illustrated in Fig. 1.1, our novel approach permits heating at rates of $\sim 10^6$ K/s to a preselected liquid temperature and thereby enables access to temperatures shown in the upper left quadrant of Fig. 1.1 on time scales many orders of magnitude shorter than previously possible.

The use of electrical current or current pulses and associated Joule heating to locally cut and shear metallic-glass ribbons was reported 20 years ago by Ballard et al. [26]. In what could be viewed as a precursor to the present work, Gibbs et al. [27] and Zaluska, Kulik, and Matyja [28, 29] used ohmic heating to carry out rapid transient annealing of ferromagnetic metallic-glass ribbons. Yavari and co-workers [30, 31] used a current-carrying tungsten electrode tip to locally heat and engrave surfaces, and performed joining-welding of rods by passing a large current density through the junction between the rods. In contrast, we focused on uniform volumetric heating of bulk samples to temperatures spanning the entire undercooled liquid region and on subsequent rapid characterization and processing of the undercooled melt.

The electrical resistivity ρ_e of metallic glasses and corresponding liquids is relatively large ($\sim$ 100 to 250 $\mu\Omega \cdot$ cm), exhibits a small and frequently negative temperature coefficient [$|S| = |(1/\rho_e)d\rho_e/dT| \leq 1 \times 10^4\,\mathrm{K}^{-1}$] [20, 21], and varies smoothly and continuously as the glass transition at T_g is traversed. Crystalline metals and alloys have much smaller resistivity (typically 1 to 50 $\mu\Omega \cdot$ cm)), a larger and positive temperature coefficient ($S \sim 10^2$ to $10^4\,\mathrm{K}^{-1}$), and large discontinu-

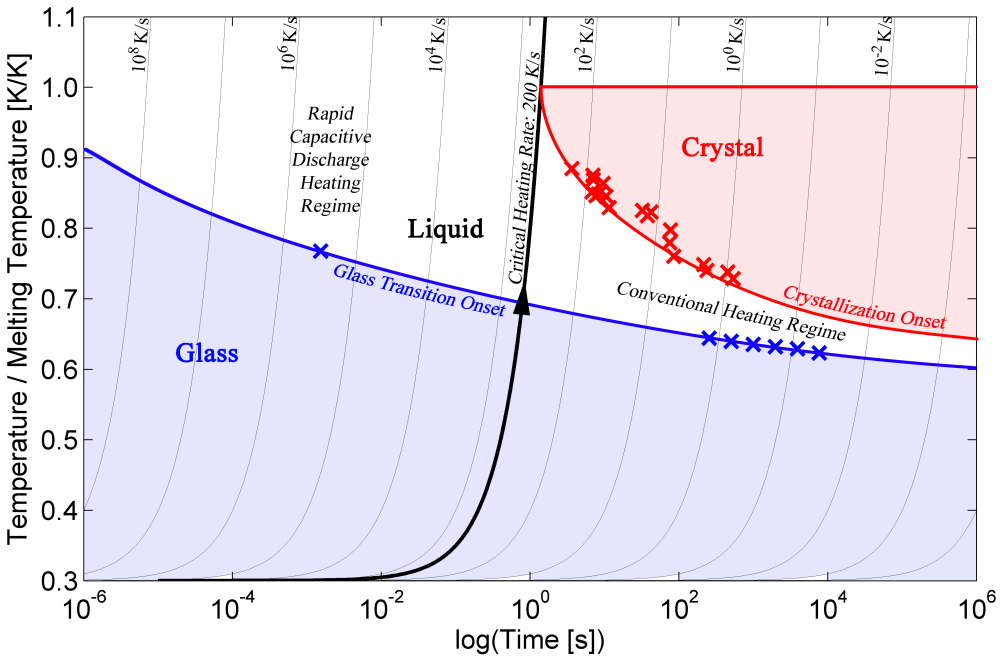

Figure 1.1: Glass-transition onset temperature and crystallization onset temperature versus time for the metallic glass Vitreloy 1 at varying heating rates. Glass transition data are taken from Wang et al. [22] and crystallization data from Schroers et al. [23]. The critical heating rate to completely bypass crystallization on heating from the glass through the liquid is about 200 K/s [23]. Conventional heating rates on the order of 1 K/s provide access to the undercooled liquid over a rather narrow temperature range, above which crystallization becomes kinetically favorable. Using the present approach, which enables heating rates on the order of 10^6 K/s, the undercooled liquid is accessible at any temperature above the glass transition, through the melting point and beyond, where the liquid enters the equilibrium state (upper left quadrant in the diagram). The glass transition data point plotted in this regime was obtained in the present study under a heating rate of $\sim 3 \times 10^5$ K/s (Fig. 1.3B). Reproduced with permission from [1].

ous jump in resistivity on melting. Under high imposed current densities and ohmic dissipation, the heating of crystalline metals tends to spatially localize. Local resistivity and temperature variations (at contacts, interfaces, or inhomogeneities) along the direction of current flow are amplified by increased dissipation in hotter regions. This results in a runaway melting instability as observed, for example, in capacitive discharge welding of metals, in which melting spatially localizes at interfaces, contacts, and areas of high initial resistance. Heating localization in metallic glasses is mitigated by their small $|S|$ and by the absence of a melting discontinuity. A discussion of the requirements for rapid uniform ohmic heating and their application to metallic glasses is provided in Appendix A.4.

1.3 Methods and Results

In the present work, a capacitor bank with capacitance $C = 0.264$ F and charging voltage up to $V_0 = 200$ V was used to store energies up to $E = CV_0^2/2 = 5280$ J. The discharge circuit used was a series RLC circuit tuned to near the critical damping condition that permits a maximum rate of energy dissipation with no circuit ringing or overshoot. For the critically damped circuit, the characteristic time constant for the discharge and dissipation of electrical energy is $\tau_h \approx 0.4$ ms. See Appendix A.3 for details of the RLC circuit and its time response.

Vitreloy 1 rods 4 mm in diameter and 2 cm in length were uniformly heated by capacitive discharge coupled through copper electrodes. The rod was heated from ambient temperature to processing temperatures between T_g and T_M in about 1 ms. After heating, the rod was deformed under a compressive force of ~ 400 N applied via the electrodes. Figure 1.2 shows infrared images (20,480 pixels) of the central portion of a rod at 0.75 ms intervals during heating to a final average temperature of 799 K. This final temperature, T_F, is ~ 180 K above the reported T_g measured by conventional calorimetry (Fig. 1.1) at a heating rate of 20 K/min. The sample geometry used is shown in Fig. 1.3A. The center column of Fig. 1.2 shows the temperature profile measured by the row of pixels located along the rods vertical centerline. The distribution of temperatures measured by all pixels is shown in the right column of Fig. 1.2. The half width at half maximum of final temperature distribution (right column of Fig. 1.2) was $\sim$3.5 K. The low-temperature tail observed in the overall

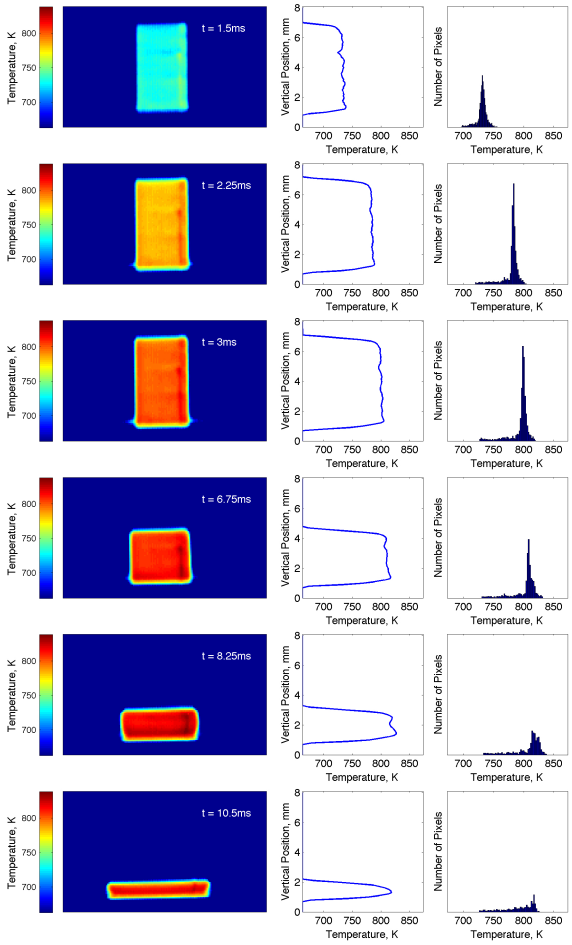

Figure 1.2: Thermal imaging during capacitive discharge heating. (Left column) Selected frames taken from an infrared imaging camera movie; (middle column) temperature measured by pixels along the vertical centerline of the rod; (right column) histogram of temperature measured by all pixels in the image. The half width at half maximum of final temperature distribution (right column) is ∼3.5 K. The low-temperature tail observed in the overall distribution is caused by edge effects that are visible in the thermal images. Reproduced with permission from [1].

distribution is caused by edge effects visible in the thermal images. Although thermal imaging measures surface temperature, an analysis of dynamic electric field penetration effects by Lohfer and Pottlacher [32] (see the Appendix A.4 for more details) shows that temperature inhomogeneity along the radial direction in the rod interior should be less than 1% of the total heating interval, or less than 5 K, with the rod centerline expected to be slightly cooler than the surface. The overall temperature distribution of the heated metallic glass rod is remarkably uniform.

After heating, deformation under the applied load began at an elapsed time of about 3 ms and

continued to about 8 ms (Figs. 2 and 3B). The average temperature rose by about 10 to 15 K during compressive deformation of the rod. This delayed rise is attributed to dissipation of the mechanical work performed by the piston during deformation. Beyond 10 ms, the deformed sample began to cool by radiative and conductive heat loss to the surroundings. Cooling, however, becomes significant only on time scales of several tenths of a second — considerably longer than the time scales for which the present data are analyzed.

To observe detailed transient features of the heating history, an ultrafast infrared pyrometer with time resolution of 5 μs (Appendix A.1) was used to track temperature with much higher time resolution. The high-resolution heating curve of a separate Vitreloy 1 sample is shown in red in the inset of Fig. 1.3B. The dimensions and heating parameters of this sample were identical to the one discussed above, but it was heated in the absence of an applied force so that no viscous deformation occurs. A dynamic glass transition at $\sim$775 K was observed, as revealed by a large horizontal step in the time-temperature trace. The step corresponds to an endothermic heat absorption. At the applied heating rate of $\sim 3 \times 10^5$ K/s, the T_g was shifted by $\sim$155 K above that observed by conventional calorimetry (620 K at a much lower heating rate of 0.67 K/s; Fig. 1.1). After the glass transition, temperature stabilized at a steady plateau value for several milliseconds, indicating that the final heated liquid lost negligible heat to the surroundings for the duration of the plateau. Measurements performed in this plateau regime will therefore be essentially adiabatic. We fitted the high-resolution heating curve below T_g to the analytic solution for dissipation of power by the RLC circuit, given by $T(t) - T_0 \sim \int_0^t t^2 \exp(-t/\tau_h) dt$, to estimate the heating time constant $\tau_h \approx$ 0.33 ms (Appendix A.3). The discrepancy between the final steady-state temperature predicted by the fit and that measured by the pyrometer is attributed to the enthalpy absorption associated with the dynamic transition from an overheated glass to the equilibrium liquid, commonly referred to as enthalpy recovery. The rapid pyrometry with microsecond time resolution, together with the known transient power dissipation, permits enthalpy versus temperature measurements at very high heating rates. The system is effectively a scanning calorimeter operating at scanning rates of 10^5 to 10^6 K/s. As discussed earlier, this is enabled by the uniform ohmic dissipation of heat, whereby

temperature gradients are never created. In conventional calorimetry, heat is supplied from the sample boundaries, and scanning rates are limited by thermal relaxation times on the order of 1 to 10 s.

Figure 1.3C summarizes relevant data on the total specific energy dissipated in the rod, h, and average final sample temperature T_F, for numerous experiments. The specific enthalpy per mole, $h = (\epsilon M/2m)CV^2$ (m is sample mass, and M is the average atomic weight), dissipated in the rod is the total energy stored in the capacitor corrected by an efficiency factor, $\epsilon = R_s/(R_s+R_0)$, where R_s is the sample resistance, and R_0 is the resistance of the circuit with no sample (Appendix A.3). The $h(T_F)$ data collected from a number of experiments are plotted in Fig. 1.3C to obtain a complete $h(T)$ relation for liquid Vitreloy 1 over the undercooled liquid region between 700 and 900 K, previously inaccessible. This $h(T)$ relation is for a configurationally relaxed liquid (as opposed to an overheated glass). Using conventional calorimetry, Busch et al. [33] reported the experimental heat capacity (c_P) of Vitreloy 1 for both the glassy and liquid states up to about 700 K and for the high-temperature liquid near T_M down to about 900 K. For the liquid, they fitted their data to interpolate $c_P(T)$ over the undercooled liquid region using a standard functional form $c_P = 3R+7.50\times10^{-3}T+8.17\times10^{6}T^2$ (J/mol K), where the first two terms in this equation describe the glass below T_g (R is the gas constant). Integrating this expression gives a predicted specific enthalpy $h(T)$ curve that is compared with the present $h(T)$ data plotted in Fig. 1.3C. The comparison shows excellent agreement.

During dynamic deformation, the time-dependent height of the deforming rod, $y(t)$, was measured using frame-by-frame video images. The digitized data were fitted to an analytic functional form that can be differentiated to determine the velocity, dy/dt, and acceleration, d^2y/dt^2, of the pneumatic drive assembly during deformation. These data were used to compute strain rate versus time, and with knowledge of the applied force, the viscosity η at T_F. Because the sample temperature increases slightly during deformation (Fig. 1.3B), the viscosity is measured over a slightly increasing temperature interval. As explained in Appendix A.6, the limited force available (400 N) and response time of the drive system (inertial effects) make the present setup most suitable for measuring viscosities in the range from 10^4 to 10^7 Pa·s. Radiative heat loss from the rod surface

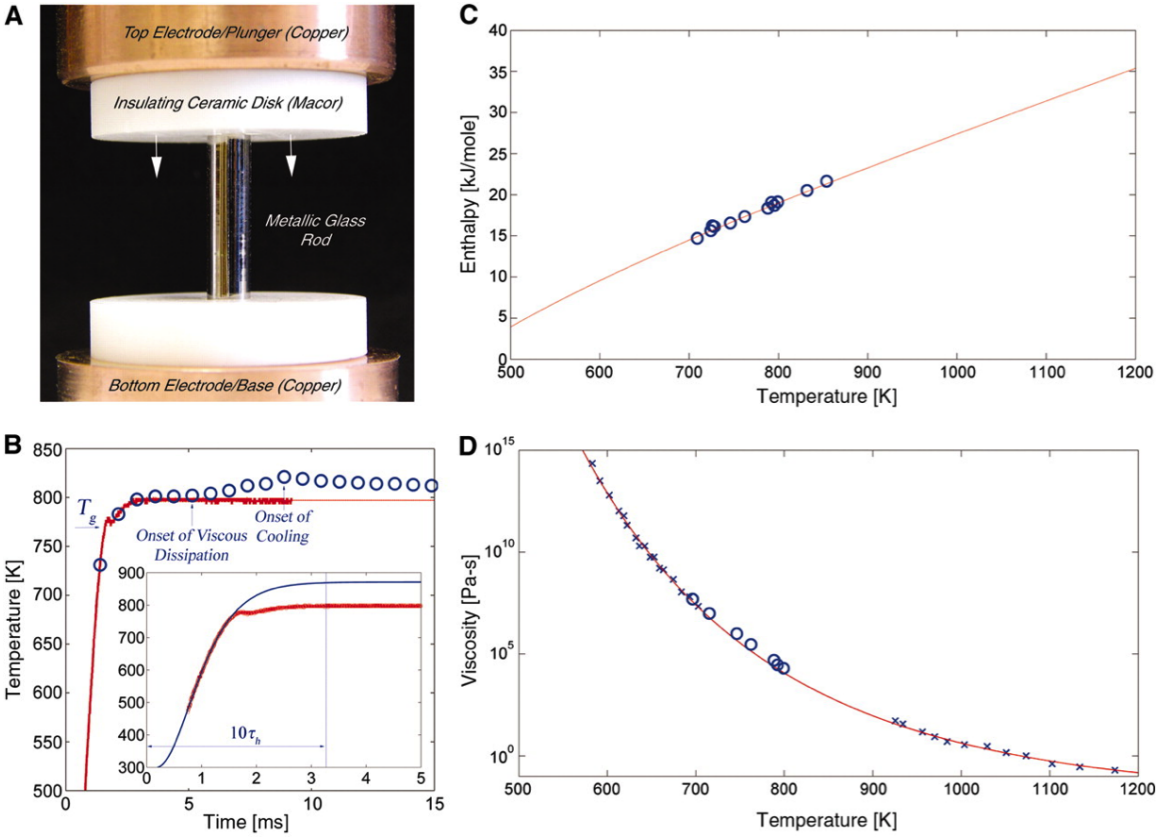

Figure 1.3: Thermodynamic and rheological measurements using capacitive discharge heating. (A) Experimental setup used to measure enthalpy and viscosity. The metallic glass rod is inset into ceramic disks making contact with copper electrodes. (B) (Solid red curve) Thermal trace of an undeformed Vitreloy 1 rod as recorded by a single-pixel high-framerate infrared pyrometer. The onset of T_g at 770 K is indicated. (Blue circles) Temperature response of a deforming Vitreloy 1 rod versus time (same dimensions and conditions as above), averaged over multiple pixels as recorded by an infrared thermal imaging camera. The onset of viscous dissipation caused by deformation and the onset of cooling caused by heat loss to the surroundings are indicated. The inset shows a fit (thin blue line) to the thermal trace (thick red line) of the form $T(t) - T_0 \sim \int_0^t t^2 \exp(-t/\tau_h)dt$, predicted for a critically damped RLC circuit (Appendix A.3). The fitting formula does not account for the enthalpy absorbed at T_g and consequently over-shoots the measured thermal response. (C) Experimental enthalpy $h = (\varepsilon/2)CV^2$ versus temperature T_F (blue circles) and enthalpy computed from liquid heat capacity data of Busch et al. [33] (solid red curve) for Vitreloy 1. (D) Viscosity versus temperature for Vitreloy 1 measured using capacitive discharge heating (blue circles) compared with viscosity data reported in the literature (blue crosses) using beam bending, parallel plate rheometry, and Couette viscometry [34]. Reproduced with permission from [1].

to the surroundings, and heat loss by conduction to the ceramic plates and cold electrodes (located several millimeters behind the ceramic surface), can be neglected in the deforming region on the time scale of the experiment (typically 5 to 15 ms). In other words, the viscosity measurements are carried out under essentially adiabatic conditions. Using the relation $\eta = Fy^2/[3v_0(dy/dt)]$[35], appropriate to the early stage of deformation (Appendix A.6), where F is the applied force and v_0 the sample volume, the viscosity was determined from a number of experiments at various T_F's. In Fig. 1.3D, the results are compared with previously reported viscosity data on Vitreloy 1 obtained with conventional rheology. Conventional beam-bending and parallel plate rheometry [36, 37] require time scales of at least tens of seconds, which limits data to about 80 K above T_g. Couette viscometry [34] at higher temperature (and lower viscosities) similarly requires time scales of at least tens of seconds and is precluded by the intervention of crystallization at temperatures below ∼900 K.

The ability to dynamically process metallic glasses at any undercooled liquid temperature on millisecond time scales creates the opportunity to carry out rapid thermoplastic forming at far lower process viscosities and pressures than was previously possible. Commercial injection molding of plastics is carried out at typical temperatures of 450 to 700 K, process viscosities of 1 to 10^4 Pa·s, and injection pressures of 1 to 30 MPa [19]. To demonstrate injection molding of bulk metallic glasses using typical plastic molding conditions, we designed and constructed a simple injection-molding apparatus. The basic elements of the setup are shown in Fig. 1.4A. Several variants of this apparatus were used to injection-mold net-shape components from Vitreloy 1 and $Pd_{43}Ni_{10}Cu_{27}P_{20}$. Figure 1.4B shows a net-shape metallic glass component with semicircular toroidal geometry molded from a glassy rod of $Pd_{43}Ni_{10}Cu_{27}P_{20}$. Figure 1.4C shows the upper mold tool used to produce the component. The part was produced by rapid heating at 10^6 K/s to $T_F \approx 720$ K, followed by injection into the mold cavity with an applied pressure of ∼20 MPa. The processing viscosity of the $Pd_{43}Ni_{10}Cu_{27}P_{20}$ melt at 720 K is estimated to be $\sim 10^3$ Pa·s [38]. The total time required to form this component was about 40 ms, as determined by monitoring the displacement of the electrode/plunger using high-speed video. This implies strain rates on the order of 10^3 to $10^4 s^{-1}$

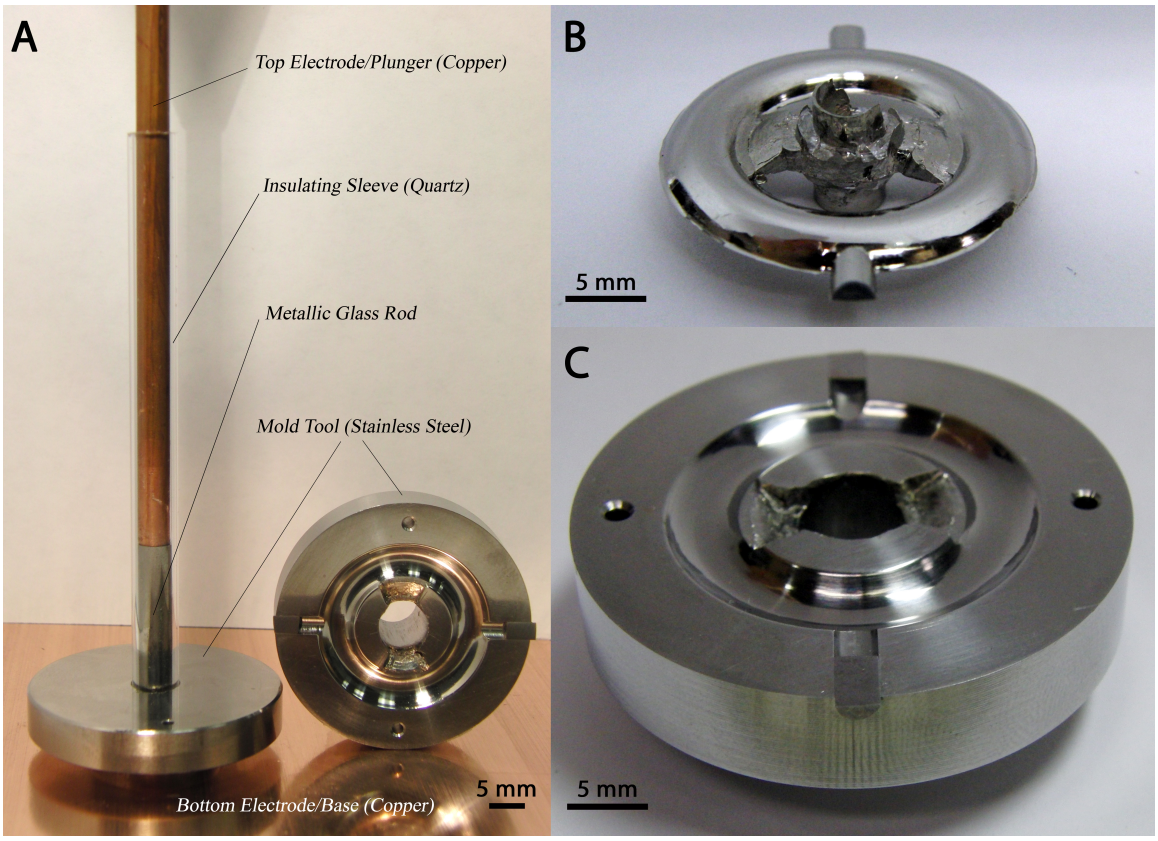

Figure 1.4: Experimental setup based on the capacitive discharge heating approach used to demonstrate injection molding of a metallic glass component. (A) Basic setup comprising an upper copper electrode used as a plunger, a lower copper electrode used as a base (not shown), and a quartz sleeve used as an insulating barrel to electrically insulate and confine the sample charge. A groove is introduced in the quartz sleeve at the point of contact with the mold runner to enable entry of the softened glass into the mold (not shown). (B) A simple "as-molded" $Pd_{43}Ni_{10}Cu_{27}P_{20}$ toroidal metallic glass part formed at a processing temperature of $\sim$ 720 K using a plunger pressure of $\sim$20 MPa. The sample is free of visible flow defects, and no oxidation can be detected despite being processed in open air. (C) Lower half of the mold tool used to mold the metallic glass component. Reproduced with permission from [1].

during the molding process. The rheological conditions (viscosity, pressure, and strain rate) are typical of those used in commercial injection molding of plastic hardware [19]. X-ray diffraction and differential scanning calorimetry show that the product parts are fully glassy for both the Vitreloy 1 and the $Pd_{43}Ni_{10}Cu_{27}P_{20}$ alloy. This is expected because the processing times are much shorter than the time for intervening crystallization (as seen in Fig. 1.1). Moreover, no visible oxidation was detected in either of the parts, despite being processed in open air.

Concerning intervening crystallization, it is of obvious interest to explore the applicability of our rapid heating and forming methods to less robust, or marginal, metallic glass-formers, such as

those with critical casting thicknesses of several millimeters (as opposed to several centimeters). As discussed earlier, marginal glass-formers have crystallization curves shifted to time scales about two orders of magnitude shorter than the robust glass-formers Vitreloy 1 and $Pd_{43}Ni_{10}Cu_{27}P_{20}$ (Fig. 1.1). The marginal metallic glass-forming alloy $Zr_{11}Ti_{33}Cu_{47}Ni_8Si_1$ [39] has a critical casting rod diameter of 5 to 6 mm and exhibits a very restricted processing window $\Delta T \approx 50$ K at conventional heating rates. Thus, its crystallization curve is shifted not only to shorter times but also to lower temperatures closer to T_g (Fig. 1.1). Fully glassy sample rods 3 mm in diameter and 2 cm long were prepared and heated by rapid discharge at $\sim 10^6$ K/s to temperatures midway between T_g and T_M. The rods were deformed under a compressive load of ~400 N between copper electrode plates (as in Fig. 1.3A) but without ceramic spacers. The rods were heated and deformed to flat uniform disks of final thicknesses ranging from 0.5 to 1 mm in total elapsed times of less than 30 ms. The deforming samples were effectively quenched between the copper electrode plates. X-ray diffraction and differential scanning calorimetry verified that the deformed disks were fully glassy, thereby demonstrating that crystallization was avoided in this marginal glass-former.

1.4 Conclusion

The rapid uniform heating approach introduced here allows access to metastable undercooled liquid states of intermediate mobility at temperatures and time scales far outside those probed by traditional methods. This platform enhances the experimental study of thermophysical properties, flow behavior, relaxation phenomena, and crystallization kinetics of undercooled metallic liquids. For example, it enables scanning calorimetry at heating rates of $\sim 10^6$ K/s. On the technology side, the method circumvents intervening crystallization and enables thermoplastic processing and forming of robust as well as marginal glass-forming alloys over the entire range of viscosity observed in undercooled metallic glass-forming melts.

Chapter 2

Accessing thermoplastic processing windows in metallic glasses using rapid capacitive discharge

2.1 Abstract

The ability of the rapid-capacitive discharge approach to access optimal viscosity ranges in metallic glasses for thermoplastic processing is explored. Using high-speed thermal imaging, the heating uniformity and stability against crystallization of $Zr_{35}Ti_{30}Cu_{7.5}Be_{27.5}$ metallic glass heated deeply into the supercooled region is investigated. The method enables homogeneous volumetric heating of bulk samples throughout the entire supercooled liquid region at high rates ($\sim 10^5$ K/s) sufficient to bypass crystallization throughout. The crystallization onsets at temperatures in the vicinity of the "crystallization nose" are identified and a Time-Temperature-Transformation diagram is constructed, revealing a "critical heating rate" for the metallic glass of $\sim$1000 K/s. Thermoplastic process windows in the optimal viscosity range of $10^0 - 10^4$ Pa·s are identified, being confined between the glass relaxation and the eutectic crystallization transition. Within this process window, near-net forging of a fine precision metallic glass part is demonstrated.

2.2 Introduction

Since their discovery, one of the most intriguing features of metallic glasses has been their ability to be formed "thermoplastically" above the glass transition temperature. This "thermoplastic forming" ability was widely perceived as finally bridging the gap between the manufacturing of metals and that of plastics and oxide glasses. Metallic glasses are kinetically frozen supercooled liquids, and thus can be heated above their glass transition temperature where they can relax and recover the properties of the metastable liquid. Since glass-forming liquids have a well-defined equilibrium viscosity that depends strongly on temperature, it was thought to be possible to "dial in" to a viscosity simply by equilibrating the liquid at a certain temperature. As known from plastics processing, the optimum viscosity range for thermoplastic forming is typically $10^0 - 10^4$ Pa·s [19], which for metallic glasses implies a processing temperature in the supercooled liquid region well above the glass-transition temperature T_g (where the viscosity is on the order of 10^{12} Pa·s) and also substantially above the crystallization temperature T_x (where the metallic glass crystallizes when heated at a rate of ∼1 K/s).

Thermoplastic forming of metallic glass was first proposed by Saotome et al., who reported micro-forming a metallic glass in the supercooled liquid region between T_g and T_x to produce micro-electro-mechanical components [40, 41, 42, 43, 15, 44]. Following Saotome's approach, other authors exploited conventional thermoplastic methods used in the processing of plastics and conventional oxide glasses, such as blow molding [14] and injection molding [13], to process bulk articles. Theoretical approaches have also been conceived aiming to quantify the thermoplastic formability of metallic glasses between T_g and T_x [45, 46, 47]. These theoretical approaches are based on estimates of the flow capacity between T_g and T_x and involve integration of the viscosity function within that range. They essentially assume that flow would initiate at T_g and terminate at T_x, thereby rendering the difference $\Delta T = T_x - T_g$ a key parameter in quantifying formability. These models have inspired scientists to develop new bulk-glass forming alloys that demonstrate higher and higher ΔT in the hope of further improving metallic glass formability to levels comparable to plastics or conventional oxide glasses [12]. But even metallic glasses with very high ΔT values (as high as

165 K) [48] have viscosities at T_x not lower than 10^6 Pa·s, i.e., still considerably higher than the optimum "thermoplastic" range. Unlike covalently and polymerically bonded glasses (e.g., silicates and plastics), metallic glasses are inherently unstable against crystallization; their centrosymmetric metallic bonding causes them to crystallize rather rapidly when the viscosity drops below 10^6 Pa·s. These limitations are well quantified by the "thermoplastic formability" models [45, 46, 47].

To work around these limitations and enable access to the optimum thermoplastic viscosity range $10^0 - 10^4$ Pa·s, the metallic glass must be heated extremely rapidly to temperatures high enough in the undercooled liquid region on a time scale much shorter than that associated with the onset of crystallization. Preferably, the heating rate utilized must be high enough to suppress crystallization throughout the undercooled liquid region. For typical bulk-glass formers, the "critical heating rate" to bypass crystallization by heating through the entire undercooled region (i.e., from T_g to the melting point) is known to be on the order of 10^4 K/s [49], and can be as low as $\sim 10^2$ K/s for very robust glass formers [23]. But conventional heating methods, where heat is introduced at the boundaries, are incapable of heating the entirety of bulk-glass samples at such high rates due to a sluggish thermal relaxation. Consider for example an amorphous rod with diameter $d = 0.5$ cm and thermal diffusivity $\alpha = 0.03$ cm^2/s (typical for metallic glasses) heated very rapidly over a surface skin (e.g., by high frequency induction). The relaxation time would be $\tau = (d/2)^2/\alpha \sim 1$s. Hence, to raise the centerline temperature by $\sim 10^2$K the heating rate would be of order 10^2K/s regardless of how rapidly the surface is heated. Such a heating rate is significantly lower than "critical heating rates" for typical glass formers, and barely on the order of those for very robust bulk-glass formers. Therefore, 5-mm diameter rods of typical bulk-glass formers would crystallize at the core (and eventually throughout) irrespective of how rapidly their surface is being heated, while 5-mm diameter rods of very robust bulk-glass formers may remain marginally amorphous or barely crystallize.

The Joule heating approach introduced by Chapter 1 generates heat "volumetrically" through a metallic glass such that it overcomes the limitations imposed by thermal relaxation.[1] In this approach, electrical current generated by discharging a capacitor across the sample passes uniformly

through the sample enabling heating of the sample homogeneously throughout via dissipation of electrical energy. Since heating is volumetric, the transient temperature distribution is essentially homogenous and free of any gradients. Consequently, the sample is heated homogenously at a rate governed by the internal time constant of the electrical discharge circuit, i.e., by the current rise time. As such, the rate of homogeneous heating of a metallic glass can be controlled almost entirely by the parameters of the electrical circuit, i.e., by the capacitor discharge time constant. Capacitor discharge time constants can be varied enormously over many orders of magnitudes, covering ranges from microseconds to seconds. This allows a broad range of homogeneous heating rates that could be applied to entirely bypass crystallization (i.e., exceed critical heating rates) in a broad range of metallic glasses, from marginal glass formers to highly robust bulk-glass formers. Therefore, by properly designing the capacitor discharge characteristics, the entire undercooled liquid region of a metallic glass could be accessed for processing independent of the glass stability against crystallization, where any desired viscosity (e.g. in the range of $10^0 - 10^4$ Pa·s) can be "dialed in" simply by selecting a discharge voltage. This is a powerful method that has the potential to entirely overcome the limitations imposed by the rapidly intervening crystallization during heating of metallic gasses.

2.3 Results

In Chapter 1 it was demonstrated that the rapid capacitive discharge heating method enables near-net thermoplastic shaping by injection molding.[1] In the current work we use $Zr_{35}Ti_{30}Cu_{7.5}Be_{27.5}$ as a model bulk-glass former to explore the thermoplastic process window throughout the undercooled liquid region. Specifically, we employ high-speed infrared thermography and pyrometry to track the evolution of temperature distribution in ohmically heated bulk samples, and accurately assess process windows defined between glass transition and crystallization by identifying the signatures for glass relaxation and liquid crystallization. By plotting the onsets of crystallization at the various temperatures in the undercooling region, the TTT diagram on heating is constructed. Lastly, thermoplastic forming by near-net forging in the optimum viscosity range of $10^0 - 10^4$ Pa·s

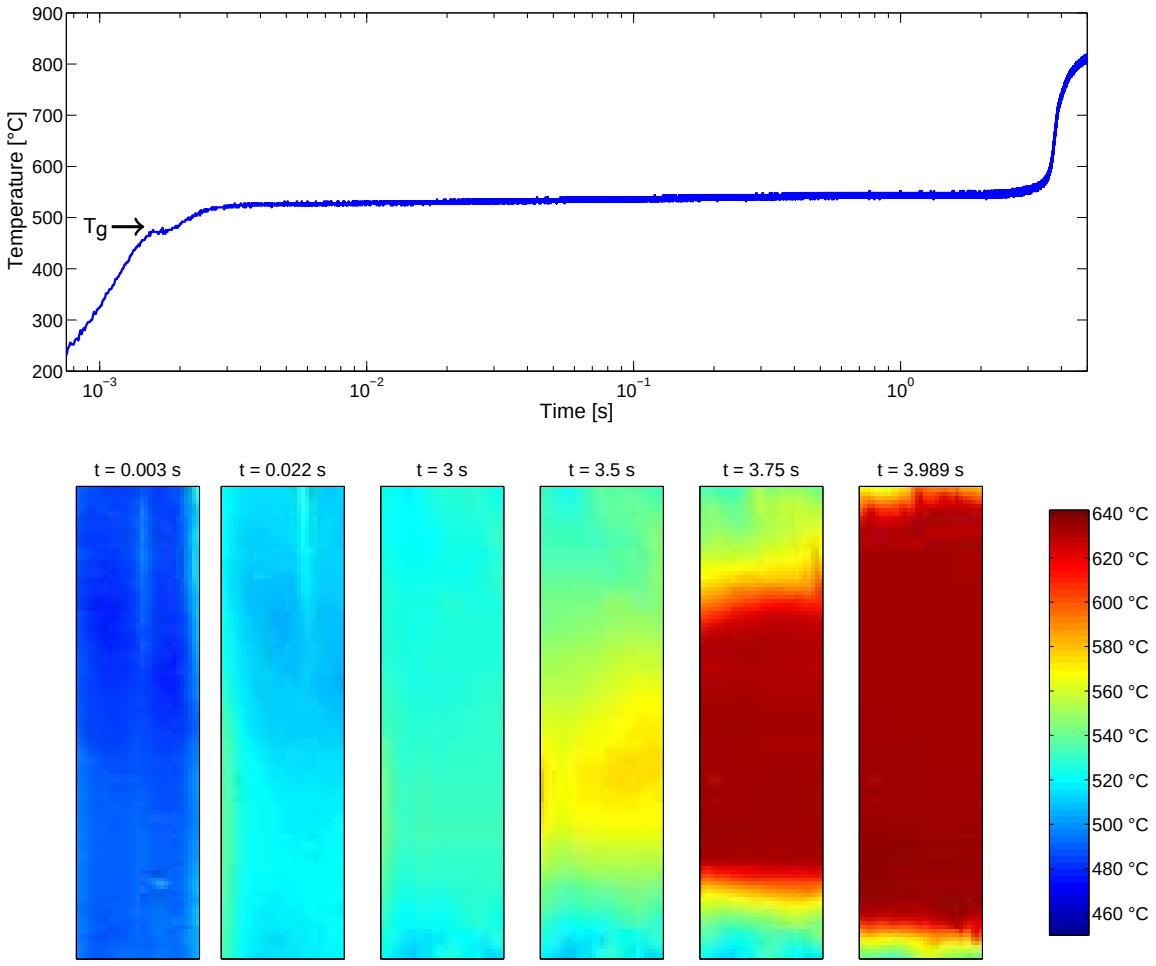

Figure 2.1: Local temperature response (A) and distribution of heating evolution at various times (B) of an ohmically heated $Zr_{35}Ti_{30}Cu_{7.5}Be_{27.5}$ metallic glass rod. The arrow at the response curve designates the glass-transition temperature. Reproduced with permission from [2].

is presented.

The temperature history and heating evolution in $Zr_{35}Ti_{30}Cu_{7.5}Be_{27.5}$ rods and strips undergoing ohmic heating at various discharge voltages were monitored by a high-speed pyrometer and a high-speed infrared imaging camera. The temperature history and heating evolution in the rod at a discharge voltage of 131.4 V associated with an energy density of 1883 J/cc is presented in Fig. 2.1. In Fig. 2.1A, the local temperature response reveals a heating rise time of about 2 ms, over which the heating process saturates as the current pulse fades and the temperature stabilizes at about 530°C. At this temperature the liquid viscosity is anticipated to be about 10^2 Pa·s [12]. The signature of a dynamic glass transition is revealed at approximately 475°C, which is 170°C higher than the

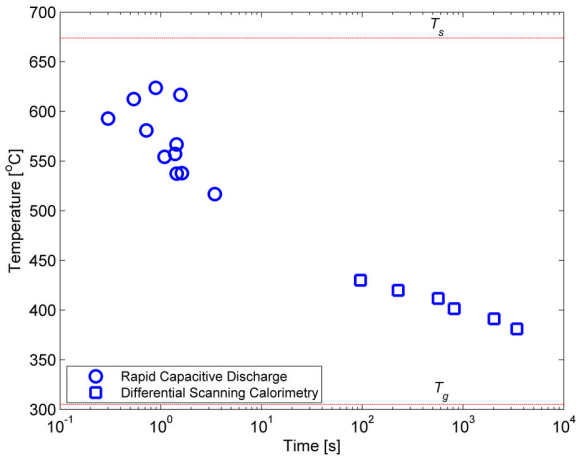

Figure 2.2: TTT diagram on heating of $Zr_{35}Ti_{30}Cu_{7.5}Be_{27.5}$ metallic glass. High temperature data were obtained by rapid capacitive discharge heating (present work), while low temperature data were gathered using differential scanning calorimetry[12]. Reproduced with permission from [2].

calorimetric glass transition (measured at 20 K/min) for this glass[12]. This is a consequence of a very high heating rate, estimated to be of order 10^5 K/s. Following the cessation of heating at 530°C, the temperature appears to remain fairly stable for a period of about 3 s. Just after 3 s a fairly sharp recalescence event is evident in the pyrometer trace, as the sample begins to crystallize at the monitored location. In Fig. 2.1B, these events are revealed over a spatial range in the rod. During heating as well as after the heating process saturates, the temperature appears fairly uniform and stable across the entire domain monitored. Uniform and stable temperature persists for a period of up to 3 s, beyond which a "nucleus" of heat evolves at the core of the sample, which rapidly spikes to over 640°C while it propagates outwards to consume the entire sample at a speed on the order of ∼1 cm/s. The sharpness of the recalescence event, which is consistent with that seen in scanning calorimetry[12], suggests that the liquid crystallizes by coupled eutectic growth. From Figs. 2.1A and 2.1B therefore, a "thermoplastic process window" of about 2 - 3 s at 530°C is revealed where the liquid viscosity is expected to be about 10^2 Pa·s.

The temperature-time crystallization onsets in the ohmic heating experiments performed at various discharge voltages over multiple samples were determined using the slope intercept method and are plotted in Fig. 2.2. The onsets obtained for the same glass at lower temperatures and longer times using differential scanning calorimetry [12] are also superimposed in the plot of Fig. 2.2. Figure

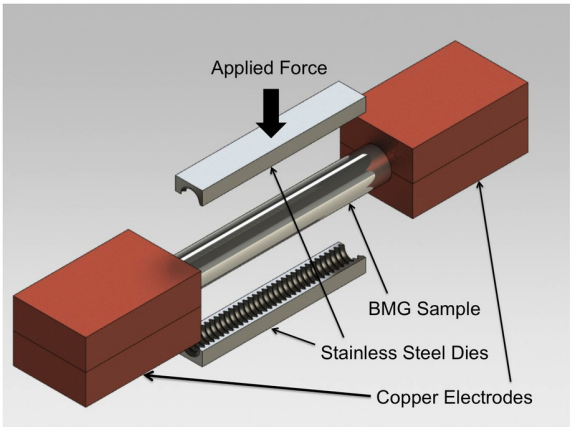

Figure 2.3: Schematic of the capacitive-discharge forging configuration, showing the die, electrodes, and metallic glass sample. Reproduced with permission from [2].

2.2 represents a TTT diagram associated with the heating a metallic glass spanning across the entire undercooled liquid region, and is the first such diagram studied using thermally equilibrated bulk samples. Previous attempts either utilized uniform heating of micrometer-thick ribbons [49], or involved surface heating of bulk samples [23]. A "critical heating rate" of ∼1000 K/s can be estimated from the TTT diagram, associated with a "nose" temperature of 593°C and a "nose" time of 0.3 s. Circling back to the discussion on thermal relaxation, the critical heating rate of $Zr_{35}Ti_{30}Cu_{7.5}Be_{27.5}$ is considerably higher than the centerline heating rate in a surface-heated 5-cm rod which would be limited by thermal relaxation. This suggests that a 5-cm rod of $Zr_{35}Ti_{30}Cu_{7.5}Be_{27.5}$ glass heated rapidly at the surface would likely crystallize before or right after it accesses the optimum viscosity range for thermoplastic processing.

To demonstrate the potential of the rapid capacitive discharge method for thermoplastic processing, a near-net forging operation is attempted within the thermoplastic process window identified near 530°C. Unlike the injection molding process outlined in Chapter 1, where the electrodes also act as plungers, in forging the ohmic heating process is decoupled from the shaping process, with the forging dies operating independently from the electrodes.[1] The process is presented schematically in Fig. 2.3, which illustrates forging a screw from a metallic glass rod. The rod is ohmically heated via the electrodes, while the forging dies subsequently (while the rod remains at the process temperature) apply a deformational force to shape the rod into a screw while simultaneously quench

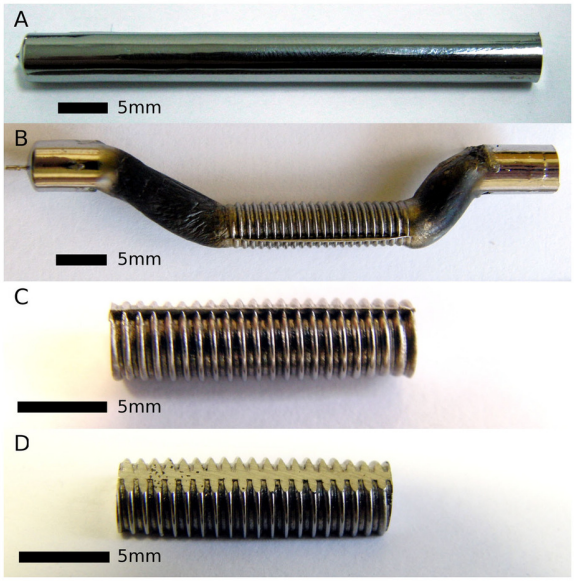

Figure 2.4: Images of a $Zr_{35}Ti_{30}Cu_{7.5}Be_{27.5}$ metallic glass feedstock rod (A), an as-processed metallic glass sample (B), a forged metallic glass screw part (C), and a post-processed metallic glass screw part (D). Reproduced with permission from [2].

the sample to revitrify it.

Forging of a 5 mm amorphous $Zr_{35}Ti_{30}Cu_{7.5}Be_{27.5}$ rod (shown Fig. 2.4A) into a threaded screw is performed using process conditions similar to those that gave rise to the process window around 530°C. A digital image of the as-processed rod is shown in Fig. 2.4B. The screw component of the rod that has undergone forging is the part in the middle. The unforged part of the rod that has free cooled in air shows significant oxidation; however, the forged part visibly appears entirely free of oxidation. Using x-ray diffraction it was also verified that the forged part is entirely amorphous. The sectioned forged screw part is presented in Fig. 2.4C, while Fig. 2.4D shows the screw with the flashing removed. To examine the near-net forging precision, the threads were imaged with scanning electron microscopy. In Fig. 2.5A, the threads on a standard steel 10-32 screw is presented. The threads on the forging die are presented in Fig. 2.5B while the threads on the forged metallic glass screw are presented in Fig. 2.5C. As can be seen, the forged metallic glass screw has finely replicated the die, and the threads closely match those of the standard steel screw.

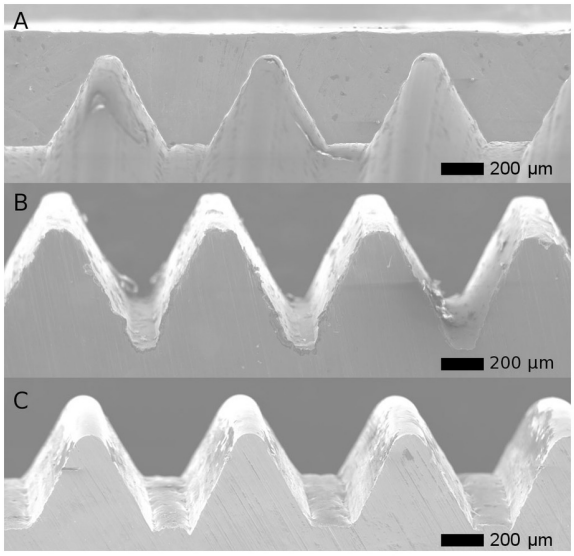

Figure 2.5: Scanning electron micrograph of the threads on a standard 10-32 steel screw (A), on the forging die (B), and on the forged metallic glass screw (C). Reproduced with permission from [2].

2.4 Conclusion

In conclusion, the rapid capacitive discharge heating method is demonstrated here to be a powerful method capable of overcoming the shortcomings of metallic glasses in thermoplastic processing. Specifically, the method is capable of applying homogeneous heating rates that could entirely bypass crystallization in a broad range of metallic glasses, from marginal glass formers to highly robust bulk-glass formers, enabling access to the entire undercooled liquid region where any desired viscosity could be "dialed in" for thermoplastic processing. Lastly, the application of the rapid discharge heating process for near-net shape processing of metallic glasses presented can have a profound impact on the commercialization and overall technology scale-up of metallic glasses. The demonstrated ability to thermoplastically process a very high strength metal into high-precision near-net shapes is already quite an achievement, as was highlighted in prior literature [19, 40, 41, 42, 43, 15, 44, 14, 13]. But the ability to conduct such thermoplastic processing in open air over millisecond timescales using shaping pressures comparable to those used in the processing of plastics, and at temperatures below typical tempering temperatures for conventional tooling, as demonstrated here, represents a significant technological leap forward.

2.5 Methods

To generate the heating curves, amorphous $Zr_{35}Ti_{30}Cu_{7.5}Be_{27.5}$ rods 5 mm in diameter 5 cm in length and strips 1 mm in thickness, 7 mm in width, and 4 cm in length were prepared by arc-melting in a water-cooled copper hearth under inert atmosphere followed by suction casting in a copper mold. A high speed infrared imaging camera (FLIR Corp., SC2500) with a spectral band from 0.9 to 1.7 μm outfitted with a bandpass filter allowing wavelengths from 1.5 to 1.9 μm was employed at frame rates of 250 - 994 frames/s to record the evolution of temperature distribution. An IMPAC IGA740-LO high-speed infrared pyrometer with a spectral band from 1.58 to 2.2 μm and a response time of 6 microseconds was also used to record temperature vs. time over a circular focal spot of $\sim$1 mm diameter near the rod center. Both camera and pyrometer were calibrated simultaneously by tracking the melting of $Pd_{43}Ni_{10}Cu_{27}P_{20}$ alloy with a solidus temperature of 531°C, which is within the temperature range considered in this work. Using this method, emissivities of 0.285 and 0.26 were found for the infrared camera and pyrometer, respectively. The emissivities are believed to be roughly representative of $Zr_{35}Ti_{30}Cu_{7.5}Be_{27.5}$ and that the temperature error is expected to be limited to within ±20°C. Ohmic heating of the amorphous $Zr_{35}Ti_{30}Cu_{7.5}Be_{27.5}$ samples was performed using a 0.264 F capacitor bank with a current rise time of about 1 ms was used at voltages ranging between $40 - 140$ V.

For the forging operation, a split die was fabricated from stainless steel with half of a 1.8 cm long 10-32 thread on each side. A 5 mm amorphous $Zr_{35}Ti_{30}Cu_{7.5}Be_{27.5}$ rod prepared as described above was placed between the dies and held in place with copper leads. A 0.792 F capacitor bank was charged to 94 V depositing 2080 J/cc of electrical energy into the sample with a current rise time of about 10 ms. The initiation of the capacitive discharge is detected by a sensor circuit measuring current in a portion of the discharge circuit. The detection of discharge activates a pneumatic valve to apply a force of 3 kN to the softened metallic glass via a pneumatic piston. A delay of approximately 10 ms occurs between the activation of the valve and contact between the die and the sample, due to mechanical constraints of the piston. The process was performed in open air.

Chapter 3

Shaping metallic glasses by electromagnetic pulsing

3.1 Abstract

With damage tolerance rivaling advanced engineering alloys and thermoplastic forming capabilities analogous to conventional plastics, metallic glasses are emerging as a modern engineering material. Here, we take advantage of their unique electrical and rheological properties along with the classic Lorentz force concept to demonstrate that electromagnetic coupling of electric current and a magnetic field can thermoplastically shape a metallic glass without conventional heating sources or applied mechanical forces. Specifically, we identify a process window where application of an electric current pulse in the presence of a normally directed magnetic field can ohmically heat a metallic glass to a softened state, while simultaneously inducing a large enough magnetic body force to plastically shape it. The heating and shaping is performed on millisecond time scales, effectively bypassing crystallization producing fully amorphous shaped parts. This electromagnetic forming approach lays the groundwork for a versatile, time and energy efficient manufacturing platform for ultra-strong metals.

3.2 Introduction

The concept of a Lorentz force generated on a current-carrying conductor exposed to a magnetic field dates back to the 19^{th} century work of Faraday and Maxwell on electromagnetism[50]. In this concept, moving point charges comprising the electric current experience Lorentz forces which consist of electric and magnetic force components. The magnetic point forces combine to produce a magnetic body force, often referred to as the Laplace force, acting on the current-carrying conductor. If the conductor is a metallic glass, the Laplace force provides for innovative methods of forming. Owing to unique electrical resistivities, metallic glasses can be rapidly and uniformly heated when electrical energy is dissipated in them[1, 51, 2]. Combining ohmic dissipation with the application of Laplace force creates a powerful platform to process metallic glasses.

While metallic glasses are generally known for their attractive mechanical properties[52, 53], perhaps their most promising attribute is their potential for "thermoplastic" processing[12, 16, 54, 18, 14, 44, 13]. By virtue of being glasses, they can be softened to viscous liquid states above the glass transition where viscoplastic shaping can be carried out in a manner similar to that applied to process conventional thermoplastics. Unfortunately, this potential for thermoplastic forming is practically limited by the rapidly intervening crystallization of the relaxed "supercooled" liquid. Electrical discharge heating has recently emerged as an effective means to overcome this limitation[1, 51, 2]. It enables rapid and spatially uniform heating to low viscosity states considered to be optimal for thermoplastic shaping, over time scales sufficiently short to bypass crystallization. In this work we demonstrate that subjecting the metallic glass to an intense electric current pulse directed normal to an applied magnetic field can generate Laplace forces sufficiently large to perform thermoplastic shaping operations, thereby producing high quality net-shaped metallic glass articles.

Electromagnetic forming of conventional (i.e. crystalline) metals has been explored since the late 1950s[55, 56]. In the most widely used approach, an induction coil excited by a current pulse generates a transient magnetic field that induces eddy currents in a workpiece according to Faradays law of induction. The coupling of the eddy currents and the magnetic field produce a repulsive Lorentz force, in accordance with Lenzs law, which accelerates the workpiece away from the restrained coil

and against a tool, causing it to form. This approach results in high workpiece velocities (typically > 100 m/s) and strain rates on the order of 10^4 s^{-1} during forming[57, 56]. Although some heat may be generated in the sample by induction, the forming process takes place entirely in the solid (i.e. the crystalline) state. Typically, the generated Lorentz forces must be high enough to generate an equivalent impact pressure (typically hundreds of MPa) that exceeds the material yield strength, thereby enabling large plastic deformation. The metallic sample must therefore have high electrical conductivity, low yield strength, and also be of limited thickness. Because of these requirements, electromagnetic forming of metals has so far been limited mostly to aluminum and copper in thin sheet and tube geometries, while stronger, less conductive metals such as steels have been largely excluded.

Compared to crystalline metals, amorphous metals demonstrate considerably higher room-temperature yield strengths (1 to 2 orders of magnitude higher than copper and aluminum)[52, 53]. However, in their relaxed viscous state above the glass transition the flow stresses are much lower (on the order of tens of MPa or less at temperatures substantially higher than the glass transition)[35], and the associated viscosities within the range where conventional plastics are typically processed (i.e. $10^0 - 10^4$ Pa·s)[58, 19]. Processing a metallic glass in this optimum rheological window is limited by crystallization of the supercooled liquid, which typically limits the available processing time to under a second. As such, a rapid forming approach for metallic glasses that utilizes an intense electromagnetic pulse to thermoplastically shape a bulk metallic glass in its relaxed viscous state would be attractive, as it would require much lower forming stresses than conventional aluminum and copper while final metallic glass parts would be considerably stronger.

Another fundamental distinction between crystalline and amorphous metals is their different electrical resistivities. Most amorphous metals exhibit electrical resistivities in the range of 150-200 $\mu\Omega$·cm[59], which are much larger than those of crystalline metals (typically 1-50 $\mu\Omega$·cm). Furthermore, unlike crystalline metals, the electrical resistivity of amorphous metals is nearly constant or even decreasing with temperature[21]. The large and temperature independent electrical resistivity hinders generation of large magnetic pressures during conventional electromagnetic forming,

however, it enables efficient and stable volumetric heating by uniform ohmic dissipation. Indeed, it has been shown that ohmic heating of metallic glasses can be both rapid and uniform, enabling thermoplastic processing at temperatures far above the glass transition[1, 51, 2]. In this work we demonstrate that the electrical and rheological properties of metallic glasses are such that a window exists for an electromagnetic forming process. Specifically, we show that by coupling a uniform electric current with an applied static magnetic field, one can simultaneously bring a metallic glass to a low viscosity state while exploiting the accompanying Laplace force to form the sample to a net shape, all while avoiding crystallization.

To process metallic glasses thermoplastically by electromagnetic forming, it is essential that the processes of ohmic heating and magnetic forming are independently controlled. This requires that the electric current, which travels through the metallic glass dissipating electrical energy and producing volumetric heating, be controlled independently of the magnetic field, which interacts with the electric current to generate the magnetic force. This is achieved by placing the metallic glass in series with an electric current source directed transverse to an independently applied magnetic field. Such a configuration is shown in Fig. 3.1, where a metallic glass sample is connected in series to a capacitor via electrodes while situated transverse to a magnetic field generated by two permanent magnets. Application of an intense electric current pulse ohmically heats the metallic glass rapidly and uniformly to a predetermined temperature in the supercooled liquid region, while the coupling between electric current and magnetic field generates a force pulse on the sample urging it against a permanent die tool, where it forms and subsequently cools and revitrifies. Here, we show that typical currents produced by discharge of a conventional capacitor and typical magnetic field strengths generated by conventional permanent magnets are adequate to rapidly and uniformly heat a bulk metallic glass sample to a low viscosity state and thermoplastically shape it against a die tool prior to the intervention of crystallization.

The Laplace force on a current-carrying conductor exposed to a magnetic field is given by $\vec{F} = I\vec{\ell} \times \vec{B}$, where I is the current traveling through the conductor, $\vec{B}$ is the strength of the magnetic field, and $\vec{\ell}$ is a conductor length vector along the current direction that traverses the magnetic field.

When the magnetic field normal to $\vec{\ell}$, the magnitude of the Laplace force reaches a maximum given by $F = BI\ell$, while any non-parallel configuration of $\vec{B}$ and $\vec{\ell}$ produces a fraction of this maximum value. For a typical metallic glass, one can show that the time-average current I discharged on a time constant τ required to ohmically heat a sample to a temperature in the supercooled liquid region where the viscosity is on the order of $\sim 10^2$ Pa·s is approximately (see Section B.1):

$$I \approx Cwt\tau^{-1/2} \tag{3.1}$$

where t is the sample thickness in the direction of the Laplace force, and C is a constant involving the material thermal and electrical properties, which for most metallic glasses ranges between 2×10^7 and 4×10^7 A·s$^{1/2}$/m^2 (see Section B.1). The magnitude of the applied Laplace force is then:

$$F \approx CBwt\ell\tau^{-1/2} \tag{3.2}$$

where w is the conductor projected width along the direction of the magnetic field . The pressure P exerted by the applied Laplace force is:

$$P \approx CBt\tau^{-1/2} \tag{3.3}$$

The Laplace force according to Eq. (3.1) appears dependent on the sample volume; its magnitude however can be independently controlled through B and τ. Pressure, on the other hand, which is the fundamental parameter determining the shaping capacity, scales with the sample thickness and is likewise controllable through B and τ.

As an example, a metallic glass sheet feedstock undergoing electromagnetic forming having $w = l = 100$ mm and $t = 1$ mm may be considered. Using Eqs. (3.1)-(3.3) and assuming $B \sim 1$ T, typical of a set of available permanent magnets, and $\tau \sim 1$ ms, typical of a capacitive discharge circuit, one may estimate $I \sim 10^5$ A, $F \sim 10$ kN, and $P \sim 10^5$ Pa (i.e. about 1 atm). These are on the order of forces and pressures applied in typical blow molding processes for plastics, performed

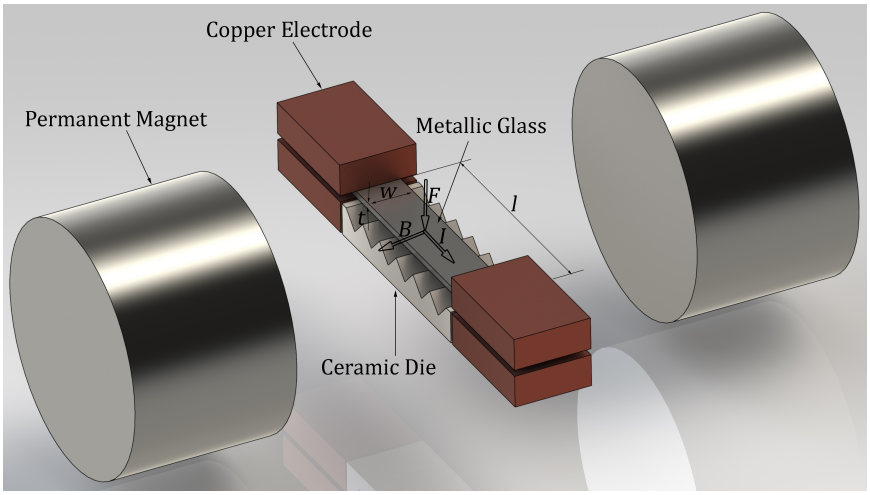

Figure 3.1: Schematic of the electromagnetic forming configuration, showing a strip of metallic glass having length l, width w, and thickness t, subject to traversing electrical and magnetic fields. The schematic shows the strip in contact with copper electrodes delivering a current I along l, and normal to a pair of permanents magnets inducing a magnetic field B. A Laplace force F is shown to be generated on the strip normal to the electric and magnetic fields (according to a left hand rule). A ceramic die is also shown placed at the side of the strip opposite to the direction of F. Reproduced with permission from [3].

at viscosities in the range of $10^0 - 10^4$ Pa·s[58, 19]. As the metallic glass would be ohmically heated to within this viscosity regime and the associated electromagnetic pressure would be on the order of typical blow molding pressures, the strains produced would likewise be comparable to those achieved in thermoplastic blow molding of plastics. Therefore, in terms of general forming capacity, electromagnetic forming of a metallic glass sheet would be akin to thermoplastic blow molding. It is also important to note the Laplace force will always be applied normal to the sheet (in the plane normal to the magnetic field). As such, the forming pressure is effectively "hydrostatic", thereby mimicking the application of gas pressure in thermoplastic blow molding.

3.3 Results

Here we demonstrate this concept by subjecting $Zr_{35}Ti_{30}Cu_{7.5}Be_{27.5}$ metallic glass strips with $\ell = 33$ mm, $w = 7$ mm, and $t = 1.0$ mm to traversing electric and magnetic fields to electromagnetically form them against permanent die tools with semicircular corrugations, as illustrated in Fig. 3.1 (see Section 3.5). A strip is placed between two FeNdB permanent magnets with its length l oriented

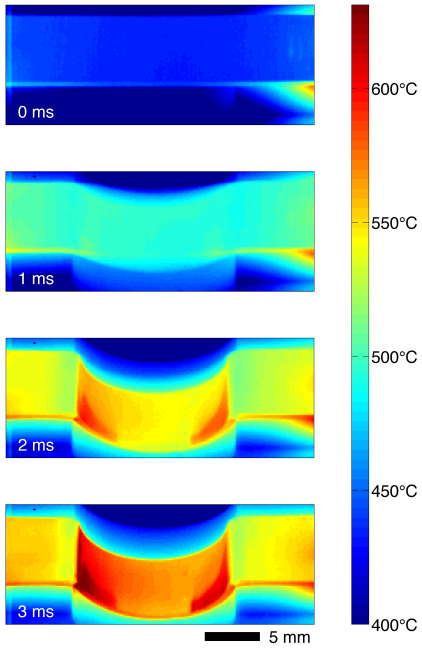

Figure 3.2: Time evolution of the temperature distribution in an amorphous $Zr_{35}Ti_{30}Cu_{7.5}Be_{27.5}$ strip undergoing heating and deformation by electromagnetic forming, as recorded by an infrared thermal imaging camera. Deformation is terminated at about 3 ms as the strip completely forms against the die (not visible by thermal imaging). Reproduced with permission from [3].

normal to the magnetic field, while a capacitor with millisecond time constant is discharged to deliver a rapid current pulse to the strip along l through the contacting electrodes. A ceramic die is placed alongside the strip where deformation would be induced by the Laplace force (i.e. normal to the electric and magnetic fields according to a "left hand rule"). A capacitive discharge circuit with 0.264 F capacitance is used, and the applied voltages ranged between 68 and 71 V. A measured magnetic field of ∼0.275 T is produced by the permanent magnets at the location of the strip. The millisecond current pulse generated by the discharging capacitor rapidly heats the metallic glass in open air to a viscous state conducive for thermoplastic forming, while the Laplace force generated by the electromagnetic interaction between electrical and magnetic fields drives the softened metallic glass against a permanent die to shape it and simultaneously cool and revitrify the sample.

The evolution of electromagnetic forming against a die with a single semicircular corrugation is captured by a thermal imaging camera and is presented in Fig. 3.2. As seen in Fig. 3.2, the strip is

heated rapidly and uniformly attaining a process temperature in the range of 500-550°C in 1-2 ms. In this temperature range the viscosity of $Zr_{35}Ti_{30}Cu_{7.5}Be_{27.5}$ is in between 10 and 100 Pa·s[12]. As the heating appears to saturate, deformation of the strip initiates owing to the generated Laplace force. The plastically deforming strip is pressed against the ceramic die (not visible by thermal imaging) forming a semicircular bow. The heating and forming process are completed over a time of $3 - 4$ ms, followed by cooling and revitrification occurring over a longer time (not shown). Crystallization is entirely avoided during the ultra-rapid heating and forming processes, as well as during cooling; the amorphous structure of the formed strip is verified by x-ray diffraction. The formed amorphous strip is shown in Fig. 3.3a. Figures 3.3b-3.3d show three more amorphous strips formed with 4, 8, and 16 semicircular corrugations produced using the same process conditions. The formed strips demonstrate a relatively fine replication of the progressively finer corrugated dies, which is a consequence of a low and fairly uniform viscosity, and also of a uniformly and hydrostatically applied force.

In Fig. 3.4 we plot the time dependent sample temperature, as monitored by an infrared pyrometer, the current through the sample as measured by a Rogowski coil, and the applied magnetic pressure as estimated by $P = BI/w$, during the heating and deformation of the strip shown in Fig. 3.2 (see Section 3.5). The time interval of the "forming region", where deformation of the strip initiates once a low enough viscosity is reached under an applied magnetic force and terminates when the strip is in full contact with the die, is indicated in all three plots. In Fig. 3.4a, the temperature is seen to rise rapidly crossing the dynamic glass transition at about 475°C (about 170°C above the calorimetric glass transition measured at 20 K/min) at about 2 ms. The temperature continues to rise in the deformation regime between 500 and 550°C but in a somewhat discontinuous manner, as the strain developing in the strip increases its electrical resistance which contributes to incrementally more efficient ohmic heating. The temperature equilibrates to about 600°C at about 6 ms. The current in Fig. 3.4b is shown to rapidly peak at slightly above 4000 A in just less than 1 ms, and then slowly declines towards zero at large time scales. The magnetic pressure as calculated from $P = BI/w$ (by assuming perfectly normal electric and magnetic fields) is plotted on the right-hand

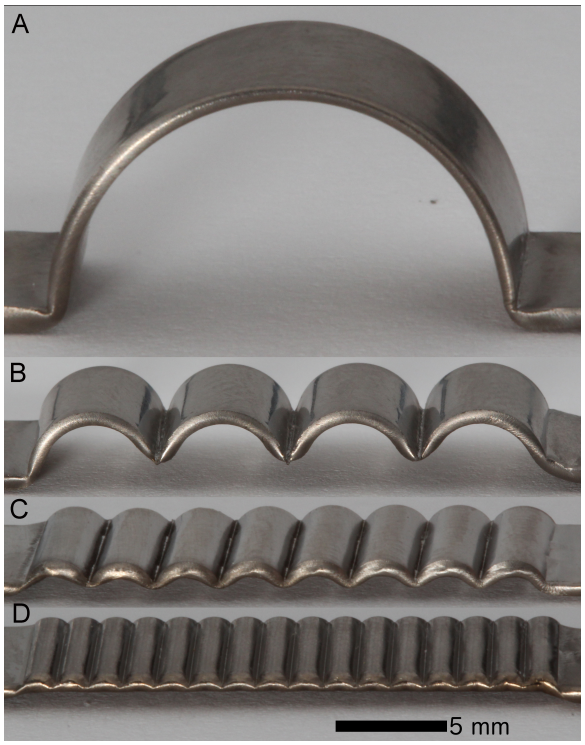

Figure 3.3: Corrugated amorphous $Zr_{35}Ti_{30}Cu_{7.5}Be_{27.5}$ strips formed electromagnetically against dies of progressively finer semicircular corrugations. Images (a)-(d) show strips formed with 1, 4, 8, and 16 semicircular corrugations. Image (a) presents the formed strip shown in the thermographs of Fig. 3.2. Reproduced with permission from [3].

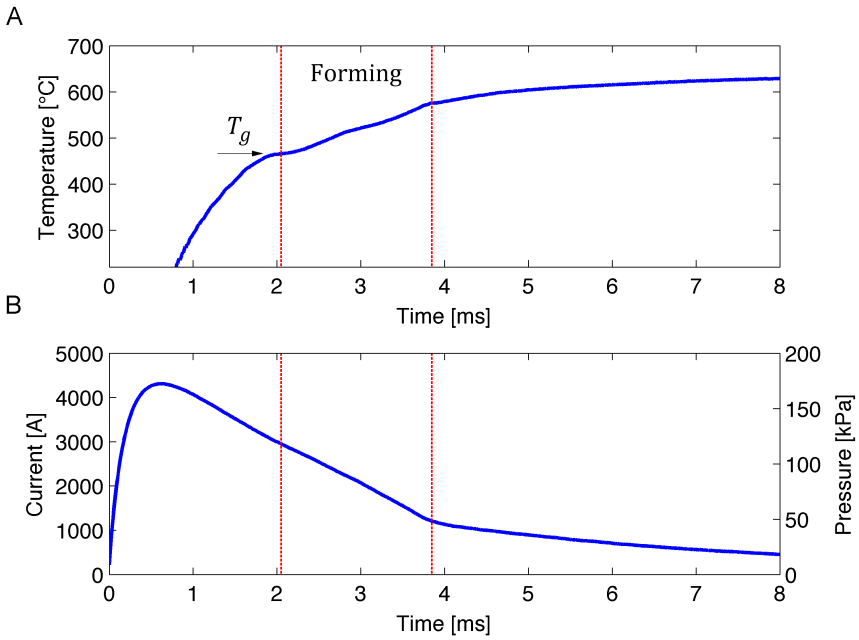

Figure 3.4: (a) Time-dependent sample temperature, as monitored by an infrared pyrometer; (b) time-dependent current through the sample as measured by a Rogowiski coil (left-hand axis) and time-dependent magnetic pressure estimated by $P = BIw$ (right-hand axis), during ohmic heating and forming of the amorphous $Zr_{35}Ti_{30}Cu_{7.5}Be_{27.5}$ strip presented in Fig. 3.2. The "forming" time interval is indicated by vertical lines in (a) and (b), and the dynamic glass-transition temperature T_g is indicated by an arrow in (a). Reproduced with permission from [3]

axis in Fig. 3.4b. With these assumptions, P is simply a linear superposition of I. The peak pressure reached in just less than 1 ms is about 170 kPa, while the pressure within the forming region declines gradually from 120 kPa to 60 kPa. These values are well within the range of pressures commonly used in thermoplastic blow molding of plastics, as discussed above.

3.4 Conclusion

In the simple configuration presented here, where current traveling through a sample is directed normal to a magnetic field induced by two permanent magnets, the magnitude of the magnetic force can be independently varied by controlling the strength of the magnetic field. But since the magnetic field in this configuration is constant, the timing of the magnetic force is solely determined by the time dependent current, and thus is not independently controllable. As shown in Fig. 3.4, being proportional to the current, the force peaks before the metallic glass reaches the least viscous

supercooled state. When the lowest viscosity state is reached, the force magnitude is lower and gradually declining. Even though force magnitudes sufficient for thermoplastic forming are achieved, the timing of the force application is not "optimal". More "optimal" timing of the process, where a constant magnetic force of a desired magnitude is applied when a desirable viscous state is reached, can be achieved by more complex electric/magnetic configurations. For instance, configurations that involve two or more successive current pulses with appropriately chosen rise times and amplitudes can achieve sequencing of the heating and forming process. Furthermore, configurations that utilize electromagnets (such as Helmholtz coils) instead of permanent magnets, where magnetic pulses with desirable profiles can be generated electrically, may achieve even more effective sequencing of the two processes.

The discussion and example above are focused on the "forging" or "stamping" of a strip or sheet using an operation mode akin to thermoplastic blow molding. The general concept introduced here could potentially be configured to perform other thermoplastic shaping operations, especially involving samples in bulk geometries. For example, using a different feedstock geometry and a different magnetic field configuration, one may be able to operate in an "injection molding" or "calendaring" (sheet extrusion) mode. Specifically, using a suitable configuration of multiple permanent magnets or electromagnets disposed at different angles relative to the electric field axis, a distribution of magnetic forces can be generated on the feedstock that are capable of guiding it through a mold runner and gate and into a mold cavity of a desirable shape, or between rollers to shape it into a sheet. As feedstock, one may use a bulk prismatic sample having $\ell = 100$ mm, $w = 10$ mm, and $t = 10$ mm. Assuming $B \sim 1$ T and $\tau \sim 1$ ms, using Eqs. 3.1-3.3 one may then estimate the current required to ohmically heat to a viscous supercooled state as $I \sim 10^5$ A, the magnetic force $F \sim 10$ kN, and the pressure $P \sim 10^6$ Pa (i.e. about 1 MPa). While I and F are on the same order as in the sheet forming process, a pressure on the order of ∼1 MPa is near the lower bound of pressures used in thermoplastic injection molding or calendaring of conventional plastics at viscosities on the order of 100-104 Pa·s[58, 19]. But as a t of 10 mm is near the upper bound of the achievable casting thickness of typical metallic glass formers and a B of 1 T is near the upper limit for conventional

permanent magnets, the window for an injection molding or calendaring process may be narrow.

The dependence of the Laplace force and pressure on the sample dimensions along with limitations in magnetic field strength may be seen as a drawback of the present approach when compared against conventional mechanical technologies (e.g. utilizing hydraulic presses, pneumatic drives, electrical motors, etc.), where larger forces and pressures are attainable. But the present concept offers unique advantages over conventional mechanical forming process. As discussed above, the Laplace force is applied normal to the deforming sample leading to pressures that are effectively hydrostatic, unlike conventional methods where forces are generally unidirectional. Furthermore, spatially-varying magnetic fields may also be designed to produce a varying direction of the Laplace force over different regions of the sample permitting complex shaping operations. From a manufacturing perspective, the absence of a working medium (i.e. the lack of presses, motors, drives, and massive fixtures) leads to an essentially frictionless process with minimal wear, and provides ease of automation. Moreover, because only the sample is accelerated during the process, large strains can be achieved in time scales significantly shorter than typical mechanical forming processes (i.e. in milliseconds rather than tens of milliseconds; see Figs. 3.2 and 3.4) such that process cycle times may be substantially reduced.

In summary, using a simple electromagnetic setup comprising a capacitor bank and a pair of permanent magnets to subject a metallic glass to traversing electric and magnetic fields, we demonstrate that the metallic glass can be formed thermoplastically in a millisecond time scale in open air in the absence of any conventional heating source or any applied mechanical force by coupling ohmic heating and magnetic forming. This simple demonstration lays the foundation for a time and energy efficient all-electronic manufacturing platform for ultra-strong metals that would rival the simplicity and economics of plastics manufacturing.

3.5 Methods

Amorphous $Zr_{35}Ti_{30}Cu_{7.5}Be_{27.5}$ strips 1 mm in thickness, 7 mm in width and 4 cm in length were prepared by arc-melting the elemental constituents in a water-cooled copper hearth under a titanium-

gettered argon atmosphere, followed by suction casting in a copper mold. The strips were ground flat and parallel, and their amorphous structure was verified by x-ray diffraction. Corrugated dies used for the shaping process were machined from MACOR ceramic.

The electromagnetic forming setup comprises a capacitor bank with capacitance of 0.264 F and rated for voltage of up to 100 V, a set of copper clamps connected to the capacitor bank via copper leads that hold the metallic glass sample and deliver the current discharge across it. Two NdFeB cylindrical magnets (3" in diameter and 2" in width) were held on either side of the sample to create a magnetic field perpendicular to current flow and parallel to the dies molding surface. The setup operates in open air. The magnetic field strength in the vicinity of the sample is measured using a hall-probe gaussmeter to be 0.275 T. Also, the time-dependent current through the sample during the electrical discharge was measured using a Rogowski coil wound around a current-carrying lead.

A high speed infrared imaging camera (FLIR Corp., SC2500) with a spectral band from 0.9 to 1.7 mm outfitted with a bandpass filter allowing wavelengths from 1.5 to 1.9 mm was employed to record the evolution of the temperature distribution and deformation at frame rates of 994-1500 frames/s. An IMPAC IGA740-LO high-speed infrared pyrometer with a spectral band from 1.58 to 2.2 mm and a response time of 6 microseconds was also used to record temperature vs. time in a circular focal spot of 1 mm diameter in the section of the strip being formed. Both camera and pyrometer were calibrated simultaneously by tracking the melting of $Pd_{43}Ni_{10}Cu_{27}P_{20}$ alloy with a solidus temperature of 531°C, which is within the temperature range considered in this work. Using this method, emissivities of 0.285 and 0.26 were found for the infrared camera and pyrometer, respectively. The emissivities are expected to be roughly representative of $Zr_{35}Ti_{30}Cu_{7.5}Be_{27.5}$ liquid in the temperature range of 450-600°C, and the temperature error is expected to be within 20°C.

Chapter 4

Measuring liquid viscosities at previously inaccessible temperatures using rapid capacitive discharge heating

4.1 Abstract

Measuring viscosities of metallic liquids in the supercooled liquid region is challenging because metastable metallic liquids have short lifetimes. The onset of crystallization prevents measurements of viscosities in the region between 10^6 and 10^1 Pa·s for most metallic glasses. Rapid capacitive discharge heats bulk metallic glasses to temperatures that access viscosities between 10^6 and 10^1 Pa·s. In combination with a parallel plate squeeze flow it is possible to measure viscosities down to 10^3 Pa·s for a variety of bulk metallis glasses.

4.2 Introduction

Above their liquidus temperatures, liquids are stable indefinitely. Thus, the hurdle for accurate rheological measurements in this temperature range is the traditional problem of handling high temperature metallic liquids. Using a variety of materials and techniques for containment of the melt, techniques such as rotating cup, capillary flow, and oscillating drop rheometry have been demonstrated to be accurate measurement techniques.[60, 61, 34] Although it is possible to achieve

significant undercooling with glass-forming liquids, the time scales required for measurements using the aforementioned techniques limits their use to at best ∼100 K below the liquidus temperature of the materials(for some of the best glass formers). This means the maximum viscosities measured by these techniques are $\sim 10^1$ Pa·s.[34]

On the other end of spectrum, liquids cooled far below their melting points can also be investigated. At temperatures around the glass transition temperature, liquids exhibit large viscosities around 10^{10} to 10^{15} Pa·s. In fact, the rheological definition of the glass transition temperature of a material, is the temperature at which the equilibrium liquid has a viscosity of 10^{12} Pa·s. Techniques employed in this regime include beam bending (for viscosities from 10^8 to 10^{13} Pa·s) and parallel plate compression (for viscosities from 10^5 to 10^8 Pa·s).[62] The upper limit for measuring viscosities in this regime occurs when the internal relaxation time $\tau = \eta/G_\eta$, where G is similar to the shear modulus and η is the viscosity, exceeds what is a practical laboratory timescale. For $Zr_{41.2}Ti_{13.8}Cu_{12.5}Ni_{10.0}Be_{22.5}$ $G_\eta = 5.5 \times 10^8$Pa, yielding a relaxation time of several days for a viscosity of 10^{13} Pa·s.[34] The lower limit for measuring viscosities is determined by the crystallization time of the material growing shorter than the timescale required to perform a viscosity measurement. This typically limits the the lowest measurable viscosities by parallel plate rheometry for the best metallic glass formers to 10^5 Pa·s.[62]

Thus, as a result of crystallization, there is a large gap in viscosity measurements in the $10^1 - 10^6$ Pa·s range. This is a critical problem for understanding the basic process of glass formation. Since the shortest crystallization times occur in this range, the glass forming ability of a liquid is determined by the kinetics of crystallization as the liquid is cooled through the $10^1 - 10^6$ Pa·s range. Because crystallization kinetics have a direct dependence on the diffusivities of various components in the alloy, and the diffusivities are related to the viscosity of the liquid by the Stokes-Einstein equation, having accurate viscosity measurements in this range is critical. In fact, there is evidence that the viscosity of an alloy at its shortest time to crystallization is directly related to the crystallization time.[63, 64] Although models can be used to interpolate between the two sets of viscosity data in order to estimate these viscosities, it is best to have direct viscosity measurements in this range.

The only option available for accessing this range is performing viscosity measurements on a much shorter timescale than is possible using traditional techniques. Whereas traditional techniques require minutes or longer to heat a sample and perform a deformation experiment, a technique which achieves the same goal in less than 1 second is demonstrated here. Capacitive discharge is employed to heat a cylindrical sample from room temperature to a process temperature in several milliseconds as described in Chapter 1. The sample is then compressed in a parallel plate fixture while compressive force, sample displacement, and sample temperature are all measured dynamically during the process. Viscosities are then calculated using the expression $\eta = Fy^2/[3v_0(dy/dt)]$. This allows for the measurement of the viscosities in the range of $10^3 - 10^6$ Pa·s of the following alloys: $Zr_{41.2}Ti_{13.8}Cu_{12.5}Ni_{10}Be_{22.3}$, $Zr_{46.75}Ti_{8.25}Cu_{7.5}Ni_{10}Be_{27.5}$, $Ni_{68.17}Cr_{8.65}Nb_{2.98}P_{16.42}B_{3.28}Si_{0.5}$, and $Pd_{77.5}Cu_6Si_{16.5}$. The two Zr-based alloys are chosen due to the large amount of viscosity measurements already published. The Pd and Ni alloys are chosen to test the ability of this method to measure viscosities in the super cooled liquid region of alloys that only had limited stability against crystallization as demonstrated by their lower ΔT values.

Table 4.1: Compositions of metallic glass alloys used in this work, their glass transition temperatures(T_g), onset temperatures for crystallization T_x, and the temperature range of the supercooled liquid region ($\Delta T = T_x - T_g$). All properties were measure at 20 K/min heating rates using differential scanning calorimetry or differential thermal analysis.

Metallic Glass Composition	T_g [K]	T_x [K]	ΔT [K]	Refs.
$Zr_{46.75}Ti_{8.25}Cu_{7.5}Ni_{10}Be_{27.5}$	622	727	105	[65]
$Zr_{41.2}Ti_{13.8}Cu_{12.5}Ni_{10}Be_{22.3}$	623	705	82	[65]
$Pd_{77.5}Cu_6Si_{16.5}$	623	700	77	[66]
$Ni_{68.17}Cr_{8.65}Nb_{2.98}P_{16.42}B_{3.28}Si_{0.5}$	400	460	60	[67]

4.3 Design

A parallel plate squeeze flow rheometer setup was chosen for two reasons. First, parallel plate squeeze flow would result in measurable forces given the strain rates and sample dimensions available, for viscosities down to 10^3 Pa·s. The upper limit of achievable strain rates of the pneumatic compression

system available was $\sim 10^2$ s^{-1}, and sample dimensions of 4 mm diameter and 12mm height were typical, resulting in forces of several newtons at sample viscosities of 10^3 Pa·s. Second, the required sample geometry for this squeeze flow was a simple cylinder, which could be easily heated using capacitive discharge. It was also possible to use the plates which compressed the sample to transmit current through the sample, further simplifying the design.

Although combining a parallel plate squeeze flow rheometer and a capacitive discharge system appears relatively simple, there important concerns to be addressed in such a design. All of these considerations stem from the large currents and voltages driven through the system by the capacitive discharge. First, in order to record meaningful data and keep the system safe for users, all portions of the system carrying large currents should be insulated using insulating plastic as shown in Fig. 4.1. Second, since there are kA currents flowing through the sample and conducting portions of the system, Lorentz forces resulting from the self-interaction of the current loop can become significant (especially when the samples soften upon heating). These forces are capable of pushing samples out from between the plates before any compression even takes place. As a result, it is vital to minimize the self-interaction of the current loop via magnetic fields. This is accomplished by aligning the conductors carrying currents to and from the sample along the sample axis, and only allowing them to change direction far away from the sample as shown in Fig. 4.1. Finally, the rapid heating of the cylindrical sample results in a large thermal expansion which puts considerable mechanical stresses on the system. $Zr_{41.2}Ti_{13.8}Cu_{12.5}Ni_{10}Be_{22.3}$ has a linear thermal expansion coefficient $\alpha \approx 9.8 \times 10^{-6}$ K^{-1}.[68] For a temperature increase of 500K this results in a 0.5% increase in length. For a 12mm sample heated in 2 ms, this corresponds to a velocity of roughly 0.3 m/s. Since the rapid expansion is accommodated by the fixture, a large momentum is imparted to the fixture, causing it to vibrate. These vibrations manifest themselves as noise in the force measurements. To eliminate this noise it it necessary to delay the onset of deformation until the vibrations are damped out. To this end a control circuit was constructed to delay the opening of a solenoid valve, applying pressure to the pneumatic piston used to compress the sample as shown in Fig. 4.1.

To determine the measurable viscosity range of this technique, it is necessary to consider the

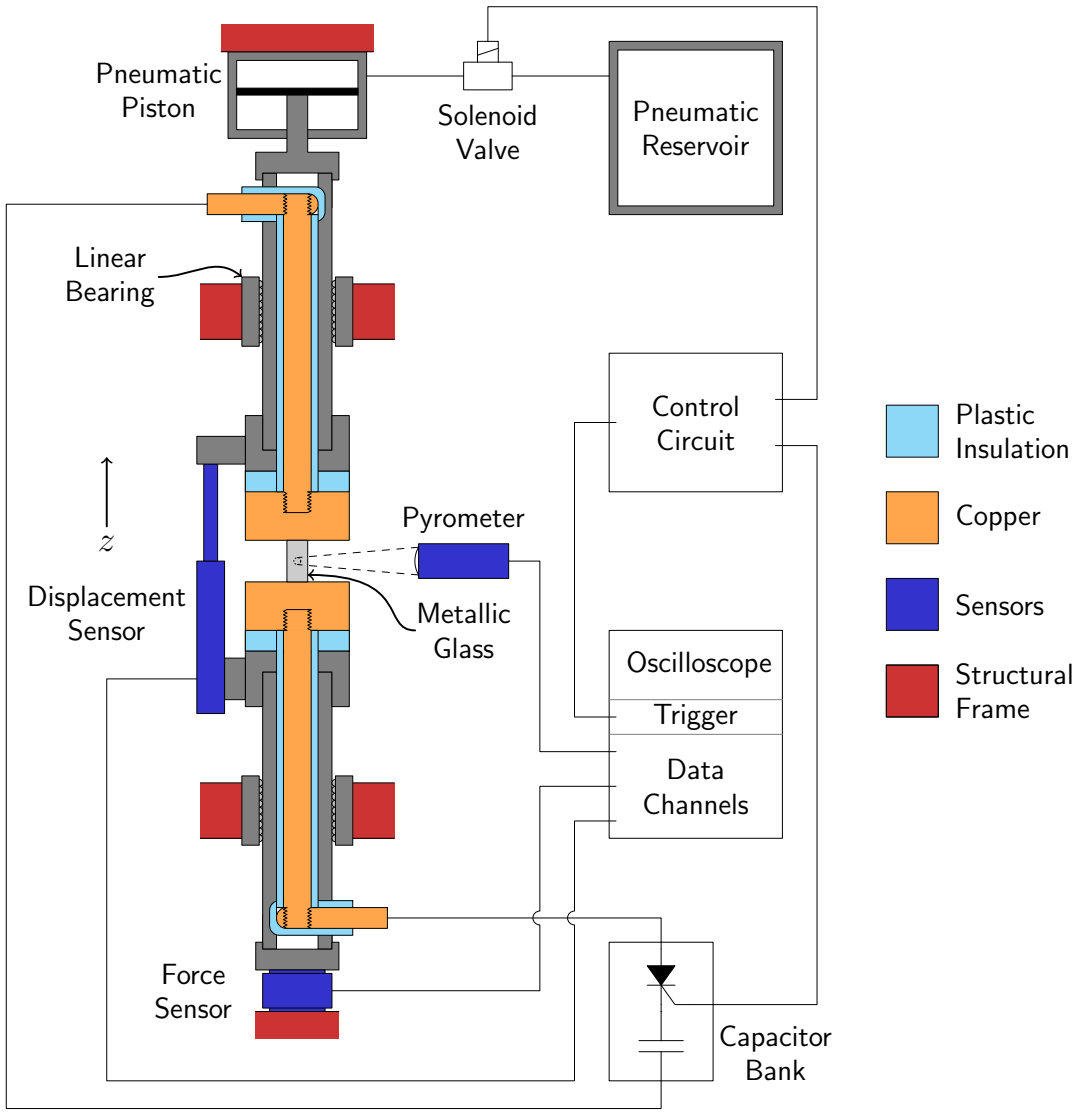

Figure 4.1: Schematic cross section of capacitive discharge parallel plate viscometer constructed in this work. In operation, the heating currents supplied by the welding power supply are routed through the sample via the copper portions of the setup. Once the metallic glass is heated, deformation is initiated by the application of pressure to the pneumatic piston. The force applied the metallic glass, its displacement in the z-direction and its temperature are all monitored during the heat and deformation process

two limiting cases. First is the case where the internal relaxation time becomes comparable to the thermal relaxation time of the sample during the experiment. This is important, as the capacitive discharge heating preferentially heats the metallic glass sample and not its surroundings, so the sample will cool off over time. Since viscosity is highly temperature dependent, it is vital that the temperature remain uniform within the sample. If using $Zr_{41.2}Ti_{13.8}Cu_{12.5}Ni_{10}Be_{22.3}$ rods with a thermal diffusivity of 2.5 mm^2/s, the thermal relaxation time of the 0.5 mm section of the sample closest to the contact with the plate is ∼100 ms.[69] This means that roughly 100 ms after heating, the sample will begin to experience significant cooling away from the contacts with the plates. Using the expression for the internal relaxation time of $Zr_{41.2}Ti_{13.8}Cu_{12.5}Ni_{10}Be_{22.3}$, we can estimate what viscosity we can reach before the internal relaxation is outpaced by the thermal relaxation of the sample. This case the upper limit for the measurable equilibrium liquid viscosity is around 10^7 Pa·s.

Second, we must examine the case where the condition for creeping flow used in the solution parallel plate squeeze flow in Appendix C.1 is violated (i.e. $Re \approx 1$). Starting with the equation for the Reynold's number, we have

$$Re = \frac{\rho v L}{\eta},$$

where ρ is the density of the fluid, v is the maximum velocity of the fluid, and L is the characteristic length scale of the geometry. To find when $Re \approx 1$, we rearrange the terms.

$$\eta_{min} = \rho v L.$$

Using a representative value of $\rho = 6000$ kg/m^3 for metallic glasses, the maximum achievable velocity of the compression fixture of ∼1 m/s, and the typical length of samples as $l \approx 0.01$ m, we find $\eta_{min} \approx 60$ Pa·s. It should be noted that measuring viscosities in the range 10^2 is already nearly impossible, due to the fact high strain rates are needed to achieve barely measurable forces. As a result, the lowest viscosities measured in this work are around 10^3 Pa·s.

4.4 Methods

Solid solutions of $Zr_{41.2}Ti_{13.8}Cu_{12.5}Ni_{10}Be_{22.3}$ and $Zr_{46.75}Ti_{8.25}Cu_{7.5}Ni_{10}Be_{27.5}$ were made by arc melting > 99.95% pure elements under a gettered Ar atmosphere. Amorphous 4mm rods were prepared by copper suction mold casting. Solid solutions of $Ni_{68.17}Cr_{8.65}Nb_{2.98}P_{16.42}B_{3.28}Si_{0.5}$ and $Pd_{77.5}Cu_6Si_{16.5}$ were prepared induction melting > 99.95% pure elements under an Ar atmosphere. The $Pd_{77.5}Cu_6Si_{16.5}$ alloy was fluxed with B_2O_3 at 1200°C for 21 hrs, and then cast into an amorphous 4 mm rod in a water quenched quartz tube from 1300°C. Amorphous 5mm rods of $Ni_{68.17}Cr_{8.65}Nb_{2.98}P_{16.42}B_{3.28}Si_{0.5}$ were prepared by counter gravity casting into copper molds under Ar atmosphere. All rods were and cut and ground to aspect ratios between 2 and 3.

An IMPAC IGA740-LO high-speed infrared pyrometer with a spectral band from 1.58 to 2.2 μm and a response time of 6 microseconds was used to record temperature vs. time over a circular focal spot of ∼1 mm diameter near the rod center. The pyrometer's emissivity setting was fixed to 0.26 and corrected for each alloy's emissivity using the SakumaHattori equation. The correction was determined by measuring the pyrometer temperature reading and the reading of an attached thermocouple for the temperature range of 220°C to roughly T_g of each alloy. Emissivities of 0.30, 0.30, 0.23, and 0.18 were found for the alloys $Zr_{41.2}Ti_{13.8}Cu_{12.5}Ni_{10}Be_{22.3}$, $Zr_{46.75}Ti_{8.25}Cu_{7.5}Ni_{10}Be_{27.5}$, $Ni_{68.17}Cr_{8.65}Nb_{2.98}P_{16.42}B_{3.28}Si_{0.5}$, and $Pd_{77.5}Cu_6Si_{16.5}$, respectively. The force applied by the compression setup was measured using a Dytran 100 lbf force sensor (Model 1051V3) connected to a power supply/signal conditioner (Model 4115B). The linear displacement of the sample was monitored using a Novotechnik TS-25A linear potentiometer. All of these signals were captured using a Tektronix DPO-2024 oscilloscope.

Samples were heated using a 0.264 F capacitor bank charged from 70 to 140 V. Deformation of the sample was delayed 50-60 ms after the heating pulse was delivered. A pneumatic piston with a 2" diameter bore was pressurized to ∼200 kPa, to deliver ∼400 N compressive force to the sample. The resulting strain rates varied from 1 to 10^2 s^{-1}. Viscosities were calculated using Eq. C.13 from

appendix C.1.

$$\eta = -\frac{Fy^2}{3v_0\dot{y}},$$

where F is the dynamic load applied to the sample, y is the height of the sample, $\dot{y}$ is the derivative with respect to time of the height of the sample, and v_0 is the initial volume of the sample.

4.5 Results

Viscosity data was collected in the range of 10^3 to 10^7 Pa·s for 4 different alloys. $Zr_{41.2}Ti_{13.8}Cu_{12.5}Ni_{10}Be_{22.3}$ and $Zr_{46.75}Ti_{8.25}Cu_{7.5}Ni_{10}Be_{27.5}$ were chosen to compare this technique to a large amount of already existing viscosity data, whereas $Ni_{68.17}Cr_{8.65}Nb_{2.98}P_{16.42}B_{3.28}Si_{0.5}$, and $Pd_{77.5}Cu_6Si_{16.5}$ were chosen to test the viability of using this technique for measuring viscosities of glass forming alloys with considerably smaller ΔT values than the Vitreloy series alloys. Recalescence (the heat release associated with crystallization) was not observed during any the viscosity experiments. The viscosity values of each alloy were fit, in combination with values from literature, to the cooperative shear model of viscosity presented by Johnson, et. al. , shown in Eq. 4.1. [70]

$$\frac{\eta_{eq}(T)}{\eta_\infty} = \exp\left\{\frac{W_g}{kT}\exp\left[2n\left(1-\frac{T}{T_g}\right)\right]\right\}, \tag{4.1}$$

where

$$W_g = kT_g\ln(\eta_g/\eta_\infty).$$

Here T_g, n, and η_∞ are all fitting parameters, while η_{eq} is the equilibrium viscosity and k_B is the Boltzmann constant. However, T_g and η_∞ have some physical significance. T_g is the temperature at which $\eta_{eq} = 10^{12}$ Pa·s and η_∞ is the high temperature limit of the viscosity. A useful parameter to determine from each fit is the "fragility index" m. m is a measure of the hyper-Arrhenius temperature dependence of the viscosity. It is defined as the steepness of $\log_{10}(\eta_{eq})$ vs. T_g/T at the glass transition temperature, as shown in Eq. 4.2[71]. For a liquid obeying an Arrhenius temperature dependence, $m = 1$, while real liquids have $m \gg 1$. m is used to classify liquids as

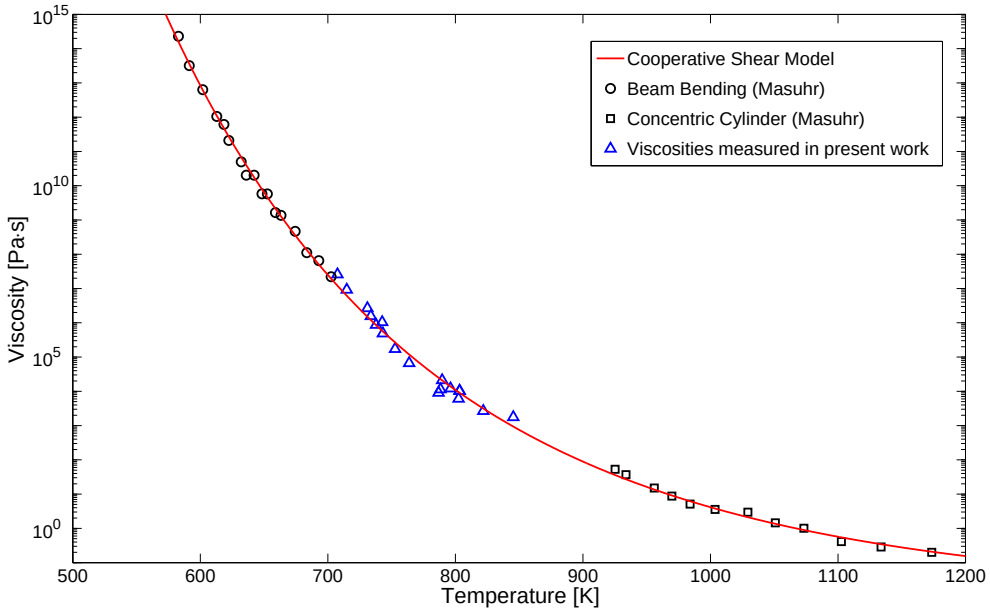

Figure 4.2: Viscosity versus temperature for $Zr_{41.2}Ti_{13.8}Cu_{12.5}Ni_{10}Be_{22.3}$ measured using capacitive discharge heating (blue triangles) compared with viscosity data reported in the literature using beam bending (black circles) and Couette viscometry (black squares) [34].

"strong" or "fragile". "Strong" liquids have lower m values while "fragile" liquids have larger m values. This implies that "fragile" liquids "fall apart" more rapidly as temperature increases than "strong" liquids. As an example, SiO_2 is considered a "strong" liquid with $m = 20$, while polystyrene is a "fragile" liquid with $m = 139$.

$$m = \left. \frac{d \log_{10} \eta_{eq}}{d(T_g/T)} \right|_{T=T_g}. \tag{4.2}$$

Evaluating the fragility of the cooperative shear model, gives the expression

$$m = (1 + 2n) \log_{10}(\eta_g/\eta_\infty), \tag{4.3}$$

where $\eta_g = 10^{12}$ Pa·s.

Fig. 4.2 summarizes viscosity measurements done on $Zr_{41.2}Ti_{13.8}Cu_{12.5}Ni_{10}Be_{22.3}$, using beam bending viscometry, couette viscometry, and the current method.[34] Fig. 4.3 summarizes viscos-

ity measurements done on $Zr_{46.75}Ti_{8.25}Cu_{7.5}Ni_{10}Be_{27.5}$, using beam bending viscometry, capillary flow viscometry, and the current method.[62] Fig. 4.4 summarizes viscosity measurements done on $Ni_{68.17}Cr_{8.65}Nb_{2.98}P_{16.42}B_{3.28}Si_{0.5}$, using beam bending viscometry and the current method. Fig. 4.5 summarizes viscosity measurements done on $Pd_{77.5}Cu_6Si_{16.5}$ using creep measurements, oscillating drop viscometry, and the current method.[61, 72] The results of the fits to the viscosity data are summarized in Table 4.2.

The viscosity data gathered for $Zr_{41.2}Ti_{13.8}Cu_{12.5}Ni_{10}Be_{22.3}$, $Zr_{46.75}Ti_{8.25}Cu_{7.5}Ni_{10}Be_{27.5}$, and $Ni_{68.17}Cr_{8.65}Nb_{2.98}P_{16.42}B_{3.28}Si_{0.5}$ in this work agree very well with previously gathered data. For both the Zr-based alloys, it can be seen that there is overlapping data in the viscosity range of 10^5 to 10^7 Pa·s, for the method developed in this work and the traditional methods of beam bending and parallel plate rheometry. For these alloys, the measured fragilities agree very closely with values from literature.[70] For the viscosities measured for $Pd_{77.5}Cu_6Si_{16.5}$, there is a sizable discrepancy between the the fragility measured in this work($m = 74$) and the fragility measured in literature ($m = 61$).[70] This is due to the fact that measured viscosities were considerably lower than what would have been expected from previous fits without the current data. A possible explanation for this may be the fact that the low temperature viscosity measurements made by Chen were performed on unfluxed material spun into ribbons, which could affect the compostition and therrmal history of the glass. If there is an offset between the two sets of viscosity values due to this difference in materials, it could have a significant impact on the fragility of the fit.

Table 4.2: Cooperative shear model fit parameters and fragility of four metallic glass alloys.

Metallic Glass Composition	T_g [K]	n	η_∞ [Pa·s]	m (Fragility)
$Zr_{41.2}Ti_{13.8}Cu_{12.5}Ni_{10}Be_{22.3}$	614	0.951	1.1×10^{-2}	40.54
$Zr_{46.75}Ti_{8.25}Cu_{7.5}Ni_{10}Be_{27.5}$	596	1.167	8.4×10^{-1}	40.26
$Ni_{68.17}Cr_{8.65}Nb_{2.98}P_{16.42}B_{3.28}Si_{0.5}$	673	1.460	2.6×10^{-3}	57.20
$Pd_{77.5}Cu_6Si_{16.5}$	638	2.174	3.5×10^{-2}	74.24

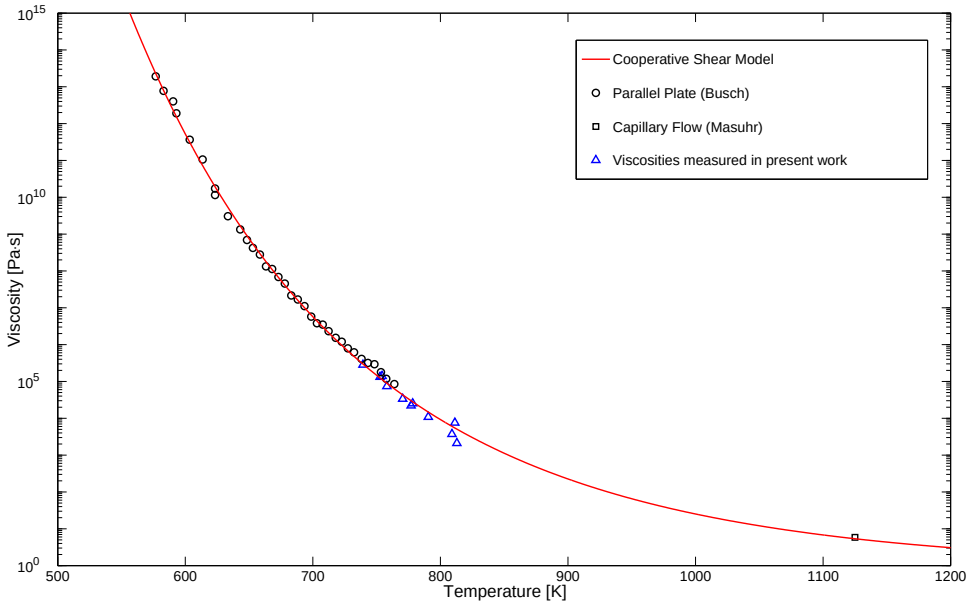

Figure 4.3: Viscosity versus temperature for $Zr_{46.75}Ti_{8.25}Cu_{7.5}Ni_{10}Be_{27.5}$ measured using capacitive discharge heating (blue triangles) compared with viscosity data reported in the literature using beam bending (black circles) and capillary flow viscometry (black squares) [62]

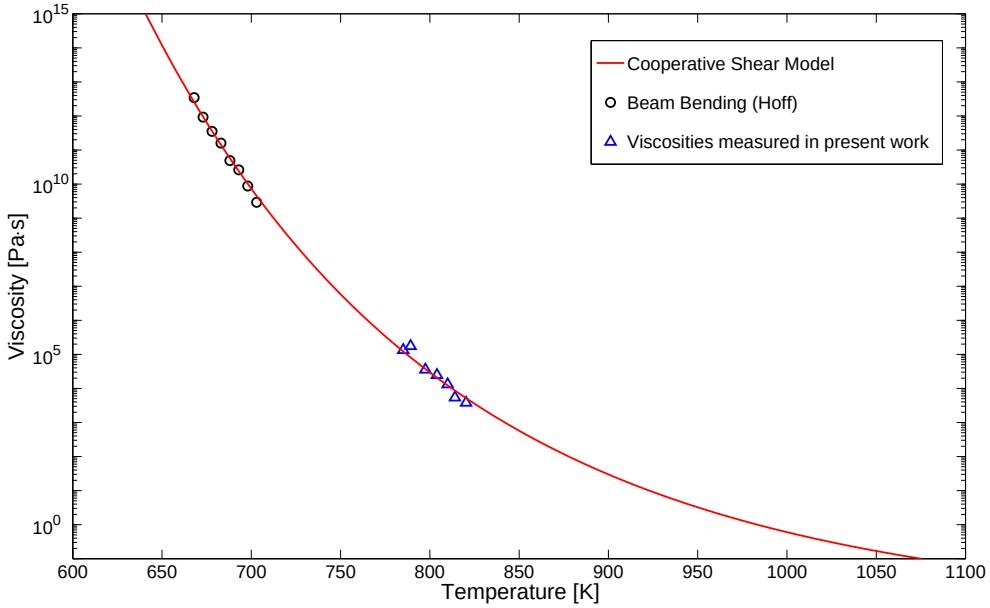

Figure 4.4: Viscosity versus temperature for $Ni_{68.17}Cr_{8.65}Nb_{2.98}P_{16.42}B_{3.28}Si_{0.5}$ measured using capacitive discharge heating (blue triangles) compared with unpublished viscosity data from Andrew Hoff (black circles) [73]

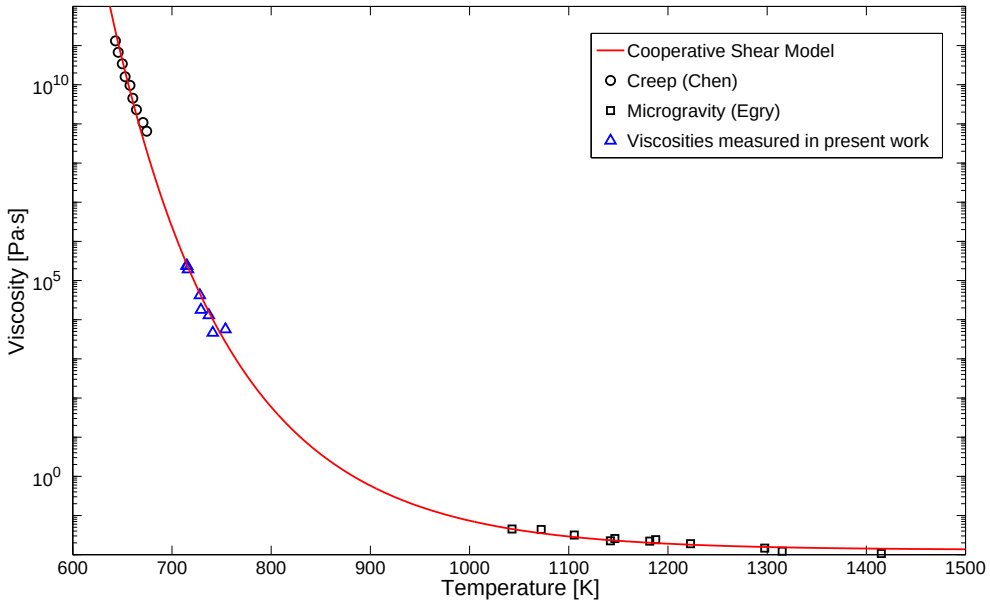

Figure 4.5: Viscosity versus temperature for $Pd_{77.5}Cu_6Si_{16.5}$ measured using capacitive discharge heating (blue triangles) compared with viscosity data reported in the literature using creep (black circles)[72] and microgravity oscillating droplet viscometry (black squares)[61]

4.6 Conclusion

The combination of capacitive discharge heating and parallel plate rheometry is a reliable method for determining viscosities in the range of 10^7 to 10^3 Pa·s. The measurement of viscosities of $Ni_{68.17}Cr_{8.65}Nb_{2.98}P_{16.42}B_{3.28}Si_{0.5}$, an alloy with a $\Delta T = 60$K, demonstrates that this technique is capable of measuring viscosities in this region even for alloys with limited thermal stability. In addition, the short timescales involved in these experiments make them ideal quickly characterizing alloy systems. The only limitation for this method is that viscosities below 10^3 Pa·s are difficult to measure using the parallel plate geometry. To measure lower viscosities, it is necessary to adopt a new flow geometry that will generate measurable forces at reasonable strain rates for viscosities below 10^3 Pa·s.

Chapter 5

Rapid pulse calorimetry of metallic glasses using capacitive discharge

5.1 Abstract

Previously, much of the calorimetry done with metallic glasses was performed using traditional calorimetry techniques, which are typically performed at heating rates around 1 K/s. Because rapid capacitive discharge heats at a rate of 10^5 or 10^6 K/s, capacitive discharge pulse calorimetry was used to measure heat capacities and enthalpies of $Zr_{46.75}Ti_{8.25}Cu_{7.5}Ni_{10}Be_{27.5}$ at a heating rate of $\sim 5 \times 10^5$ K/s. It was possible to demonstrate systematic differences in the enthalpies of specimens annealed at different temperatures. In addition, the glass transition temperatures of as-cast samples was found to be 123 K above the calorimetric glass transition measured at 0.33 K/s heating rates. Lastly, the annealing temperature was found to have a strong correlation with the glass transition temperature of each specimen.

5.2 Introduction

Since the forming operations in Chapters 1-3 employ a current pulse heating method which operates at 10^5 to 10^6 K/s, it is essential to understand the fundamentals of this heating process in order to properly control these forming methods. Specifically, it is necessary to predict charging voltages for the capacitor bank, so that the glassy feedstock is heated to the appropriate temperature. This

is a vital step in forming process, as the nature of the discharge circuit will not allow for dynamic control of the heating process. Therefore, all processing parameters have to be set beforehand. As a result, it is vital to be able to predict the enthalpy to reach a specific temperature in the supercooled liquid. An essential component of this is is to understand how the thermal history of the metallic glass interplays with the rapid heating method.

Since the 1970s, rapid current pulses have been used to obtain thermophysical properties of metals. The use of large battery banks to generate heating rates of ∼1000 K/s enabled heat capacity measurements of refractory metals at temperatures above 2000 K.[74] More, recently metallic glass ribbons have been investigated at heating rates of 10^4 k/s using similar techniques. However, when heating ribbons, it is difficult to ensure temperature uniformity in the material as the thermal relaxation time of geometry becomes very small.

Due to the rapid nature of the heating, and the relatively low temperatures involved in experiments in the super-cooled liquid region of glasses, very little heat transfer occurs during the several milliseconds during and after the capacitive discharge. Thus, for bulk($>$ 1mm thick) samples thermal conduction and radiation can be neglected during the analysis of these short timescale experiments. Thus, apart from the electrical heating done to the samples, the process can be assumed to be adiabatic. Therefore, by measuring the current run through sample, the voltage drop across it, and its temperature as the heating takes place, we can construct a calorimeter that simultaneously measures the temperature of a material and its enthalpic state during ohmic heating.

To understand how glasses behave upon heating it is important to understand how their thermal history affects their properties. As shown in Figure 5.1, when a liquid is cooled without crystallizing, its properties will eventually begin to deviate from those of the equilibrium liquid properties. Here the enthalpy of the material displays this behavior; however, many properties exhibit this behavior. This behavior has been demonstrated on the elastic moduli of a metallic glass.[75] The temperature at which this deviation begins(the glass transition temperature, T_g) and the final properties of the frozen glass are the dependent on the cooling the rate. In Fig. 5.1 Glass 1 is cooled slowly and Glass 2 is cooled rapidly, causing Glass 2 to fall out of equilibrium at higher temperature, resulting in an

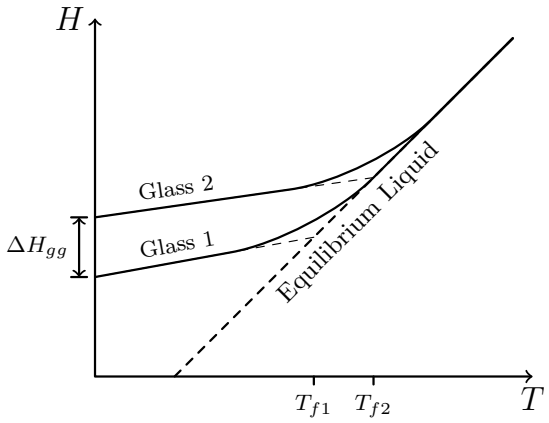

Figure 5.1: Schematic cooling curve of two glasses cooled at different rates showing enthalpy as a function of temperature. Glass 1 is cooled more slowly and stays equilibrated to lower temperatures, while Glass 2 is cooled more rapidly and falls out of equilibrium at higher temperatures.

enthalpy difference between the two glasses, ΔH_{gg}. In addition, each glass has a different fictive temperature(T_f) where the extrapolated glassy curves for H meet the equilibrium liquid curve. In a laboratory this effect is much easier to produce by annealing samples at fixed temperatures and waiting for them to become equilibrated liquids rather than varying cooling rates. It should also be noted that T_f and T_g are not the same. Although they are both related to the thermal history of the glass, T_f is fixed once the sample is frozen in a glass state. T_g on the other hand is simply the temperature at which the material changes from glassy to liquid behavior or vice versa, although it typically used in the context of heating a glass. The glass transition occurs when the relaxation time of the material ($\tau = \eta/G$, where η is the viscosity and G is the shear modulus) becomes shorter than the laboratory timescale. Therefore, when the heating rate is changed, the available time for relaxation changes and the glass transition temperature changes to accommodate for a shorter τ. However, since τ has a very steep temperature dependence, changes in heating rate typically only produce small changes in in T_g.

This is further supported by the concept of the potential energy landscapes. A potential energy landscape is the potential energy of N atoms in the $3N$ dimensional coordinate space formed by the position vectors those atoms. This highly dimensional "landscape" contains a myriad of minima, which are the stable inherent structures. A schematic of a potential energy landscape is shown

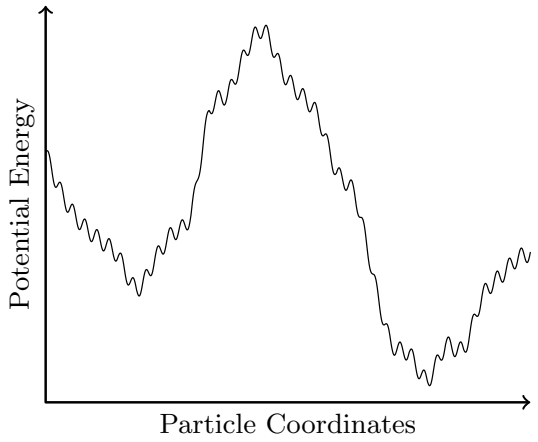

Figure 5.2: Schematic of a potential energy landscape.

in Fig. 5.2. In order to make visualization of the landscape possible, one must choose a particle coordinate or linear combination thereof to move the system along to see the potential energy basins. It is theorized that local minima populate larger "metabasins" a shown in Fig. 5.2.[76] The system moves between minima by hopping over saddle points connecting 2 minima. This thermally activated hopping allows for the system to relax stresses. Once a liquid is cooled to a sufficiently low temperature, it will be unable to move between "metabasins", becoming a glass. The rate of cooling during the process affects how far down into the landscape a system can reach before it is frozen in some local state.

5.3 Methods

A solid solution of $Zr_{46.75}Ti_{8.25}Cu_{7.5}Ni_{10}Be_{27.5}$ was perpared by arc melting $> 99.95\%$ pure elements under a gettered Ar atmosphere. Amorphous 4mm diameter rods 4.5 cm in length were prepared using copper mold suction casting. Several samples were annealed at the temperatures of 573 K, 588 K, 608 K, and 643 K for 86400, 57600, 3600, 600 seconds, respectively. Two 30 gauge copper wires were spot welded to each rod spaced 5-7 mm apart along the length of the rod, to measure the voltage difference between the spacing(ΔV). For each experiment, the rods were clamped between copper electrodes attached to a welding power supply as shown in Fig. 5.3.

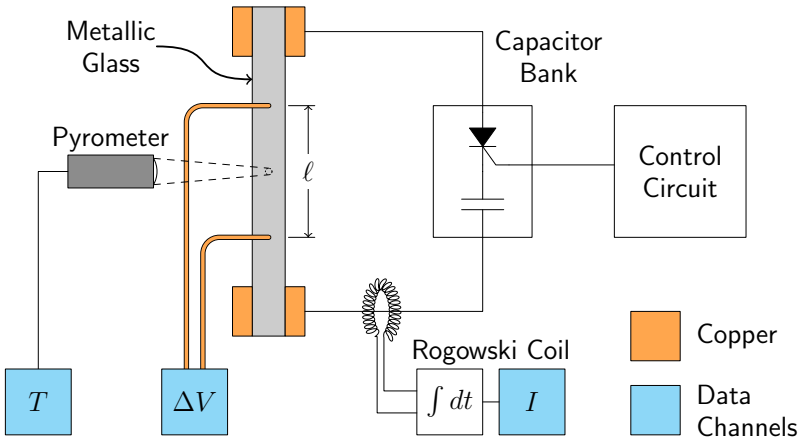

Figure 5.3: Schematic capacitive pulse calorimeter. In operation, the heating currents supplied by the welding power supply are routed through the sample copper clamps on either end of the sample. Current is measured using a rogowski coil, the voltage difference across a know section of the sample is measured using spot-welded copper leads, and the temperature is measured by a pyrometer

An IMPAC IGA740-LO high-speed infrared pyrometer capable of measuring temperatures between 200°C and 1000°C with a spectral band from 1.58 to 2.2 μm and a response time of 6 microseconds was used to record the temperature, T, over a circular focal spot of $\sim$1 mm diameter near the rod center. The pyrometer was calibrated to alloy's emissivity by adjusting the emissivity setting on the pyrometer until the temperature reading from the pyrometer matched that of an attached thermocouple for the temperature range of 220°C to roughly T_g. An emissivity of 0.28 was found to give the best agreement. A PEM CWT300LF Rogowski coil was employed to measure the current, I. All of the raw signals for T, ΔV, and I were captured using a Tektronix DPO-2024 oscilloscope.

Current pulses peaking at $\sim 10^4$ A and lasting roughly 2 ms were employed to heat the samples at heating rates varying from 4.8×10^5 to 5.5×10^5 K/s. An example of the data collected during such a heating experiment is shown in Fig. 5.4. The integral $\int_0^t \Delta V(t')I(t')dt'$ was performed numerically on the data to find the enthalpy change in the section of material between the voltage probes as a result of heating. The enthalpy change was then converted to a specific enthalpy change by dividing by $v/\rho M$, where v is the volume of the sample between the voltage probes, ρ is the density of the sample, and M is the molar mass of the alloy. An example of this enthalpy data is shown in

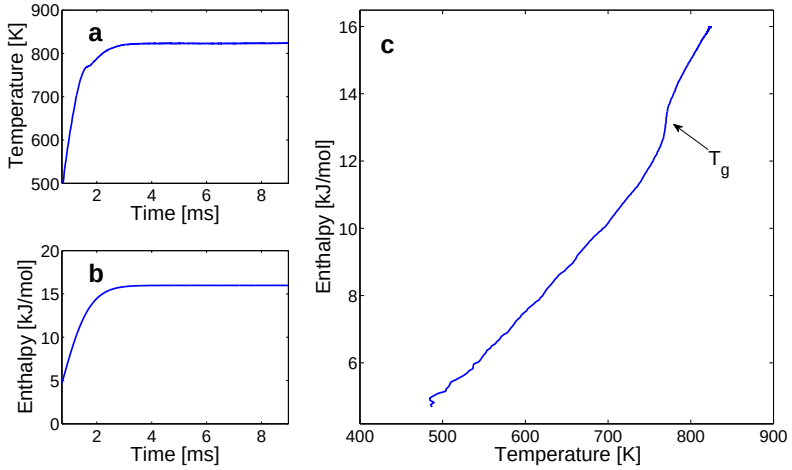

Figure 5.4: Example data set from as cast $Zr_{46.75}Ti_{8.25}Cu_{7.5}Ni_{10}Be_{27.5}$ specimen. **a** is temperature vs. time from pyrometer data. **b** is enthalpy vs. time calculated using the method described in section 5.3 **c** combines the two previous data sets into an enthalpy vs temperature plot. The glass transition is indicated by an arrow at T_g.

Fig. 5.4b, The assumption that the glassy heat capacity should be the same for alloys was used to normalize all of the data sets to make them easier compare. To remove any errors between data sets resulting from variations in the cylindrical cross section of each sample, a linear correction was applied to each data set so they would all have the same average slope.

5.4 Results

In Fig. 5.4 we can examine the enthalpy vs temperature relation of an as cast specimen. At temperatures up 750K, the material exhibits a slope that is relatively constant at around $3R$(R is the ideal gas constant), the Dolung-Petit heat capacity for solids. At 765K there is a large increase in the slope of the enthalpy curve associated with the relaxation of the material from the glassy state to the liquid state, known as the glass transition. At higher temperature the slope decreases to a value higher than the roughly $3R$ heat capacity of the glass as material approaches the liquid heat capacity.

The simplest analysis done on the data collected was to investigate the heat capacity of the glass and compare it to values from literature. All data sets were pooled and fit between the temperatures

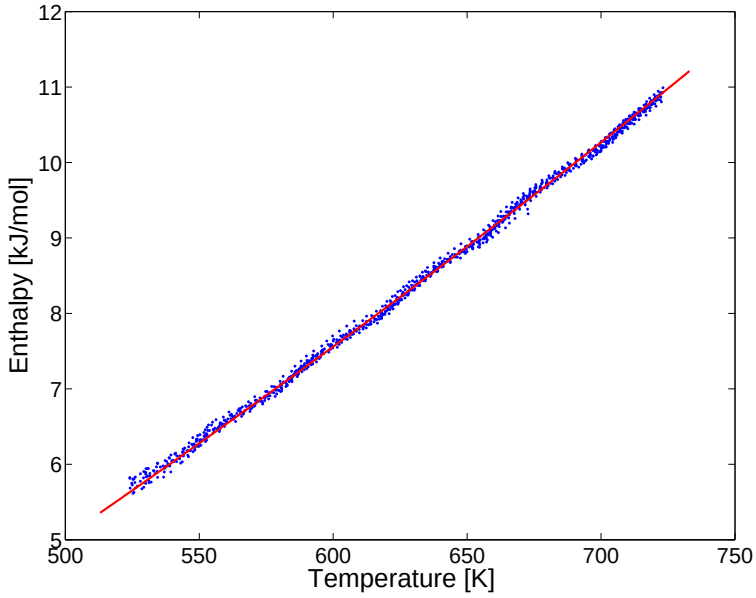

Figure 5.5: Enthalpy versus temperature for $Zr_{46.75}Ti_{8.25}Cu_{7.5}Ni_{10}Be_{27.5}$ in the glassy state. The blue dots represent data gather by the capacitive discharge pulse calorimetry method. The red line represent the fit of Eq. 5.2

523 K to 723 K to the integral of the glassy heat capacity function from Busch et. al. 1998 [77]

$$c_p^g(T) = 3R + aT + bT^2 \tag{5.1}$$

$$\Delta H_g = \int_{T_0}^{T} c_p^g(T)dT = 3RT + \frac{a}{2}T^2 + \frac{b}{3}T^3 + c, \tag{5.2}$$

where c_p^g is the glassy heat capacity, T_0 is room temperature, and a, b, and c are fitting parameters determined to be -1.51×10^{-2} J/mol·K^2, 2.82×10^{-5} J/mol·K^3, and -6.72×10^{3} J/mol, respectively. These data and fit are plotted in Fig. 5.5. As an additional check the fitted function $\Delta H_g = 0$ at a temperature of 285K, which is only several degrees from room temperature(the initial temperature of the sample). The heat capacity was computed using Eq. 5.1 with fitted values for a and b and plotted in Fig. 5.6. In addition, heat capacity measurements by step calorimetry were included for liquid and crystalline samples.[78] Fits for these data were determined using the following equations:

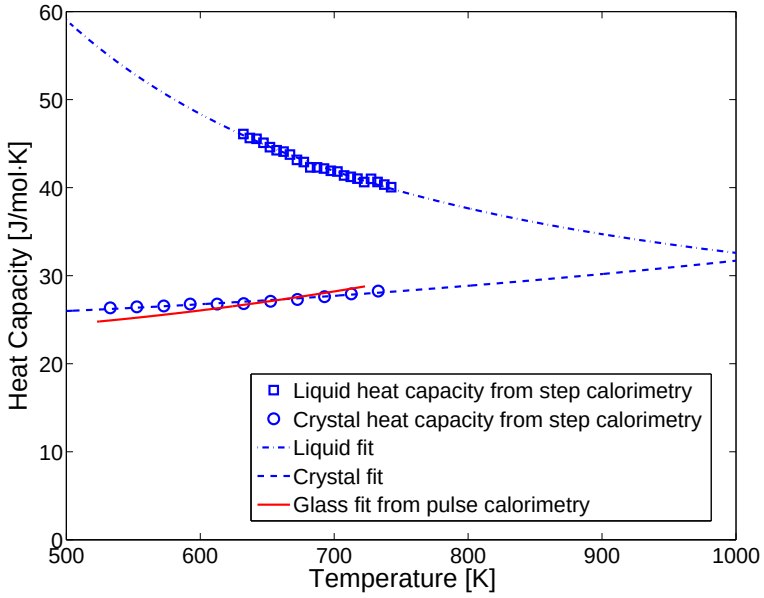

Figure 5.6: Heat capacity versus temperature for $Zr_{46.75}Ti_{8.25}Cu_{7.5}Ni_{10}Be_{27.5}$. The blue squares and circles are heat capacities of liquid and crystalline samples, respectively, measured using step calorimetry with a DSC.[78] The blue dashed-dotted and dashed line are fits to this liquid and crystalline data, respectively, using Eqs. 5.3 and 5.4. The solid red line is the heat capacity computed from the fit in Fig. 5.5

$$c_p^l(T) = 3R + dT + fT^{-2} \tag{5.3}$$

$$c_p^x(T) = 3R + gT + hT^2, \tag{5.4}$$

where c_p^l is the liquid heat capacity, c_p^x is the crystalline heat capacity, and d, f, g, and h are fitting parameters determined to be -1.00×10^{-3} J/mol·K^2, 8.65×10^6 J·K/mol, -2.58×10^{-3} J/mol·K^2, and 9.34×10^{-6} J/mol·K^2, respectively. Both the glassy and crystalline heat capacities are dominated by the $3R$ Dulong-Petit contribution of the vibrational heat capacities of harmonic oscillators. The dilatational heat capacity contribution $vB\alpha^2T$, where v is the molar volume, B in the bulk modulus, and α is the volumetric thermal expansion coefficient, would be expected to give a heat capacity contribution of $\sim 1 \times 10^{-3}$ J/mol·K$^2 \times T$ to the heat capacity using the properties of $Zr_{41.2}Ti_{13.8}Cu_{12.5}Ni_{10}Be_{22.3}$.[69] This would increase the heat capacity by ~ 0.6 J/mol·K in the

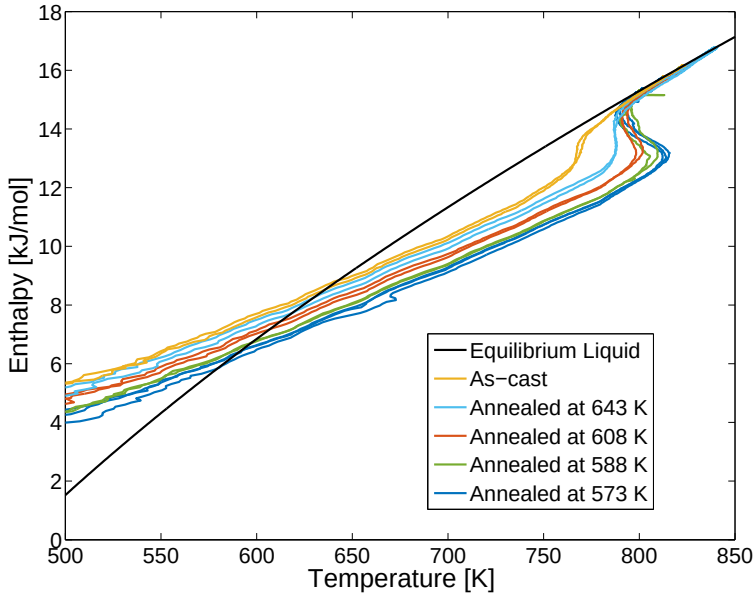

Figure 5.7: Enthalpy versus temperature for $Zr_{46.75}Ti_{8.25}Cu_{7.5}Ni_{10}Be_{27.5}$ for samples with varying thermal histories (colored lines) referenced to an equilibrium liquid enthalpy curve $H_l(T)$ (black line) generated by integrating Eq. 5.3. [62]

temperature range measured. Therefore, the average heat capacity measured for the glass of 26.6 J/mol·K is within reason for the temperatures of 523 K to 723 K.

By annealing samples to several different temperatures around T_g, an attempt was made to measure the enthalpy differences between each of the annealed states. In order to do this, an enthalpy function for the liquid was calculated by integrating Eq. 5.3 and assigning an arbitrary constant of integration. This function, $H_l(T)$, represents the amount of energy $(H_l(T_2) - H_l(T_1))$ required to change the temperature of the liquid from T_1 to T_2. It was assumed that roughly 8 ms after the initiation of the heating pulse the sample had become a full relaxed liquid due to the leveling off of the temperature at a final value, T_F. Based on this assumption, each of the enthalpy datasets was adjusted by a constant so that experimental enthalpy value $H_{exp}(T)$ at T_F coincided with the function $H_l(T)$. Since each glass with a different thermal history starts the heating experiment in a considerably different configurational state but relaxes to the same liquid, this is the best method to allow direct comparison between the enthalpy curves of all of the annealed states, as shown in Fig. 5.7.

Qualitatively examining Figure 5.7 immediately shows similarities to Fig. 5.1. It can be seen that the as-cast specimens have the highest glassy enthalpy curves followed by the glasses annealed at the higher temperatures and then those annealed at the lower temperatures. Since the equilibrium enthalpy curve for the liquid is monotonically increasing, a glass equilibrated to a liquid state at the highest temperature should have the highest quenched-in enthalpy, as confirmed by the enthalpy curves of the samples annealed at 643K. If the glassy enthalpy data is evaluated at a fixed temperature, the data from the annealed samples spans roughly 850 J. This span is somewhat smaller than the $\sim$ 1500 J expected from integrating the difference in heat capacity of the glass and the liquid in the span of the annealing temperatures. Two reasons are postulated for this discrepancy. First, the samples may not have been annealed long enough to fully equilibrate in the liquid state, resulting in smaller enthalpy differences than predicted. Second, it is also possible that the heat capacities of the liquid at temperatures below 620 K are overestimated. It is difficult to get heat capacity data in this regime due to the long relaxation times required. In addition, the enthalpy values of the glassy as-cast specimens another 250 J above those annealed at 643K. This demonstrates that the as-cast samples, which were rapidly quenched from above the liquidus temperatures, have the highest quenched in enthalpy of all of the glasses.

If we further examine Fig. 5.7, we can see the most significant effect of the annealing the glass actually occurs during the relaxation process around 800 K. It is clearly visible that this process happens at higher and higher temperatures as the glass is annealed at lower temperatures. It can also be seen that as this transition goes higher temperatures the glass moves further out of equilibrium with the liquid. In fact, for some annealed samples, as the glass relaxes to the liquid state, so much extra enthalpy is required that the power from the current pulse is unable to keep up and the sample begins cooling. In essence, it is exchanging energy stored mostly in the vibrational states of the glass with the configurational states of the liquid that just became available upon relaxation of the system. It should be noted that this is not representative of a negative heat capacity, but rather a system that has been driven far out of thermodynamic equilibrium returning to its equilibrium state. To quantify just how much enthalpy was necessary to relax the difference between the liquid

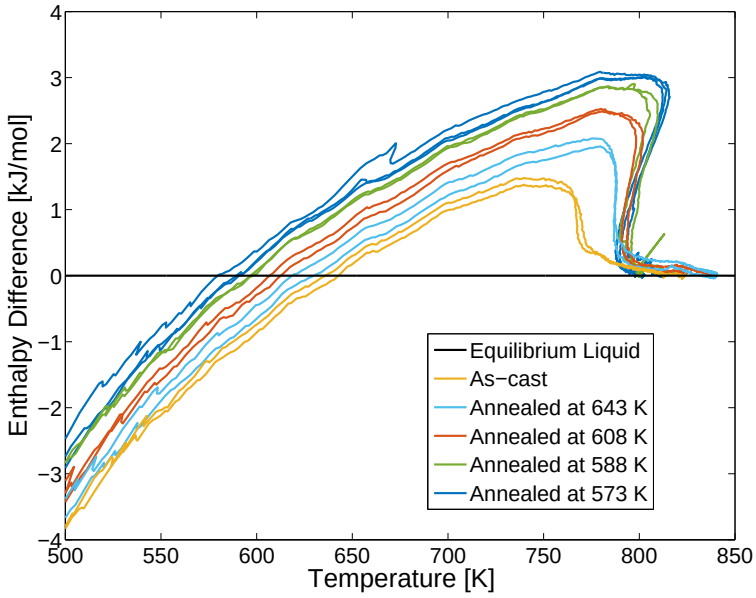

Figure 5.8: Enthalpy difference between equilibrium liquid and heating samples($H_l - \Delta H_{exp}$) vs. temperature. Positive values indicate the glass has to absorb energy to equilibrate with the liquid at that temperature, while negative values indicated the glass must release heat.

enthalpy function and the experimental enthalpy data was taken ($H_l - \Delta H_{exp}$) and plotted in Fig. 5.8.

It is evident from Fig. 5.8 the degree to which these glasses haven been driven out of equilibrium before relaxing. Samples annealed at 643 K had to recover 3 kJ/mol of enthalpy before relaxing to the liquid state. To put this quantity in perspective, the heat of fusion of $Zr_{41.2}Ti_{13.8}Cu_{12.5}Ni_{10}Be_{22.3}$, a very similar alloy, is roughly 8 kJ/mol. In Fig. 5.9, this enthalpy difference between the liquid and the glass is plotted versus time. It is evident that most of the enthalpy difference is relaxed in 1 ms. As a result, it would require an additional ∼3 MW/mol of specific power in order to heat through this relaxation event without the sample experiencing cooling.

Since the data taken in these experiments is enthalpy data and the heating rate in these experiments is not constant, it difficult to find an appropriate measure of the glass transition temperature. Typically glass transition temperatures are measured as either the onset, midpoint, or end of the jump from a glassy heat capacity to a liquid heat capacity at a constant heating rate in a scanning calorimeter. Due to the cooling upon relaxation of some samples in this experiment, this approach

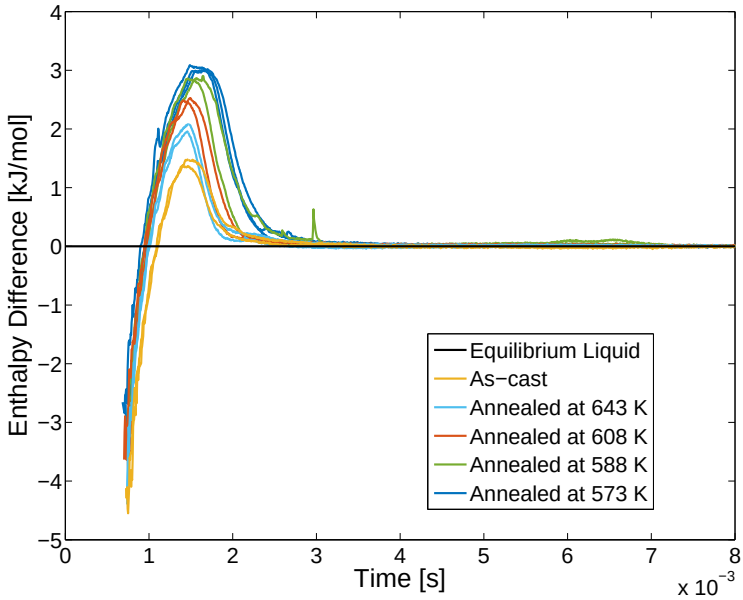

Figure 5.9: Enthalpy difference between equilibrium liquid and heating samples($H_l - \Delta H_{exp}$) vs. time. Positive values indicate the glass has to absorb energy to equilibrate with the liquid at that temperature, while negative values indicated the glass must release heat.

is impractical, as calculated heat capacities take on negative and infinite values during these cooling events. Another approach was necessary. Since the magnitude of $H_l - \Delta H_{exp}$ would continue to increase during heating if the samples did not relax and then decline during the glass transition, the peak of the smoothed $H_l - \Delta H_{exp}$ data vs time was used as a measure of the glass transition onset, and the temperature at this time was taken as T_g.

The calculated glass transition temperatures are plotted in Fig. 5.10 vs the annealing temperature of each sample. The glass transition for $Zr_{46.75}Ti_{8.25}Cu_{7.5}Ni_{10}Be_{27.5}$ is measured to be 622 K at heating rates 0.33 k/s. Here the glass transition temperatures are measured to be 745 K for the as cast samples, and between 765 and 795 K for the annealed samples. As the heating rate increases by 6 orders of magnitude, the allowed time for relaxation of the glass is reduced by 6 orders of magnitude. The Maxwell relaxation time of a material is η/G, where η is the viscosity and G is the shear modulus. Since the shear modulus of the glass doesn't vary strongly with temperature, changes in η account for the greatest changes in relaxation time. Therefore, the viscosity must be reduced 6 orders of magnitude before the sample can relax. Using the cooperative shear model fit

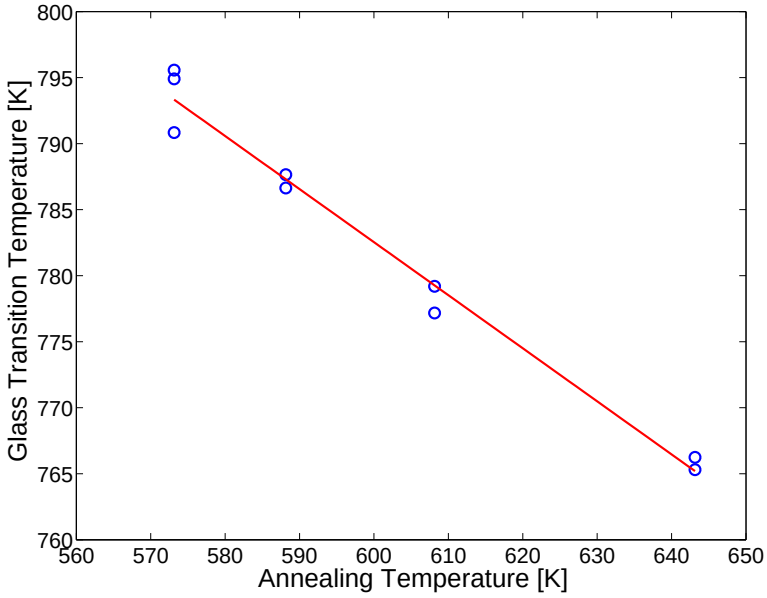

Figure 5.10: Glass transition temperature vs annealing temperature for $Zr_{46.75}Ti_{8.25}Cu_{7.5}Ni_{10}Be_{27.5}$ measured at heating rate of approximately 5×10^5 K/s. Red line is a linear fit to the data with a slope of -0.401

from Chapter 4, we find that $\eta(622K) \approx 3 \times 10^{10}$ Pa·s. The temperature where η is reduced 6 orders of magnitude to 3×10^4 Pa·s is found to be 779 K. Thus, it is possible to predict the change in glass transition temperature to around 40K accuracy for 6 orders of magnitude change in heating rate.

There appears to be a linear trend with a slope of -0.4 between the glass transition temperature and the annealing temperature. This slope may be explained by a potential energy landscape argument. If the glass is allowed to relax at lower and lower temperatures, it will fall deeper into the landscape. Relaxation of the glassy to liquid state is a thermally activated process associated with the system hopping over saddle points to jump from one minimum to the next. When the system is deeper in the landscape, higher activation energies are required to move between minima and there are are fewer minima available to jump to. Therefore, higher temperatures are required to achieve the same relaxation times accessible to other glasses higher in the landscape at lower temperatures. As a result, the annealing temperature has a negative correlation with the glass transition temperature. The surprising development is that this effect is so large. Typically in DSC scans with heating rates of 0.33 K/s the effect of annealing samples at different temperatures may

cause the glass transition temperature to vary by a few degrees, depending on how it is measured. At heating rates of 5×10^5 K/s, the effect of annealing samples is very pronounced in both the glass transition and the measured enthalpy differences from the glass.

5.5 Conclusion

Capacitive discharge is capable of heating bulk samples of metallic glasses at rates 10^5 or 10^6 K/s. This opens an entirely new realm of possibilities for processing metallic glasses thermoplastically. It is therefore valuable to understand the behavior of metallic glasses when heated using this method. This is especially true as there is no dynamic control of the discharge process, so predicting the behavior of the material before a processing step is preformed is a necessity. It is possible to outfit a capacitive discharge welder with relatively simple tools to turn it into a viable, highly sensitive calorimeter. With this technique it is possible to dynamically observe the enthalpy vs temperature relation for the heating of the materials. This information can be used to calculate accurate heat capacities for a glassy material. The glass transition is observed to occur at temperatures 123 K greater than is typical for laboratory experiments performed at heating rate of 0.33 K/s. This method is sensitive enough to be able to discern the enthalpy differences between samples annealed at different temperatures. Finally, at these rapid heating rates, the glass transition temperature is very sensitive to the thermal history of the glass, and shows a strong correlation with the annealing temperate.

Chapter 6

Conclusion and Future Work

6.1 Conclusion

Because supercooled metallic liquids are susceptible to rapid crystallization, investigation of their behavior has been severely limited. Typically, metallic liquids are studied in two temperature ranges. The first temperature range is at or above the melting point of the alloy, where liquids remain thermodynamically stable indefinitely, while the second is at or below the glass transition temperature, where crystallization is kinetically limited to long timescales. The span of temperatures between these two ranges is the location of the crystallization "nose", i.e. the temperature at which crystallization occurs the most rapidly. In the best case scenario, a metallic alloy has seconds at the nose temperature before crystallizing. Realistically, this window is only fractions of a second, making the study of the supercooled liquid that exists for short time periods at temperatures around the nose a significant challenge. A large portion of this challenge is the technical hurdle of uniformly heating a macroscopic sample ($>$ 1 mm minimum dimension) of metallic glass to a stable temperature very rapidly. Here the use of capacitive discharge to ohmically heat metallic glasses at rates of 10^5 to 10^6 K/s has been presented as one that grants access to the short-lived metallic liquids, which have been largely unstudied.

To expand our understanding of these liquids, several experimental methods have been explored. First, pulse calorimetry was demonstrated to be a sensitive and reliable method for studying the glass transition of an amorphous sample during rapid heating and well as finding the enthalpy versus

temperature relations of both the glassy and liquid states of said sample. Second, a method combining parallel plate rheometry and capacitive discharge was developed to measure the viscosities of metallic liquids approaching the crystallization nose. Viscosities as low as 10^3 Pa·s were measured using this method. Finally, by using capacitive discharge heating and then waiting for the temperature increase associated with the crystallization, it was possible to determine the time until the onset of crystallization at a specific temperature. This allowed the mapping of the crystallization kinetics of a metallic glass around the crystallization nose.

To explore the possibility of using this method as a manufacturing process for metallic glass parts, several forming methods were investigated. First, a method to injection mold metallic glass parts was successfully put into practice. Second, a method to stamp metallic glass parts was also successfully applied. Finally, a new technique using the combination of the heating current and a magnetic field to produce a forming force was also used to produce glassy parts.

The application of the capacitive discharge heating to metallic glasses has enabled access to a significant range of temperatures, which were previously inaccessible because of the rapid intervention of crystallization. This method provides a platform for both scientific experimentation as well as manufacturing using supercooled metallic liquids.

6.2 Future Work

In order to produce a metallic glass, a molten alloy must be cooled rapidly enough to prevent any crystallization from taking place. The critical temperature range for this cooling process is around the crystallization nose, where the time required to nucleate crystals is the shortest. Therefore, the formation of metallic glasses is dominated by the crystallization kinetics of metallic liquids at the crystallization nose. Currently, there has been limited exploration of metallic liquids in the temperatures around their crystallization noses. Capacitive discharge heating is currently the only method with which it is possible to access metallic liquids around their crystallization nose temperature. This opens the possibility for gaining greater insight into the process of glass formation in metals by high speed experiments performed on the liquids near the nose. While the experimental

methods detailed here allow for calorimetric and rheological investigation of the liquids, there is still much to be desired for available experimental techniques. For example, adapting the process to new flow geometries would enable the measurement of even lower viscosities at higher temperatures. This could close the gap in high temperature and low temperature viscosity data for some alloys. It would also be possible to measure elastic properties of the liquids using ultrasonic transmission. However, any technique would have to be modified to be done on very short time scales and be robust enough to handle the electrical disturbances associated with large current pulses.

Even more interesting would be the chance to observe the crystallization process as it occurs. The ability to measure time-temperature transformation data has been demonstrated, and pursuing this for a variety of alloys would help paint a clearer picture of the crystallization kinetics of metallic glasses. In addition, combining this with a stamping process to rapidly cool the materials after or during crystallization, it may be possible to freeze in short lived phases or microstructures for later investigation. The combination of liquid properties around the nose and data gathered on the kinetics of crystallization would have clear benefits in testing and refining current theories of glass formation in metal alloys.

Appendix A

Chapter 1 Appendix

A.1 Materials and Methods

Uniform and fully amorphous cylinders with diameters of 4 mm and 5 mm and lengths of 2-5 cm were fabricated from the glass-forming alloys $Zr_{41.2}Ti_{13.8}Cu_{12.5}Ni_{10}Be_{22.3}$ (Vitreloy 1) and $Pd_{43}Cu_27Ni_{10}P_{20}$ by casting in copper molds or water quenching in quartz tubes. The cylinders were cut into 2-3 cm lengths (total volume 0.25-0.4 cm^3) with flat, polished, parallel ends. Cylinders are placed between parallel faced Cu electrodes loaded under compression by a pneumatic cylinder with a force up to 400 N (Fig. 1.3a). This load was found to ensure good electrical contact between the copper electrode and metallic glass rod. A schematic of the setup is shown in Fig. A.1. To study heating and temperature uniformity of the rods, a calibrated high speed infrared imaging camera (FLIR Corp., SCR4000) was employed at a frame rate of 1333 frames/s. High speed video imaging (Casio EX-FH20 camera) at 1000 frames/s was used to complement the infrared thermal imaging to analyze the dynamic deformation of the metallic glass rods under compressive loading at various temperatures. An IMPAC IGA740-LO high-speed infrared pyrometer was also used to generate temperature-time curves with high time resolution (as in Fig. 1.3b in the main article). The pyrometer has a response time of 5 microseconds. We measured temperature vs. time over a circular focal spot of 1 mm diameter near the rod center.

The rod is deformed between two parallel and polished ceramic disks (Macor^{TM}) having very low thermal conductivity ($\sim 3 W/m \cdot K$). The low thermal conductivity of the plates minimizes

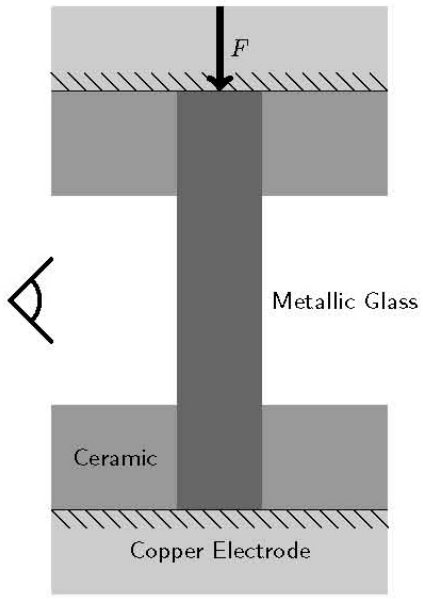

Figure A.1: Schematic of the Ohmic heating setup used to conduct enthalpy and viscosity measurements.

conductive heat loss from the sample during deformation and enhances the adiabatic constraint. The "injection molding" apparatus is based on the set-up described above (Fig. A.1) combined with an electrically insulating "barrel" to confine and inject the metallic glass rod, a simple gating system, and several simple mold-tools (see Fig. 1.4a in the main article). The set-up comprises an upper copper electrode used as plunger, a lower copper electrode served as base, and a quartz sleeve used as insulating barrel liner to electrically insulate and confine the sample.

A.2 Electrical resistivity measurement of the Vitreloy 1 glass

The temperature dependence of the electrical resistivity $\rho_e(T)$ of the Vitreloy 1 glass was measured using the four-probe method during continuous heating of a glassy rod. A room temperature value of 191 μcm was measured, with an average temperature coefficient of $S = (1/\rho_e)(d\rho_e/dT) = -12 \times 10^{-5}\mathrm{K}^{-1}$ measured between room temperature and the glass-transition temperature. The resistance R_s of Vitreloy-1 rods used in this work with diameters of 4 mm and lengths of about 2 cm averaged

over a range between room temperature and halfway between T_g and T_m is therefore 3 mΩ.

A.3 Characterization of the RLC circuit

The capacitor-discharge system is an RLC circuit. A schematic is presented in Fig. A.2. The intrinsic resistance of the circuit, R_0, comprises the resistance of the Silicon Control Rectifier, the copper leads, the electrodes, and the capacitor bank itself. A small inherent inductance L exists arising from the copper leads and the geometry of current carrying loop. The circuit capacitance C is known to be 0.264 F. In order to get an accurate measure of R_0 and L, a Rogowski Coil was wound around a current carrying lead. The time-dependent signal obtained from the coil during discharge was integrated to determine the functional form of the time-dependent current in the loop. After discharging the circuit several times in the absence of a sample, the circuit current was then fitted to the under-damped solution for the transient response of an RLC circuit to obtain values for R_0 and L using the known C. An average R_0 of 2.85 ± 0.1 mΩ and an average L of 2.4 ± 0.1 μH are obtained, while the damping factor ζ is found to be ~ 0.5 for the shorted circuit with no sample charge. The shorted RLC circuit is thus under-damped. When the metallic glass sample rod is included in the discharge circuit, ζ is found to be ~ 1.0, indicating a very near critically-damped RLC circuit. The transient response of a critically damped system permits transfer of energy from the capacitor to the sample in the shortest possible time without current overshoot/ringing and is therefore the preferred configuration for rapid and efficient energy dissipation. For critical damping, the current pulse takes the form $I(t) = Kt\exp(-t/2\tau_h)$, where $\tau_h = L/R$ and K is a normalization constant. With $L \approx 2.4\mu H$ and $R = R_s + R_0 \approx 6$ mΩ one can obtain $\tau_h \approx 0.4$ ms. The power delivered to the sample becomes $P(t) = R_s K^2 t^2 exp(-t/\tau_h)$ and the sample heating rate is $dT/dt = P(t)/c_P$, with c_P the total heat capacity of the sample. Integrating this equation (and ignoring the temperature dependence of c_P) gives the predicted $T(t)$ curve for the metallic glass rod heated by the discharge. One obtains:

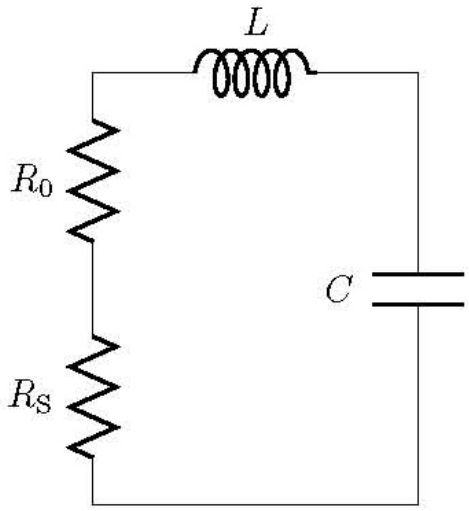

Figure A.2: Schematic of the RLC circuit corresponding to the Ohmic heating setup.

$$T(t) - T_0 = \frac{R_s K^2}{c_P} \int_0^t \exp\left(-\frac{t}{\tau_h}\right) dt = \frac{\varepsilon C V^2}{2 c_P} \left\{1 - \exp\left(-\frac{t}{\tau_h}\right) \left[1 + \frac{t}{\tau_h}\left(1 + \frac{t}{2\tau_h}\right)\right]\right\},$$

where the normalization constant K was adjusted to give the total heat dissipation in the sample as $t \to \infty$ of $E = (\varepsilon/2)CV^2$ (see Section 3 below). This functional form was used to fit the heating response to independently estimate $\tau_h = L/R$. A value of $\tau_h \approx 0.33$ ms is determined (Fig. 1.3b in the main article). The independent estimate of L/R provides a self-consistency check on the overall description of the RLC circuit.

A metallic glass rod with a current density, J, flowing through a uniform cross section will heat uniformly at an average rate of $dT/dt = \rho_e J^2/c_P$ where ρ_e is the resistivity, J is in A/m^2, and c_P is the specific heat per unit volume. Taking $J \sim 10^9$ A/m^2, as is typical in the present experiments, and using a specific heat of $c_P \approx 4 \times 10^6$ J/m^3·K and electrical resistivity of $\rho_e \approx 191$ $\mu\Omega$·cm for the Vitreloy 1 glass, one obtains a typical heating rate of $\sim 4 \times 10^5$ K/s. The capacitor stores total energy $E_C = (1/2)CV_0^2$, where $C = 0.264$ F for the present experiments, and the applied Voltage V_0

ranges up to 200 V. The total load resistance is $R = R_0 + R_s$ where $R_0 = 2.85\text{m}\Omega$ is the measured output resistance of the capacitor system (see section above) and the sample resistance is $R_s \approx 3\text{m}\Omega$ for the metallic glass rods used in these experiments. The fraction of the discharged energy delivered to the sample is $\varepsilon = R_s/(R_0 + R_s)$ = efficiency of the system. Total Ohmic heat dissipation in the sample is $E = (\varepsilon/2)CV^2$.

A.4 Uniform heating Requirements

To dissipate heat uniformly in the sample requires that the following conditions be met: (1) a sample of highly uniform cross section; (2) a small value $S = (1/\rho_e)d\rho_e/dT$ along with no discontinuous jump in resistivity associated with melting (always achieved in metallic glasses since electrical resistivity is continuous through the glass transition); and (3) a dynamic electric field and associated current density during the discharge which penetrate the sample uniformly.

Requirement (1) is a straightforward constraint on the sample quality and geometry. To better quantify requirement (2), consider a long one-dimensional rod with axis lying in the longitudinal z-direction subjected to a constant and uniform current density J, and having an initial temperature profile $T(z, t = 0) = T(z, 0) = T_0 + (\Delta T)_0 \sin(Kz)$ where $T_{av}(t) = T_0 + \rho_e J^2 t/c_P$ is the average rod temperature (at time t) and $(\Delta T)_0$ the initial amplitude of a periodic temperature inhomogeneity of wavelength L and wavevector $K = 2\pi/L$. For an initial temperature variation in the transverse direction (x or y direction), the coordinate z in the above expression can be replaced by x (or y). At $t = 0$, the rod is Ohmically heated with a z-dependent (x-dependent for transverse temperature variation) heating rate since $\rho_e(T) = \rho_e(T0) + S\rho_e(T_0)(T(z, 0) - T_0) + \ldots$ and subject to Fourier heat conduction. A heating rate stability analysis for the z-direction gives:

$$dT(z,t)/dt|_{t=0} = \rho_e J^2/c_P \left[1 + S(\Delta T)_0 \sin(Kz) + \text{higher order terms in}(\Delta T)_0 - D_T \nabla^2 T(z,0)\right],$$

where D_T is the thermal diffusivity. To linear order, this gives a relative longitudinal inhomogeneity

in the heating rate:

$$\left[d(\Delta T)/dt\right]/\rho_e J^2/c_P = S(\Delta T)_0\left[1 - 4\pi^2 c_P D_T/(SL^2J^2\rho e)\right],$$

where $dT_{av}/dt = \rho_e J^2/c_P$. Since initial temperature variations in the transverse x-direction produce current variations $J(x) = (E/\rho_e)/(1 + S\Delta T) = (E/\rho_e)(1 - S\Delta T + \dots)$ where E is the constant applied E-field in the z-direction, it is easily shown to linear order the stability equation for transverse heating rate variations becomes:

$$\left[d(\Delta T)/dt\right]/\rho_e J^2/c_P = S(\Delta T)_0[-1 - 4\pi^2 c_P D_T/(SL^2J^2\rho_e)\right].$$

Both equations have a simple exponential solution for $\Delta T(t)$:

$$\Delta T(t) = (\Delta T)_0 \exp(\alpha t) = (\Delta T)_0\left[1 + \alpha t + \dots\right],$$

where $\alpha = S\left[\rho_e J^2/c_P\right]\left[\pm 1 - 4\pi^2 c_P D_T/(SL^2J^2\rho_e)\right]$ where the "+" sign refers to the z-direction and the "−" sign to the transverse x-direction. If the right-hand bracket $A = [1-4\pi^2 c_P D_T/(SL^2J^2\rho_e)] > 0$, the inhomogeneity grows along the z-direction when $S > 0$ with an amplification coefficient α proportional to S, to the average heating rate $\rho_e J^2/c_P$, and to A. If $4\pi^2 c_P D_T/(SL^2J^2\rho_e) < 1$, or equivalently if $L < L_{crit} = 4\pi^2 c_P D_T/(SJ^2\rho_e)$, then $A < 0$ and the inhomogeneity of length scale $L < L_{crit}$ along the z-axis will decay and the rod will be dynamically "stable" at short wavelengths against growth of inhomogeneous heating in the z-direction. For Vitreloy 1, $c_P \approx 4 \times 10^6$ J/m^3, $c_P D_T = \kappa =$ thermal conductivity ≈ 8 W/m·K, $S = 12\times10^{-5}$ K^{-1}, and $\rho_e = .1.91\times10^{-6}\Omega$·m. Using $J \sim 1\times10^9$ A/m (typical for the present experiments and heating rates of $10^5 - 10^6$ K/s), one obtains $L_{crit} \sim 0.5$ mm along the z-direction. One sees that relaxation of temperature inhomogeneities by Fourier heat conduction is effective only for relatively small $L < 0.5$ mm. Consider a large scale longitudinal inhomogeneity such as that produced by electrode/metallic glass contact resistance at two ends (located at $z = \pm L/2$) of a rod with $L \approx 2 - 3$ cm, Fourier heat conduction is ineffective,

and one has $A \approx 1$, and $\alpha \approx S[\rho_e J^2/c_P]$, so that:

$$\Delta T(t) = (\Delta T)_0 \exp(\alpha t) = (\Delta T)_0[1 + \alpha t + \dots] = (\Delta T)0 + S(\Delta T)_0[\rho_e J^2/c_P]t + \dots$$

The growth of $\Delta T(t)$ is directly proportional to $S(\Delta T)_0$. For S negative, the longitudinal inhomogeneity will always decay. By contrast, a transverse inhomogeneity with $L \sim 1$ cm, and $S < 0$, will grow in proportion to S. Generally, one sees that if $|S| \leq 10^{-4}\mathrm{K}^{-1}$ as is appropriate for metallic glasses, and for modest $(\Delta T)_0 \sim 10^2$ K, neither longitudinal nor transverse inhomogeneities grow appreciably. In contrast, for a crystalline material with $S \sim 10^{-2}\mathrm{K}^{-1}$, all inhomogeneities will grow far more rapidly. Melting of the crystalline metal at the contact will lead to even greater instability. The small values of S in metallic glasses are thus key to suppressing the development of localized heating instabilities and thereby to achieving uniform heating of bulk samples.

Requirement (3) is met when the dynamic electromagnetic skin depth at frequency ω, $\Lambda = (2\rho_e/\mu_0\omega)^{1/2}$, is much greater than the sample dimension normal to the applied electric field where μ_0 is permittivity of free space. For $\omega \sim 1/\tau_h \sim (R/L)^{-1} \sim 10^3$ Hz (as used in the present work), and $\rho_e \sim 2 \times 10^{-6}\Omega$·m typical of a metallic glass sample, we obtain $\Lambda \sim 2$ cm. Condition (3) is well satisfied since the radius of the cylindrical samples is roughly an order of magnitude less than 2 cm. A detailed analysis by Lohoefer and Pottlacher [32] of the skin depth effect for a long square metal wire of half thickness "a", heated by a suddenly switched-on capacitive discharge gives a relative inhomogeneity in the E-field at elapsed time t (from the onset of a sudden discharge) over the sample cross section of $|\Delta E/E| < 0.39a^2\mu 0/(\rho_e t)$. For an amorphous wire of $a = 2$mm, at $t = 0.1\mathrm{ms} < \tau_h$, we obtain $|\Delta E/E| = 0.01$. At $t = 0.4$ ms $\approx \tau_h$, one has$|\Delta E/E| = 0.0025$. Heating inhomogeneity due to skin depth effects is expected to be of order 1% or less over the overwhelming majority of the energy discharge. In summary, requirement (3) above should be well satisfied under the experimental conditions used in the present studies.

A.5 Analysis of Enthalpy Data

Figure 3c of the main article summarizes relevant data on specific energy density dissipated in the rod (normalized by the total rod mass), and average sample temperature achieved in the heating stage, T_F, for several experiments. The specific energy density, $e = (\varepsilon/2m)CV^2$ (m is sample mass and e is in J/g) dissipated in the rod is the total energy stored in the capacitor corrected by an efficiency factor, $\varepsilon = R_s/(R_s + R_0)$, which accounts for the total output resistance of the discharge circuit (primarily from the copper leads), $R_0 \approx 2.85\text{m}\Omega$ (see Section 2 above), and the resistance of the present sample rod, $R_s = 2.66\text{m}\Omega$, determined from the temperature dependent sample resistivity and measured sample rod dimensions (see Section 2 above). This gives an efficiency $\varepsilon = 0.483$ and energy coupled to the sample of 505 J (where the total output energy is $\frac{1}{2}CV^2 = 1046$ J). Using the sample mass of 1.59 g, the specific energy density is $e(T_F) = 318$ J/g. The average final temperature, $T_F = 799$ K, is taken from thermal imaging. Multiplying $e(T_F)$ by the average atomic weight of the alloy of 60.3 g/mole gives a specific enthalpy per mole of $h(T_F) = 19.2$ kJ/mole, dissipated in the material to reach T_F. The $h(T_F)$ data similarly collected for a large number of experiments are plotted in Fig. 1.3c to obtain the $h(T)$ curve for Vitreloy 1 over a broad range in the undercooled liquid region that has been previously inaccessible.

A.6 Analysis of Viscosity Data

The dynamic deformation of a cylinder under uniaxial compressive stress σ between two parallel plates is well described in the limiting cases of small strains and very large strains. For small strains, homogeneous compression at strain rate $\gamma = y^{-1}(dy/dt)$ gives a viscosity [35]:

$$\eta = \frac{\sigma}{2\gamma} = \frac{Fy^2}{3v_0(dy/dt)} \tag{A.1}$$

with v_o the total sample volume, F the applied force, and y the sample height. For large strains where the cylinder spreads into a thin disk with a no-slip boundary with the plates, the viscosity is

given by the Stefan equation [79]:

$$\eta = \frac{\pi F y^5}{24 v_0^2 (dy/dt)}. \tag{A.2}$$

Both limits are relevant to an analysis of the present experiments. A simple model of an apparatus based on capacitor discharge heating is also required. The electrode/drive system consists of a pneumatic cylinder which applies a known force F_0 to the electrode assembly. The drive cylinder uses stainless steel shaft to drive the copper electrode assembly. The electrode assembly includes a thick copper plate which slides freely on Teflon guide rods and makes contact with the cylindrical charge. The piston/electrode assembly has a total measured mass $m = 1.15$ Kg. Under the applied force, this assembly accelerates at a rate $a_0 = (F_0/m) + g$ (g is gravitational acceleration) in the absence of viscous forces created by the compression of the sample. During sample deformation, the electrode assembly is also acted on by an upward viscous force F_V from the sample. The electrode assembly acts as a "momentum exchanger" with total acceleration $a(t) = (F_0 - F_V)/m + g$. Typically, $F_0/m \sim 300 - 400\text{m/s}^2 \gg g \approx 10\text{m/s}^2$ so that gravitational effects are small. Frictional forces in the drive system are also very small (typically less than mg) and are neglected here. One measures the height of the sample vs. time, $y(t)$, using a frame by frame analysis of video images. The initial height of the sample is y_0. The digitized $y(t)$ data are fit to an analytic functional form which is differentiated to obtain the piston velocity $v(t) = dy(t)/dt$, and acceleration $a(t) = dv(t)/dt$. The viscous force due to flow of the sample is then given by:

$$F_V(t) = ma(t) - F_0 - mg.$$

For example, when $a(t) = 0$ (at the inflection point of the $y(t)$ curve), $F_V(t)$ is equal to the applied downward force $F_0 + mg$. Using $y(t)$ and $v(t)$, and $F_V(t)$ one can compute the viscosity, η from Eq. (A.1) or Eq. (A.2) as appropriate. Equation (A.1) applies during the early stages of deformation when $y_0 > y(t) > 0.5y_0$ (case 1) while Stefan's equation, Eq. (A.2), applies when $y(t) \ll y_0$ (case 2). Owing to the limited spatial resolution of the video images and geometry of the present experiments, it was difficult to carry out accurate image analysis of late stages of deformation where the sample

thickness is small and the Stefan equation applies. Furthermore, the adiabatic assumption of a uniform sample temperature breaks down as the sample thins, and heat is lost by conduction to the parallel plates. To mitigate the breakdown of the adiabatic constraint, viscosity measurements were carried out using a modified geometry in which two circular ceramic disks 4 mm in thickness with polished surfaces were attached to the face of each circular copper electrodes, as shown in Fig. 1.3a of the article. A cylindrical hole of diameter 4 mm was machined in the center of each ceramic disk. The metallic glass rods were slip fit into the holes so as to make contact with the copper electrodes (see Fig. 1.3a in the main article). On heating and deformation, the rod ends are confined in the ceramic, and the remaining rod section deforms under load between the flat parallel ceramic disks. Teflon "guide rods" were used to align and guide the copper/ceramic electrode assembly and ensure that the plates close smoothly and remain parallel during closing. Despite these modifications, it was still difficult to obtain accurate viscosity data in the "Stefan" limit in the present set-up. The data presented in Fig. 1.3d of the article are thus limited to viscosities greater than 10^4 Pa·s or higher.

Appendix B

Chapter 3 Appendix

B.1 Analysis of ohmic heating in a magnetic field

The electrical energy E dissipated to ohmically heat a prismatic metallic glass sample having length l along the direction of current flow, width w, and thickness t from an initial temperature T_o (typically room temperature) to a process temperature T in the supercooled liquid region (i.e. above the glass transition temperature T_g) where the viscosity is on the order of 10^2 Pa·s is given by:

$$E = wlt \int_{T_o}^{T} c_p dT, \tag{B.1}$$

where c_p is the specific heat capacity of the material in J/m^3·K. Assuming that c_p of the glass and the supercooled liquid are constant (i.e. independent of temperature) and approximately equal, and neglecting the specific enthalpy recovered at T_g which is generally small, Eq. (B.1) can be approximated as:

$$E = c_p wlt \Delta T, \tag{B.2}$$

where ΔT is the temperature rise from T_o to T. For most metallic glasses,

$$\Delta T = 1.5 \Delta T_g, \tag{B.3}$$

where $\Delta T_g = T_g - T_o$ [70]. If one approximates the time-dependence of a current pulse produced in an electrical discharge with a characteristic discharge time τ by an equilateral triangle, the electrical energy dissipated during the discharge can be estimated as:

$$E \approx I^2 R\tau, \tag{B.4}$$

where I is the maximum current attained at time τ, and R is the electrical resistance of the metallic glass sample, given by:

$$R = \rho lwt, \tag{B.5}$$

where ρ is the electrical resistivity of the metallic glass. Substituting Eqs. (B.3)-(B.5) into (B.2) and solving for I, one can obtain the electrical current required to ohmically heat a metallic glass sample a temperature where the viscosity is on the order of 10^2 Pa·s as follows:

$$I \approx Cwt\tau^{-1/2}. \tag{B.6}$$

The constant C has units of $\mathrm{A{\cdot}s^{1/2}/m^2}$, and involves the material properties as follows:

$$C \approx \sqrt{((1.5c_p\Delta T_g)/\rho)}. \tag{B.7}$$

Below we estimate the constant C for a wide variety of metallic glass compositions. The temperature-dependent resistivity of metallic glasses is known to vary over a narrow range, typically from 150-200 $\mu\Omega$·cm [59]. Here, for the sake of simplicity, we assume that the resistivity of all metallic glasses is represented by a mean value of 175 $\mu\Omega$·cm (1.75×10^{-6} Ω·m). Moreover, the specific heat capacity of the glass at room temperature will be assumed for c_p. The specific heat capacity in $\mathrm{J/m^3{\cdot}K}$, as used in Eqs. (B.1) and (B.7), can vary substantially between metallic glass compositions because of the variation in the molar volume between compositions. Here we estimate the specific heat capacity in $\mathrm{J/m^3{\cdot}K}$ for each metallic glass composition as the ratio between 35 J/mol·K and its molar volume. Lastly, ΔT_g, estimated here as $\Delta T_g = T_g - 298\mathrm{K}$, also varies considerably between metallic glass

compositions.

In Table I we present values for ΔT_g, molar volume v_m, and c_p in J/m^3·K (estimated as the ratio between 35 J/mol·K and v_m) for a Au-based, Pt-based, Pd-based, Zr-based, and Fe-based metallic glass to estimate the constant C corresponding to each composition using Eq. (B.7). As seen, C for these broadly varying metallic glass compositions is in the range of $\sim 2 \times 10^7$ to 4×10^7 A·s$^{1/2}$/m^2.

Table B.1: Data for five metallic glass compositions for estimating constant C using Eq. (B.7).

Metallic Glass Composition	ΔT_g [K]	v_m [m^3/mol]	c_p [J/m^3·K]	C [A·s$^{1/2}$/m^2]	Refs.
$Au_{49}Cu_{26.9}Ag_{5.5}Pd_{2.3}Si_{16.3}$	103	9.23×10^{-6}	3.79×10^6	1.83×10^7	[80]
$Pt_{57.5}Cu_{14.7}Ni_{5.3}P_{22.5}$	210	8.75×10^{-6}	4.00×10^6	2.68×10^7	[81, 82]
$Pd_{40}Ni_{10}Cu_{30}P_{20}$	295	7.92×10^{-6}	4.42×10^6	3.34×10^7	[83]
$Zr_{41.2}Ti_{13.8}Cu_{12.5}Ni_{10}Be_{22.5}$	320	9.95×10^{-6}	3.52×10^6	3.11×10^7	[83]
$Fe_{70}Ni_5Mo_5C_5B_{2.5}P_{12.5}$	398	6.89×10^{-6}	5.08×10^6	4.16×10^7	[84]

Appendix C

Chapter 4 Appendix

C.1 Parallel Plate Squeeze Flow with Perfect Slip Boundary Conditions

The parallel plate squeeze flow geometry is shown in Fig. C.1 for a cylindrical coordinate system(using r, ϕ, and z). It consists of a cylinder being squeezed along the axial direction by two plates. If gravity is ignored it is possible to reduce to problem to only the top half of the cylinder being compressed, so $z = 0$ is chosen to be at the center of the rod to simplify the problem. In order to solve the for the flow, the following assumptions were made:

1. The sample behaves as a incompressible newtonian fluid.
2. Creeping flow. ($Re < 1$) Inertial terms in equations of motion can be ignored. It should be noted that this implies instantaneity (the flow can solved completely at any instant in time knowing only the boundary conditions).
3. Flow is axisymmetric. (There is no dependence on ϕ and $v_\phi = 0$)
4. The effects of gravity can be ignored.
5. v_z is not a function of r.

The following boundary conditions are used to constrain the solution to best reflect the constraints on the sample:

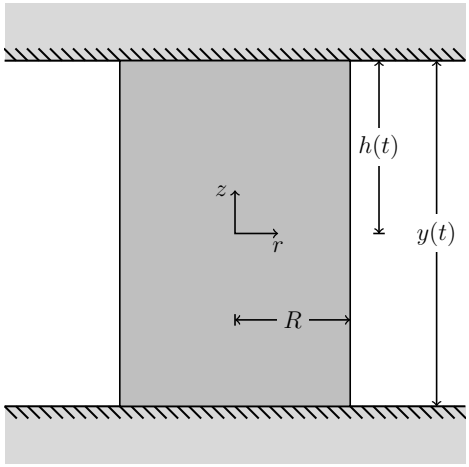

Figure C.1: Schematic cross-section of parallel plate squeeze flow. A cylindrical sample is compressed between two flat plates.

1. $v_z(z = 0) = 0$ (Symmetry)

2. $v_z(z = h) = \dot{h}$ (Wall Velocity)

3. $\tau_{rz}(z = 0) = 0$ (Symmetry)

4. $\tau_{rz}(r = 0) = 0$ (Symmetry)

5. $v_r(r = 0) = 0$ (Symmetry)

6. $\tau_{rz}(z = h) = 0$ (Perfect-slip)

7. $\sigma_{rr}(r = R) = 0$ (Assuming ambient pressure = 0)

Here v denotes velocity, τ denotes the shear stress, and σ denotes the total stress. Using the newtonian viscosity law to express the shear stress τ_{rz}, we get

$$\tau_{rz} = -\eta \left[\frac{\partial v_r}{\partial z} - \frac{\partial v_z}{r} \right]. \tag{C.1}$$

Using assumption 5 this simplifies further to

$$\tau_{rz} = -\eta \frac{\partial v_r}{\partial z}.$$

Therefore, boundary conditions 3, 4, and 6 imply $\frac{\partial v_r}{\partial z} = 0$ at $z = 0, h$ and $r = 0$. Moving on to the continuity equation for incompressible flow we have:

$$\nabla \cdot \vec{v} = \frac{1}{r}\frac{\partial}{\partial r}(r v_r) + \frac{1}{r}\frac{\partial v_\phi}{\partial \phi} + \frac{\partial v_z}{\partial z} = 0 \tag{C.2}$$

$$\frac{\partial}{\partial r}(r v_r) = -r\frac{\partial v_z}{\partial z}.$$

If we use assumption 5 then we can set $v_z = f(z,t)$ and integrate the previous expression, we get

$$\frac{\partial}{\partial r}(r v_r) = -r\frac{\partial f}{\partial z}$$

$$r v_r = -\frac{r^2}{2}\frac{\partial f}{\partial z} + C(z).$$

Using boundary condition 5 we find $C(z) = 0$ and the following relation between v_r and f.

$$v_r = -\frac{r}{2}\frac{\partial f}{\partial z}. \tag{C.3}$$

If we apply assumptions 1 - 4 to the equations of motion, we get the following equations:

$$r: \qquad 0 = -\frac{\partial p}{\partial r} + \eta\left[\frac{\partial}{\partial r}\left(\frac{1}{r}\frac{\partial}{\partial r}(r v_r)\right) + \frac{\partial^2 v_r}{\partial z^2}\right] \tag{C.4}$$

$$z: \qquad 0 = -\frac{\partial p}{\partial z} + \eta\left[\frac{1}{r}\frac{\partial}{\partial r}\left(r\frac{\partial v_z}{\partial r}\right) + \frac{\partial^2 v_z}{\partial z^2}\right]. \tag{C.5}$$

Using assumption 5 and Eq. C.3 we can further simplify the equations to

$$r: \qquad \frac{\partial p}{\partial r} = -\frac{\eta r}{2}\frac{\partial^3 f}{\partial z^3} \tag{C.6}$$

$$z: \qquad \frac{\partial p}{\partial z} = \eta\frac{\partial^2 f}{\partial z^2}. \tag{C.7}$$

Since p has to be a state function of both r and z, we know

$$\frac{\partial^2 p}{\partial z \partial r} = \frac{\partial^2 p}{\partial r \partial z}. \tag{C.8}$$

Putting together Eqs. C.6 - C.8 we get

$$-\frac{\eta r}{2}\frac{\partial^4 f}{\partial z^4} = 0$$
$$\frac{\partial^4 f}{\partial z^4} = 0. \tag{C.9}$$

Integrating Eq. C.9 4 times we get the form of $f(z,t)$

$$f(z,t) = c_3(t)z^3 + c_2(t)z^2 + c_1(t)z + c_0(t). \tag{C.10}$$

Now we can use our boundary conditions to determine c_3, c_2, c_1, and c_0.

$$\text{B. C. 1} \quad \Longrightarrow \quad c_0(t) = 0$$
$$\text{B. C. 3} \quad \Longrightarrow \quad c_2(t) = 0$$
$$\text{B. C. 6} \quad \Longrightarrow \quad c_3(t) = 0$$
$$\text{B. C. 2} \quad \Longrightarrow \quad c_1(t) = \frac{\dot{h}(t)}{h(t)}.$$

Therefore, $f(z,t) = \dot{h}z/h$ and the velocity field in the sample is

$$v_z = \frac{\dot{h}z}{h}$$
$$v_r = -\frac{\dot{h}r}{2h}$$
$$v_\phi = 0.$$

If we plug our velocities back into the equations of motion we find that

$$\frac{\partial p}{\partial r} = 0,$$
$$\frac{\partial p}{\partial z} = 0$$

meaning pressure in constant throughout the liquid. Using the last boundary condition we can find the pressure of the fluid.

$$\sigma_{rr} = p + \tau_{rr}(R) = 0 \qquad \Longrightarrow \qquad p = -\tau_{rr}(R).$$

Simplifying the newtonian viscosity law for an incompressible fluid to find τ_{rr}, we get

$$\tau_{rr} = -\eta \left[2\frac{\partial v_r}{\partial r} \right] = \frac{\eta \dot{h}}{h}.$$

Finally, to find the total stress in the z direction, σ_{zz}, we use

$$\sigma_{zz} = p + \tau_{zz} = \tau_{zz} - \tau_{rr}.$$

Using the newtonian viscosity law a final time we get

$$\tau_{zz} = -\eta \left[2\frac{\partial v_z}{\partial z} \right] = -\frac{2\eta \dot{h}}{h},$$

and

$$\sigma_{zz} = -\frac{3\eta \dot{h}}{h}. \tag{C.11}$$

Solving for viscosity gives

$$\eta = -\frac{\sigma_{zz} h}{3\dot{h}}. \tag{C.12}$$

Plugging in $\sigma_{zz} = F/A$, $y = 2h$, $\dot{y} = 2\dot{h}$ to Eq. C.11, we find

$$\eta = -\frac{Fy}{3A\dot{y}}.$$

Assuming the sample volume remains constant, $A = v_0/y$ where v_0 is the initial volume of the sample. Using this we find

$$\eta = -\frac{Fy^2}{3v_0\dot{y}}. \tag{C.13}$$

Bibliography

[1] W L Johnson, Georg Kaltenboeck, Marios Demetriou, Joseph P Schramm, X Liu, Konrad Samwer, C P Kim, and Douglas C Hofmann. Beating Crystallization in Glass-Forming Metals by Millisecond Heating and Processing. *Science*, 332(6031):828–833, May 2011.

[2] Georg Kaltenboeck, Thomas Harris, Kerry Sun, Thomas Tran, Gregory Chang, Joseph P Schramm, Marios Demetriou, and W L Johnson. Accessing thermoplastic processing windows in metallic glasses using rapid capacitive discharge. *Sci Rep*, 4, October 2014.

[3] Georg Kaltenboeck, Marios D. Demetriou, Scott Roberts, and Johnson. Shaping metallic glasses by electromagnetic pulsing. *Nature Communications*, 7:10576, 2016.

[4] W Klement, R H Willens, and P Duwez. Non-crystalline Structure in Solidified Gold–Silicon Alloys. *Nature*, 187(4740):869–870, September 1960.

[5] H W Kui, A L Greer, and D Turnbull. Formation of bulk metallic glass by fluxing. *Applied Physics Letters*, 45(6):615–616, 1984.

[6] A Peker and W L Johnson. A highly processable metallic glass: $Zr_{41.2}Ti_{13.8}Cu_{12.5}Ni_{10.0}Be_{22.5}$. *Applied Physics Letters*, 63(17):2342, 1993.

[7] D M Herlach, R F Cochrane, I Egry, H J Fecht, and A L Greer. Containerless processing in the study of metallic melts and their solidification. *International Materials Reviews*, 38(6):273–347, January 1993.

[8] Y J Kim, R Busch, W L Johnson, A J Rulison, and W K Rhim. Metallic glass formation in

highly undercooled $Zr_{41.2}Ti_{13.8}Cu_{12.5}Ni_{10.0}Be_{22.5}$ during containerless electrostatic levitation processing. *Applied Physics Letters*, 65(17):2136–2138, 1994.

[9] X H Lin, W L Johnson, and W K Rhim. Effect of Oxygen Impurity on Crystallization of an Undercooled Bulk Glass Forming Zr-Ti-Cu-Ni-Al Alloy. *Materials Transactions, JIM*, 38(5):473–477, 1997.

[10] W L Johnson. Bulk Glass-Forming Metallic Alloys: Science and Technology. *MRS bulletin*, 24(10):42–56, October 1999.

[11] A Inoue. Stabilization of metallic supercooled liquid and bulk amorphous alloys. *Acta Materialia*, 48(1):279–306, January 2000.

[12] G Duan, A Wiest, Mary-Laura Lind, J Li, W K Rhim, and W L Johnson. Bulk Metallic Glass with Benchmark Thermoplastic Processability. *Advanced Materials*, 19(23):4272–4275, 2007.

[13] A Wiest, J S Harmon, Marios Demetriou, R D Conner, and W L Johnson. Injection molding metallic glass. *Scripta Materialia*, 60(3):160–163, 2009.

[14] J Schroers, Q Pham, A Peker, N Paton, and R V Curtis. Blow molding of bulk metallic glass. *Scripta Materialia*, 57(4):341–344, August 2007.

[15] Y Saotome, Y Noguchi, T Zhang, and A Inoue. Characteristic behavior of Pt-based metallic glass under rapid heating and its application to microforming. *Materials Science and Engineering: A*, 375-377:389–393, July 2004.

[16] G Kumar, Hong X Tang, and J Schroers. Nanomoulding with amorphous metals. *Nature*, 457(7231):868–872, February 2009.

[17] G Kumar, Amish Desai, and J Schroers. Bulk Metallic Glass: The Smaller the Better. *Advanced Materials*, 23(4):461–476, October 2010.

[18] J Schroers. Processing of Bulk Metallic Glass. *Advanced Materials*, 22(14):1566–1597, December 2009.

[19] C D Han. *Rheology and Processing of Polymeric Materials: Polymer Processing*, volume 2. Oxford University Press, 2007.

[20] H J Güntherodt. Metallic glasses. In *Festkörperprobleme 17*, pages 25–53. Springer, 1977.

[21] S Nagel. Temperature dependence of the resistivity in metallic glasses. *Physical Review B*, 16(4):1694–1698, August 1977.

[22] W H Wang, L L Li, M X Pan, and R J Wang. Characteristics of the glass transition and supercooled liquid state of the $Zr_{41}Ti_{14}Cu_{12.5}Ni_{10}Be_{22.5}$ bulk metallic glass. *Physical Review B*, 2001.

[23] J Schroers, A Masuhr, W L Johnson, and R Busch. Pronounced asymmetry in the crystallization behavior during constant heating and cooling of a bulk metallic glass-forming liquid. *Physical Review B*, 60(17):11855–11858, November 1999.

[24] Y J Kim, R Busch, W L Johnson, A J Rulison, and W K Rhim. Experimental determination of a time–temperature-transformation diagram of the undercooled $Zr_{41.2}Ti_{13.8}Cu_{12.5}Ni_{10.0}Be_{22.5}$ alloy using the containerless electrostatic levitation processing technique. *Applied Physics Letters*, 68(8):1057–1059, 1996.

[25] J Schroers, W L Johnson, and R Busch. Crystallization kinetics of the bulk-glass-forming $Pd_{43}Ni_{10}Cu_{27}P_{20}$ melt. *Applied Physics Letters*, 77(8):1158, 2000.

[26] D E Ballard, P G Frischmann, and A I Taub. Hot shear cutting of amorphous alloy ribbon. US Patent Office, October 1991.

[27] M R J Gibbs, D H Lee, and J E Evetts. D.C. magnetic properties of metallic glasses after flash annealing. *Magnetics, IEEE Transactions on*, 20(5):1373–1375, September 1984.

[28] A Zaluska and H Matyja. Crystallization and Relaxation of Amorphous $Fe_{50}Ni_{30}Si_{10}B_{10}$ Alloy During Pulse Heating. *Int. J. Rapid Solidification*, 2(3):205–218, 1986.

[29] T Kulik and H Matyja. Effect of flash- and furnace annealing on the magnetic and mechanical properties of metallic glasses. *Materials Science and Engineering: A*, 133:232–235, October 1991.

[30] M F de Oliveira, W J Botta F, C S Kiminami, A Inoue, and A R Yavari. Electromechanical engraving and writing on bulk metallic glasses. *Applied Physics Letters*, 81(9):1606–1608, 2002.

[31] A R Yavari, M F de Oliveira, C S Kiminami, A Inoue, and W J Botta F. Electromechanical shaping, assembly and engraving of bulk metallic glasses. *Materials Science and Engineering: A*, 375-377:227–234, July 2004.

[32] G Lohöfer and G Pottlacher. Rectangular Wires in Pulse-Heating Experiments. *International journal of thermophysics*, 26(4):1239–1254, October 2005.

[33] R Busch, Y J Kim, and W L Johnson. Thermodynamics and kinetics of the undercooled liquid and the glass transition of the $Zr_{41.2}Ti_{13.8}Cu_{12.5}Ni_{10.0}Be_{22.5}$ alloy. *Journal of Applied Physics*, 77(8):4039–4043, 1995.

[34] A Masuhr, T A Waniuk, R Busch, and W L Johnson. Time Scales for Viscous Flow, Atomic Transport, and Crystallization in the Liquid and Supercooled Liquid States of $Zr_{41.2}Ti_{13.8}Cu_{12.5}Ni_{10.0}Be_{22.5}$. *Physical Review Letters*, 82(11):2290–2293, 1999.

[35] J Lu, G Ravichandran, and W L Johnson. Deformation behavior of the $Zr_{41.2}Ti_{13.8}Cu_{12.5}Ni_{10.0}Be_{22.5}$ bulk metallic glass over a wide range of strain-rates and temperatures. *Acta Materialia*, 51(12):3429–3443, July 2003.

[36] G J Dienes and H F Klemm. Theory and Application of the Parallel Plate Plastometer. *Journal of Applied Physics*, 17(6):458–471, 1946.

[37] T A Waniuk, R Busch, A Masuhr, and W L Johnson. Equilibrium viscosity of the $Zr_{41.2}Ti_{13.8}Cu_{12.5}Ni_{10.0}Be_{22.5}$ bulk metallic glass-forming liquid and viscous flow during relaxation, phase separation, and primary crystallization. *Acta Materialia*, 46(15):5229–5236, September 1998.

[38] G J Fan, H J Fecht, and E J Lavernia. Viscous flow of the $Pd_{43}Ni_{10}Cu_{27}P_{20}$ bulk metallic glass-forming liquid. *Applied Physics Letters*, 84:487, 2004.

[39] H Choi-Yim, R Busch, and W L Johnson. The effect of silicon on the glass forming ability of the $Cu_{47}Ti_{34}Zr_{11}Ni_8$ bulk metallic glass forming alloy during processing of composites. *Journal of Applied Physics*, 83(12):7993, 1998.

[40] Y Saotome, K Itoh, T Zhang, and A Inoue. Superplastic nanoforming of Pd-based amorphous alloy. *Scripta Materialia*, 44(8-9):1541–1545, May 2001.

[41] Y Saotome, T Hatori, T Zhang, and A Inoue. The micro-formability of Zr-based amorphous alloys in the supercooled liquid state and their application to micro-dies. *Journal of Materials Processing Technology*, 113(1–3):64–69, 2001.

[42] Y Saotome, S Miwa, T Zhang, and A Inoue. Superplastic micro/nano-formability of $La_{60}Al_{20}Ni_{10}Co_5Cu_5$ amorphous alloy in supercooled liquid state. *Materials Science and Engineering: A*, 304-306:716–720, May 2001.

[43] Yasunori Saotome, Kenichi Imai, Shigeo Shioda, Susumu Shimizu, Tao Zhang, and A Inoue. The micro-nanoformability of Pt-based metallic glass and the nanoforming of three-dimensional structures. *Intermetallics*, 10(11-12):1241–1247, November 2002.

[44] P Sharma, N Kaushic, H Kimura, Y Saotome, and A Inoue. Nano-fabrication with metallic glass-an exotic material for nano-electromechanical systems. *Nanotechnology*, 18(3):035302, January 2007.

[45] H Kato, T Wada, M Hasegawa, J Saida, A Inoue, and H S Chen. Fragility and thermal stability of Pt- and Pd-based bulk glass forming liquids and their correlation with deformability. *Scripta Materialia*, 54(12):2023–2027, June 2006.

[46] J Schroers. On the formability of bulk metallic glass in its supercooled liquid state. *Acta Materialia*, 56(3):471–478, February 2008.

[47] E B Pitt, G Kumar, and J Schroers. Temperature Dependence of the Thermoplastic Formability in Bulk Metallic Glasses. *Journal of Applied Physics*, 110:043518, 2011.

[48] A Wiest, G Duan, Marios Demetriou, Landon a. Wiest, Andrew Peck, Georg Kaltenboeck, B Wiest, and W L Johnson. Zr–Ti-based Be-bearing glasses optimized for high thermal stability and thermoplastic formability. *Acta Materialia*, 56(11):2625–2630, 2008.

[49] S Pogatscher, P J Uggowitzer, and J F Löffler. In-situ probing of metallic glass formation and crystallization upon heating and cooling via fast differential scanning calorimetry. *Applied Physics Letters*, 104(25):251908, June 2014.

[50] O Darrigol. *Electrodynamics from Ampère to Einstein*. OUP Oxford, 2003.

[51] Xiao Liu, Marios Demetriou, Georg Kaltenboeck, Joseph P Schramm, Glenn R Garrett, and W L Johnson. Description of millisecond Ohmic heating and forming of metallic glasses. *Acta Materialia*, 61(8):3060–3067, 2013.

[52] M Ashby and A Greer. Metallic glasses as structural materials. *Scripta Materialia*, 54(3):321–326, February 2006.

[53] Marios Demetriou, Maximilien E Launey, Glenn Garrett, Joseph P Schramm, Douglas C Hofmann, W L Johnson, and Robert O Ritchie. A damage-tolerant glass. *Nature Materials*, 10(2):123–128, January 2011.

[54] J Schroers, Thomas M Hodges, G Kumar, Hari Raman, Anthony J Barnes, Quoc Pham, and Theodore A Waniuk. Thermoplastic blow molding of metals. *Materials Today*, 14(1-2):14–19, January 2011.

[55] G W Harvey and D F Brower. Metal forming device and method. US Patent Office, March 1961.

[56] F W Wilson. *High-velocity Forming of Metals*. A Publication in the ASTME manufacturing data series. Prentice-Hall, 1964.

[57] V Psyk, D Risch, B L Kinsey, A E Tekkaya, and M Kleiner. Electromagnetic forming—A review. *Journal of Materials Processing Technology*, 211(5):787–829, May 2011.

[58] John M Dealy and Kurt F Wissbrun. *Melt rheology and its role in plastics processing : theory and applications*. Van Nostrand Reinhold, New York, 1990.

[59] A Tschumi, T Laubscher, R Jeker, E Schüpfer, H U Künzi, and H J Güntherodt. Electrical resistivity and Hall coefficient of glassy and liquid alloys. *Journal of Non-Crystalline Solids*, 61-62:1091–1096, January 1984.

[60] A Masuhr. *Viscuous flow and crystallization of bulk metallic glass forming liquids*. PhD thesis, California Institute of Technology, October 1999.

[61] I Egry, G Lohöfer, I Seyhan, S Schneider, and B Feuerbacher. Viscosity and Surface Tension Measurements in Microgravity. *International journal of thermophysics*, 20(4):1005–1015, 1999.

[62] R Busch, E Bakke, and W L Johnson. Viscosity of the supercooled liquid and relaxation at the glass transition of the $Zr_{46.75}Ti_{8.25}Cu_{7.5}Ni_{10}Be_{27.5}$ bulk metallic glass forming alloy. *Acta Materialia*, 46(13):4725–4732, August 1998.

[63] S Mukherjee, J Schroers, W L Johnson, and W K Rhim. Influence of Kinetic and Thermodynamic Factors on the Glass-Forming Ability of Zirconium-Based Bulk Amorphous Alloys. *Physical Review Letters*, 94(24):245501, June 2005.

[64] Oleg N Senkov. Correlation between fragility and glass-forming ability of metallic alloys. *Physical Review B*, 76(10):104202, September 2007.

[65] W H Wang, C Dong, and C H Shek. Bulk metallic glasses. *Materials Science and Engineering: R: Reports*, 44(2-3):45–89, June 2004.

[66] Hong-Yu Ding, Yang Li, and Ke-Fu Yao. Preparation of a Pd-Cu-Si Bulk Metallic Glass with a Diameter up to 11 mm. *Chinese Physics Letters*, 27(12):126101, December 2010.

[67] J H Na, M Floyd, D Duggins, Marios Demetriou, and W L Johnson. Fluxing methods for nickel based chromium and phosphorus bearing alloys to improve glass forming ability. Technical Report 20150159248, 2015.

[68] Yi He, R B Schwarz, D Mandrus, and L Jacobson. Elastic moduli, density, and structural relaxation in bulk amorphous $Zr_{41.2}Ti_{13.8}Cu_{12.5}Ni_{10}Be_{22.5}$ alloy. *Journal of Non-Crystalline Solids*, 205-207:602–606, October 1996.

[69] C Aydiner. *Investigation of Thermal Tempering in Bulk Metallic Glasses*. PhD thesis, April 2004.

[70] W L Johnson, Marios Demetriou, J S Harmon, Mary-Laura Lind, and Konrad Samwer. Rheology and ultrasonic properties of metallic glass-forming liquids: A potential energy landscape perspective. *MRS bulletin*, 32(08):644–650, 2007.

[71] D N Perera. Compilation of the fragility parameters for several glass-forming metallic alloys. *Journal of Physics: Condensed Matter*, 11(19):3807, 1999.

[72] H S Chen. A method for evaluating viscosities of metallic glasses from the rates of thermal transformations. *Journal of Non-Crystalline Solids*, 27(2):257–263, 1978.

[73] A Hoff. Unpublished Viscosity data for $Ni_{68.17}Cr_{8.65}Nb_{2.98}P_{16.42}B_{3.28}Si_{0.5}$. 2014.

[74] A Cezairliyan. Design and operational characteristics of a high-speed (millisecond) system for the measurement of thermophysical properties at high temperatures. *J Res Nat Bur Stand(US) C*, 1971.

[75] Mary-Laura Lind, G Duan, and W L Johnson. Isoconfigurational Elastic Constants and Liquid Fragility of a Bulk Metallic Glass Forming Alloy. *Physical Review Letters*, 97(1):15501, 2006.

[76] P G Debenedetti and F H Stillinger. Supercooled liquids and the glass transition. *Nature*, 2001.

[77] R Busch, W Liu, and W L Johnson. Thermodynamics and kinetics of the $Mg_{65}Cu_{25}Y_{10}$ bulk metallic glass forming liquid. *Journal of Applied Physics*, 83(8):4134, 1998.

[78] R Busch and W L Johnson. The kinetic glass transition of the $Zr_{46.75}Ti_{8.25}Cu_{7.5}Ni_{10}Be_{27.5}$ bulk metallic glass former-supercooled liquids on a long time scale. *Applied Physics Letters*, 72(21):2695–2697, 1998.

[79] M J Stefan. Akademie der Wissenschaften in Wien. *Mathematik Naturwissen*, 69:713, 1874.

[80] J Schroers, Boonrat Lohwongwatana, W L Johnson, and Atakan Peker. Gold based bulk metallic glass. *Applied Physics Letters*, 87(6):061912, 2005.

[81] J Schroers and W L Johnson. Ductile Bulk Metallic Glass. *Physical Review Letters*, 2004.

[82] J Schroers and W L Johnson. Highly processable bulk metallic glass-forming alloys in the Pt–Co–Ni–Cu–P system. *Applied Physics Letters*, 84(18):3666, 2004.

[83] W L Johnson and Konrad Samwer. A Universal Criterion for Plastic Yielding of Metallic Glasses with a $(T/T_g)^{2/3}$ Temperature Dependence. *Physical Review Letters*, 95(19):195501, 2005.

[84] Marios Demetriou, Georg Kaltenboeck, Jin-Yoo Suh, Glenn Garrett, Michael Floyd, Chase Crewdson, Douglas C Hofmann, Henry Kozachkov, A Wiest, Joseph P Schramm, and W L Johnson. Glassy steel optimized for glass-forming ability and toughness. *Applied Physics Letters*, 95(4):41903–41907, 2009.